A Circularly-Polarized Optical Dipole Trap and Other Developments in Laser Trapping of Atoms

by

Kristan Lee Corwin

B.A., State University of New York at Buffalo, 1993

M.S., University of Colorado, 1997

A thesis submitted to the

Faculty of the Graduate School of the

University of Colorado in partial fulfillment

of the requirements for the degree of

Doctor of Philosophy

Department of Physics

1999

This thesis entitled:
A Circularly-Polarized Optical Dipole Trap and Other Developments in Laser Trapping of Atoms
written by Kristan Lee Corwin
has been approved for the Department of Physics

Dr. Carl E. Wieman

Dr. Deborah S. Jin

Date

The final copy of this thesis has been examined by the signatories, and we find that both the content and the form meet acceptable presentation standards of scholarly work in the above mentioned discipline.

Corwin, Kristan Lee (Ph.D., Physics)

A Circularly-Polarized Optical Dipole Trap and Other Developments in Laser Trapping of Atoms

Thesis directed by Prof. Dr. Carl E. Wieman

Several innovations in laser trapping and cooling of alkali atoms are described. These topics share a common motivation to develop techniques for efficiently manipulating cold atoms. Such advances facilitate sensitive precision measurements such as parity non-conservation and β-decay asymmetry in large trapped samples, even when only small quantities of the desired species are available.

First, a cold, bright beam of Rb atoms is extracted from a magneto-optical trap (MOT) using a very simple technique. This beam has a flux of 5×10^9 atoms/s and a velocity of 14 m/s, and up to 70% of the atoms in the MOT were transferred to the atomic beam. Next, a highly efficient MOT for radioactive atoms is described, in which more than 50% of ^{221}Fr atoms contained in a vapor cell are loaded into a MOT. Measurements were also made of the ^{221}Fr 7 ^{2}P$_{1/2}$ and 7 ^{2}P$_{3/2}$ energies and hyperfine constants. To perform these experiments, two schemes for stabilizing the frequency of the light from a diode laser were developed and are described in detail.

Finally, a new type of trap is described and a powerful cooling technique is demonstrated. The circularly polarized optical dipole trap provides large samples of highly spin-polarized atoms, suitable for many applications. Physical processes that govern the transfer of large numbers of atoms into the trap are described, and spin-polarization is measured to be 98(1)%. In addition, the trap breaks the degeneracy of the atomic spin states much like a magnetic trap does. This allows for RF and microwave cooling via both forced evaporation and a Sisyphus mechanism. Preliminary application of these techniques to the atoms in the circularly polarized dipole trap has

successfully decreased the temperature by a factor of 4 while simultaneously increasing phase space density.

Dedication

To my loving parents,

Allen George Corwin

and

Julie Ann Grastorf Corwin.

Acknowledgements

Many, many people have helped make my graduate school experience a rich and rewarding one. Although it is impossible for me to thank them all, here I attempt to mention those who have had the greatest influence on my research at CU.

I have been very fortunate to learn atom trapping from a master, Carl Wieman. He brings an honest and direct approach to both people and science, which I appreciate. And I thank him for the mentoring me on everything from preparation for oral exams to personal and professional advice on being a good scientist. When he adds this document to his collection, I hope he'll say (as on the day he found the source of some particularly annoying noise) "Superadvisor strikes again!!!"

I have also had the pleasure to work with many talented postdocs. The first was Michelle Stephens, who patiently showed me around JILA and taught me important skills such as tuning a Ti:Sapph laser, making dry film coatings, and drilling holes. Even after she left JILA, her continued support has been very much appreciated. After a couple months on my own, I was very happy to welcome Zheng-Tian Lu to the experiment. Lu always encouraged my complete involvement in the experiment, and inspired me by his example to work efficiently and responsibly, always with the final goal in mind. His love of science is contagious, and I am certain that he is now an excellent advisor for his own students and postdocs at Argonne National Labs.

Simon Kuppens joined the experiment about 1 1/2 years ago. At that time, I was certain that I didn't need a postdoc, much like the eldest VanTrapp daughter in

the Sound of Music who asserted, “I don’t need a governess!” But Simon showed me otherwise. He brought to the experiment a mathematical approach that was crucial to the unraveling of the FORT loading puzzle. In addition, he became a close friend. Once a visitor asked if we always run the experiment with so much laughter, and the answer was... yes! I already miss him since his return to Holland.

The experiment is now in good hands. Kurt Miller has been doing great work on the experiment for over two years. The majority of the evidence for cooling is largely due to his efforts – we wouldn’t even know the FORT temperature without him. As he takes over the experiment, he’ll have excellent help from Stephan Dürr, who only joined the group 6 weeks ago but is already making big contributions. I thank Stephan for his helpful comments on the cooling mechanisms and especially Landau-Zener transitions, and I’m sorry I won’t have a chance to work more with him.

Many other people have contributed directly to the work described in this thesis. The LVIS experiment sprung from an idea of Mike Anderson, followed by an astute observation of Mike Renn. In addition, the DAVLL lock was developed with help from Carter Hand and Ryan Epstein. And Tasha Fairfield contributed to the development of the cavity lock.

The francium experiment would have been impossible without the source and hard work provided by the Berkeley team: Tim Dinneen, Harvey Gould, and Jason Maddi. And prospects for finishing the experiment looked dim until Kurt Vogel rode in on a shining Ar^+ laser (from Jan Hall) and saved the day. Thanks also to JILA for providing us a new Ar^+ laser tube, days before the final francium source arrived. That experiment taught me how close colleagues can become when working on a source with a 1 month decay time; I miss the sense of excitement and camaraderie, but not the sleep deprivation. Several members of the JILA shops made major contributions to the Fr experiment: Dave Alchenberger constructed the vacuum chamber and the high-precision oven manipulator, Hans Rohner built the beautiful glass cell and helped

us coat it, and Terry Brown build the high-speed electronics that made the precise λ-meter measurements possible. John Smedley, a JILA visiting fellow, also worked on experiment construction.

Before the FORT project, I had an opportunity to bridge the gap between the old and new teams on the "Fiber project," under the supervision of Dana Anderson, Eric Cornell, and Carl Wieman. Elizabeth Donley showed me the ropes, and I passed things on to Eric Abraham, Brian DeMarco, and Dirk Müller. I enjoyed working with Brian and Dirk as new grad students, back when THEY had asked ME questions; it seems the roles are now largely reversed. I also appreciated Eric A.'s guidance at that time, even after I left the project in capable hands to return to the circularly polarized FORT.

The circular FORT project was originally conceived by Dong Hyung Cho, who has continued to participate in the project during his visits to Boulder. He also graciously hosted me at his home institution, Korea University, where the collaboration continued. Timothy Chupp also contributed to the studies of FORT loading while he was a JILA visiting fellow in 1997-98. I appreciate Tim teaching me to take the time to stop and think on the "rare" occasions when we did not immediately understand our experimental results. I also enjoyed working and playing soccer with him. Jake Roberts did a brief stint on the project between the Cs parity violation measurement and the Bose-Einstein Condensation measurement, and his contributions then and throughout the experiment have been very valuable. Neil Claussen has also contributed to both the earliest and most recent stages of the FORT experiment, from modeling the loading of the FORT after its initial observation to providing us with a high-power laser system that he personally constructed (the MOPA).

I also want to thanks all the members of the Wieman group who contributed greatly to the stimulating and supportive atmosphere. The old gang includes Steve Bennett, Eric Burt, Rich Ghrist, Nate Newbury, Chris Myatt, and Chris Wood. Present members include Nick Cizek, Simon Cornish, and John Essick. Undergraduates Dan

Lowell and Travis Andrews also provided a lot of assistance in the labs.

The Wieman-Cornell-Jin "family" provides a wonderful environment in which to do science. Eric Cornell has served as my additional advisor many times, and I appreciate his ideas and his support. Debbie Jin often has helpful insights during group meeting, and I thank her also for a careful reading of this manuscript with many useful suggestions. Other current "family" members who continue to make this a great group include: Brian Anderson, Ian Coddington, Paul Haljan, Heather Lewendowski, Scott Papp, Marco Prevedalli, Malcom Rickard, Peter Schwindt, and Dwight Whitaker. Previous members who have moved on to great things include Anne Curtis, Harold Gauck, Tim Gfroerer, David Hall, Sergio Muniz, and especially Mike Matthews. Jason Ensher deserves special mention, since he and I have been in school together 10 years, both at UB and CU, and he has always both challenged and encouraged me.

JILA has many staff members, besides those already mentioned, who have made my graduate career a lot easier or better. Fran Haas, Rhonda Hickey, Pam Leland, Karen Melcher and now Linda Morris have helped keep the group and JILA running smoothly, and they have provided me personally with a lot of support and encouragement. In the Scientific Reports Office, Marilee Degode has improved many of the papers appearing here, as has Laurie Kovalenko through the scientific writing course. In the Electronics Shop, Paul Beckingham taught me his Survival class and helped me with many circuits, always keeping me on my toes until we were "home and dry." James Fung-A-Fat and Mike Whitmore also helped us out a lot. I also thank all the instrument shop members, including Blaine Horner, John Andru, and Hans Green. Among the computing staff, thanks to Alan Dunwell, Joel Frahm, Chela Kunaz, and Peter Ruprecht. Also to the supply office staff: Maryly Dole, Ed Holliness, Brian Lynch, and David Tegart. The rest of the JILA staff has always been very helpful, and I thank you all.

My experience during the early years of graduate school was shaped predominantly by members of my class. I had an opportunity to work a problem with each and

every one of them. I cannot list all my classmates here, but they include Brian King, Shawn Kraut, Sarah Makoski, Jim Mooney, Keith Nordstrum, Arnold Leitner, Darren Link, Harold Parks, Brad Paul, Orion Poplawski, Shuka Schwarz, Eric Vaandering, and Oleg Vdovin. Thanks to the faculty at CU, including my committee members Katy Garmany, Steve Pollock, and Murray Holland. Also Jinx Cooper, Alan Gallagher, and Trisha Rankin, among others.

I have been blessed with many dear friends over the last six years who reminded me of life outside of cold atoms. Thanks to Sara Cho, Hilary Eaton, Melissa Fu, Dana Jandzinski, Kim King, Heather Robinson, Sarah Parks, Sarah Roberts, and many others. Special thanks to Josh Long, whose love and understanding have been very important to me the last couple years. My extended family has also been very supportive. Finally, I thank my mom, dad, and sister Kelly for encouraging me to come to graduate school so far from home, for the long phone calls and many visits, and their enthusiasm for my success. I couldn’t have done it without them.

Contents

Chapter

1 Introduction 1

1.1 Atomic Beams and the Development of Neutral Atom Traps 1

1.2 Trapping Radioactive Elements 4

1.3 Optical Dipole Traps 5

1.4 Cooling in Dipole Potentials 6

2 A Low-Velocity Intense Source of Atoms from a Magneto-Optical Trap 8

2.1 Introduction 8

2.2 Description 9

2.3 Experimental Setup 9

2.4 Results 11

2.4.1 Optimum Detuning 11

2.4.2 Longitudinal velocity 11

2.4.3 Collimation 12

2.4.4 Flux 15

2.5 Conclusion 16

3 Efficient Collection of ^{221}Fr into a Vapor Cell Magneto-optical Trap 17

3.1 Introduction 17

3.2 Theory 18

3.3 Experimental Setup 18
3.3.1 Fr Source 18
3.3.2 The Magneto-optical Trap 19
3.3.3 Sensitive Detection 19
3.4 Results 21
3.4.1 Trapping Efficiency 21
3.4.2 Spectroscopy 22
3.5 Conclusions 23

4 Spin-Polarized Atoms in a Circularly Polarized Optical Dipole Trap 25
4.1 Introduction 25
4.2 Theory 25
4.3 Experimental Setup 27
4.3.1 The Lasers 27
4.3.2 The Pockels Cell and Polarization Issues 30
4.3.3 Diagnostics and Loading 31
4.4 The Elliptically and Circularly Polarized FORTs 33
4.4.1 Loading Atoms into the Circular FORT 33
4.4.2 Elliptically Polarized FORT Decay Rates 34
4.4.3 Model of Lifetime vs. Ellipticity 35
4.4.4 FORT $\lambda > \lambda_{D_1}$ 36
4.5 Spin-Polarization Demonstration 38
4.6 Conclusion 38

5 The Physics of Loading an Optical Dipole Trap 40
5.1 Introduction 40
5.2 The FORT potential 42
5.3 Experiment 43

5.3.1 Loading and diagnostics 44
5.4 Dynamics of the loading process 45
5.4.1 Hyperfine repump intensity and detuning 48
5.4.2 Primary MOT light intensity 50
5.4.3 The role of MOT detuning 52
5.4.4 Alignment with respect to the MOT 53
5.4.5 Dependence on FORT depth 54
5.4.6 The effect of elliptically polarized FORT light 56
5.5 Temperature 57
5.6 Trap Lifetime 58
5.7 Analysis 59
5.7.1 Analysis of density dependent losses 59
5.7.2 A model for the FORT loading rate 62
5.8 Discussion 66
5.9 Enhanced and quasi continuous loading 67
5.10 Conclusions 69

6 Cooling in the Circularly Polarized Optical Dipole Trap 70
6.1 Motivation 70
6.2 Theory 71
6.2.1 Sisyphus Cooling Mechanism 71
6.2.2 Repumping with Spontaneous Scattering 77
6.2.3 Cooling Rates 80
6.2.4 Evaporative Cooling 81
6.2.5 Heating Mechanisms 82
6.2.6 Ultimate Temperatures 82
6.2.7 Cooling with a Pulsed Drive 83

6.3 Experimental Implementation 84
6.3.1 RF considerations 84
6.3.2 MOPA 84
6.3.3 Procedure 86
6.4 Preliminary results 87
6.4.1 Two-Photon Stimulated Raman Transitions 87
6.4.2 Cooling with Stationary Frequency 87
6.4.3 Cooling with Swept Microwave Frequency 91
6.4.4 Heating Rates 91
6.5 Conclusion 91

Bibliography 94

Appendix

A Dichroic Atomic Vapor Laser Lock 102
A.1 Introduction 102
A.2 Diode Laser Frequency Stabilization 102
A.3 The Dichroic-Atomic-Vapor Laser Lock Signal 104
A.4 Apparatus 105
A.5 Characterization of Frequency Stability 107
A.6 Conclusion 109

B Stabilization of a Diode Laser at an Arbitrary Frequency 110
B.1 Introduction 110
B.2 Description 110
B.3 Implementation 114

B.3.1 Components 114
B.3.2 Procedure 115
B.3.3 Polarization 115
B.4 Results 116
B.5 Conclusion 116

Tables

Table

3.1 Various rates, fluxes, and efficiencies for the transfer of ^{221}Fr from the source to the trap. 23

3.2 The hyperfine constants and wavenumbers of ^{221}Fr. 23

6.1 Repumping probability from the $|2, +1>$ state. 78

6.2 Repumping probability from the $|2, +1>$ state. 80

Figures

Figure

2.1 Schematic of the LVIS system. 10

2.2 A typical longitudinal velocity distribution. 12

2.3 The average longitudinal velocity and flux as a function of the forcing laser intensity and detuning. 13

2.4 The average longitudinal velocity and spread as a function of the forcing beam polarization. 14

2.5 The measured divergence angle as a function of the collimation length z. 15

3.1 A diagram of the ^{221}Fr trap setup. 20

3.2 The atomic level diagram of ^{221}Fr. 21

3.3 The number of atoms loaded into a ^{221}Fr trap vs. time, showing a trapping efficiency of 56(10)%. 22

4.1 Schematic level diagram for ^{85}Rb. 26

4.2 AC Stark shift $U(\rho)$ in the focus of a circularly polarized Gaussian laser beam for both hyperfine levels. 27

4.3 Maximum FORT Potential depth as a function of FORT wavelength. . . 28

4.4 Schematic of the experimental apparatus. 29

4.5 FORT laser beam polarization as a function of the voltage applied to the Pockels cell. 32

4.6 Number of atoms stored in a linearly polarized FORT as a function of trapping time. 33
4.7 Dependence of the FORT exponential loss rate Γ on the ellipticity ϵ of the FORT laser polarization. 34
4.8 Exponential decay rate Γ vs. FORT peak intensity for three different FORT polarizations. 35
4.9 FORT decay curve with FORT $\lambda = 798.4$ nm. 37
4.10 Demonstration of spin-polarized atoms in the circular FORT. 39

5.1 Number of atoms N in the FORT as a function of time spent loading. . 41
5.2 Experimental setup 43
5.3 Number of atoms remaining in the FORT as a function of time for $\lambda = 782.5\,\mathrm{nm}$. 45
5.4 Number of atoms loaded in the FORT as a function of FORT loading stage duration. 46
5.5 Number of atoms in the FORT vs time, both with and without MOT light on. 48
5.6 FORT loading rate R_0 and loss coefficient β'_{L} as a function of hyperfine repump light intensity. 49
5.7 Number of atoms in FORT as a function of MOT hyperfine repump detuning for different repump intensities. 50
5.8 FORT loading rate R_0 (a) and loss coefficient β'_{L} (b) as a function of primary MOT light intensity, for a repump intensity of $5\,\mu\mathrm{W/cm}^2$. . . . 51
5.9 FORT loading rate R_0 and loss coefficient β'_{L} as a function of the primary MOT light detuning, Δ_{M}. 52
5.10 Optimum MOT detuning versus FORT depth. 53

5.11 Number of atoms loaded into the FORT as a function of trap depth for two different beam waists w_0. 54
5.12 FORT Loading rate R_0 and loss rate $\beta'_{\rm L}$ as a function of trap depth U_0. . 55
5.13 Number of atoms in the FORT as a function of loading time for three different ellipticities of the FORT light. 56
5.14 Illustration of ballistic expansion and temperature measurement. 57
5.15 Temperature of the atoms in the FORT as a function of trap depth, for $w_0 = 26\,\mu\mathrm{m}$. 58
5.16 Approximate intramolecular potential for Rb, with $C_3 = 71\,\text{Å}^3\,\mathrm{eV}$. . . . 62
5.17 Radiative escape loss rate coefficient β calculated as a function of the trap depth. 63
5.18 Comparison of loading model with measured results. 64
5.19 Equipotential contours of the FORT. 65
5.20 Demonstration of enhanced loading using a shadowed repump beam. . . 68

6.1 Two mechanisms for Sisyphus cooling. 73
6.2 Effective Rabi frequency/(2π) for the two-photon stimulated Raman transition. 75
6.3 Landau-Zener transition probability in the circular FORT. 76
6.4 Fraction of energy removed in one cooling cycle as a function of initial energy. 79
6.5 Attenuation of rf radiation by the vacuum chamber. 85
6.6 Optimum modulation of the MOPA. 86
6.7 Layout of the all-optical two-photon stimulated Raman cooling scheme. 88
6.8 Observation of loss-inducing two-photon Raman transitions. 89
6.9 Cooling with a fixed microwave frequency. 90
6.10 Cooling with a swept microwave frequency. 92

6.11 Heating rate of atoms stored in the circular FORT. 93

A.1 Schematic of a DAVLL system. 103

A.2 Comparison of the signal from a saturated absorption spectrometer and a DAVLL system. 104

A.3 Origin of the DAVLL signal shape. 106

A.4 Measured beat frequency between two DAVLL systems over a 38 h period. 108

B.1 Schematic of the cavity locking system. 112

B.2 Fractional transmission (calculated) of a cavity with a finesse of 40 for two different wavelengths. 113

B.3 A simple computer algorithm. 114

Chapter 1

Introduction

The laser trapping and cooling of atoms has been a rapidly growing field since its inception in the 1970s. A variety of optical trapping and cooling forces have been discovered and employed successfully on atomic gases. These technologies have made possible a host of advances, including more accurate atomic clocks, atom lithography, atomic interferometry, and the creation of quantum degenerate gases [1]. In addition, several precision measurements are being performed using these techniques, including the asymmetry of nuclear β-decay, the electric dipole moment of the electron, and parity non-conservation in electronic transitions of atoms.

The precision measurements listed above require large samples of rare atoms. The most sensitive measurement of parity non-conservation [2] required many grams of Cs per week, and 350 hrs of data collection. Such large quantities of radioactive elements are generally unavailable; production rates of 10^5 /s are typical [3]. Therefore, there is a need for efficient collection and manipulation of these atoms to make improved precision measurements possible.

The work presented here represents a series of advances that have implications for most of the topics mentioned above. The original motivation for these advances was to develop tools for making a precision measurement on radioactive alkali atoms. These advances therefore include an efficient technique for transferring atoms out of an initial magneto-optical trap (MOT) into a slow, bright atomic beam. They also include the efficient collection of radioactive Fr into a MOT. The majority of this work is dedicated to the description of a new type of laser trap that may prove useful for precision measurements. The properties of the trap are discussed, as well as the mechanisms developed to transfer atoms into it as efficiently as possible. Finally, cooling mechanisms in the trap are explored. While cooling may not be necessary for precision measurements, it is very important for achieving quantum degeneracy, and may make this trap useful for attaining Bose-Einstein Condensation using purely optical techniques.

1.1 Atomic Beams and the Development of Neutral Atom Traps

Since the beginning of modern atomic physics, effusive atomic beams have played a central role. The study of beams has led to the development of most of the tools in the lab used to produce this work, the first part of which (Chapter 2)is itself a useful advance in the technique of beam control.

In the 1920's, Stern and Gerlach first discovered the quantized nature of spin angular momentum by observing the deflection of a beam of Ag atoms [4, 5]. In the 1930s and 40s, I. I. Rabi developed the concept of nuclear magnetic resonance in beams of Na [6], laying the groundwork for the MASER and then the LASER, the principal tool of atomic physics as it is practiced today. In general, these beams were made by heating samples of Ag or Na in a container with a small aperture. The resulting increase in vapor pressure in the container caused the atoms to exit the aperture, forming a beam. Beams made this way were poorly collimated and moved very fast (on the order of 1000 m/s). However, they became the basis of seven generations of atomic time standards in Boulder, Colorado and around the world.

Forty years after Rabi's work, and with an interest in improving the time standard, Phillips and Metcalf successfully decelerated a beam of Na atoms using laser light and a magnetic field [7]. This technique, called the "Zeeman slower", is still used today. The key to the success of the technique is the application of a spatially varying magnetic field that tunes the atoms into resonance with the counter-propagating laser as they decelerate, in order to counteract the changing Doppler shift. Atoms leaving the oven with a high velocity and therefore a large positive Doppler shift absorb photons from a laser directed toward the beam and tuned near to the atomic resonance frequency. This laser exerted a "spontaneous scattering force" on the atoms. Each time the atom absorbs a photon from the laser beam, its momentum decreases by the amount of momentum carried by the photon, $\hbar k$. The photon is then reemitted in a random direction. Therefore, on average the atoms slow down as they move toward the laser beam until they are out of resonance with the laser. But by reducing the applied magnetic field, the atoms are shifted back into resonance with the lasers, absorb more photons, and are further slowed. Unfortunately, there is no cooling in the transverse direction, and in fact the spontaneous emission of photons in random directions gives rise to heating in the transverse dimensions. Thus as the longitudinal velocities approach the transverse velocities (≤ 15 m/s), the atoms diffuse randomly and densities are therefore limited. Another implementation of the slowed beam, such as the chirp-cooled beam [8], does not require magnetic fields. Instead, the frequency of the laser light is varied in time, in order to stay resonant with the atoms.

An important extension of the scattering force to three dimensions occurred when a so-called optical molasses was loaded with the chirp-cooled beam [9]. Optical molasses relies on the same spontaneous scattering force described above, but in three dimensions. Laser beams from six directions intersect at the end of the slowed beam, and their frequency is detuned several linewidths from resonance. When an atom in the molasses region moves toward one of the laser beams, it will be Doppler shifted into resonance with that beam and absorb photons from it until the atom slows down in that direction. The atom must then reradiate the photon in a random direction, which results in heating. The Doppler cooling temperature limit, or "Doppler Limit" T_{D} is then set by a balance between the molasses cooling and the heating that results from the spontaneously emitted photons. In general, this limit depends only on the natural

linewidth γ of the atomic transition [10]:

$$T_{\mathrm{D}} = \frac{\hbar\gamma}{2k_{\mathrm{B}}}$$

where $\hbar$ is Planck's constant over 2 π and k_{B} is Boltzman's constant. A temperature consistent with the Doppler limit was initially observed in a cloud of Na atoms at 240 μK [9].

Several years later, Lett *et al.* [11] cooled Na to below the Doppler limit in an optical molasses, to 43 μK. No reasonable explanation of this surprising sub-Doppler cooling existed until two groups [12, 13] proposed a polarization gradient cooling mechanism. They explained that the counter-propagating, orthogonally-polarized molasses beams form a standing wave. In this case, the polarization of the standing wave changes every λ/4. When the polarization reverses, the direction of optical pumping and also the polarization- dependent light shifts of the atom change. An atom tends to be optically pumped into internal states with lower potentials as it travels through the standing wave. The time lag between traveling into the new polarization and optical pumping causes the atoms to be continuously pumped from deep potentials into shallower ones. Thus the atoms tend to move uphill more than down, and are therefore cooled in this so-called "Sisyphus" mechanism.

The first neutral atom trap to use the spontaneous scattering force was made in 1987 by Raab *et al.* [14]. To turn an optical molasses into a magneto-optical trap (MOT), the lasers must be circularly polarized and they must intersect in the center of a quadrupole magnetic field. This field is zero in the center of the trap, and increases in magnitude as atoms move away from this field zero. Now the scattering force can provide spatial confinement as well as cooling. As an example, consider what happens to an atom in one dimension as it moves to the left in the potential. The magnetic field in this dimension is pointed away from the center, and the laser polarization is then arranges so that σ_- comes from the left and σ_+ from the right. As the atom moves to the left, the magnetic field breaks the energy degeneracy of the atomic spin orientations. Thus $\Delta m = -1$ transitions shift to lower frequencies, into resonance with the red-detuned laser beam coming from the left, and further out of resonance with the σ_+ beam from the right. Therefore the atom is always pushed back to the trap center and spatially confined.

Later, it was shown that the MOT could capture atoms directly from a room-temperature atomic vapor instead of a precooled atomic beam[15]. A vapor-cell MOT is much simpler to construct that a beam-fed MOT. However, it has the limitation of a background pressure of atoms being trapped. Thermal background atoms limit the lifetime of the MOT and heat the sample [16, 17]. Therefore, when long lifetimes are required, a two-chambered MOT is constructed. In this system, atoms are pushed out of the MOT in the high-pressure chamber with a resonant laser beam, through a magnetic hextapole atom waveguide formed with six permanent magnets, and into a second MOT in a chamber of lower pressure[18]. In this way, the vapor cell MOT can be used in applications requiring very long lifetimes, such as Bose-Einstein condensation[19].

Meanwhile, the quest to create a brighter, better atomic beam continued. The

spontaneous scattering force techniques described above for three-dimensional confinement was employed to cool the two transverse dimensions. In this way, the atom funnel was developed [20]. Similar two-dimensional compression was demonstrated by other groups [21, 22, 23]. These systems often require a complicated apparatus or laser configuration.

In Chapter 2, a novel method of creating a cold atomic beam is presented. While making use of modern trapping techniques, the design is much simpler than that of other cold beam demonstrations. Dubbed a low velocity intense source, or LVIS, it is made by creating a small leak in a MOT through which atoms exit in a collimated beam. Its simple design and implementation make it an excellent source for cold atoms. In addition, it is a highly efficient source for an atomic beam, as the integrated flux in the beam can be up to 70% of the loading rate of the MOT.

After the publication of the first LVIS results in 1996 [24], it has been used as a source of atoms for several applications. An LVIS beam has been used to load a second MOT [25], with a transfer efficiency of $67 \pm 15\%$, limited only by beam divergence. Williamson *et al.* [26] transferred ^{39}K and ^{40}K a distance of 35 cm from a modified pyramidal trap [27] using an LVIS-like technique. Unfortunately, the transfer efficiency was limited to 6%, perhaps due to poor collimation in the pyramid configuration. In addition, atoms from the LVIS beam have been successfully guided in an optical fiber [28] and a magnetic waveguide [29].

1.2 Trapping Radioactive Elements

Chapter 3 describes the efficient transfer of radioactive ^{221}Fr atoms from a room-temperature vapor into a MOT. This represents a major advancement over the conventional vapor cell MOT technique described above. Typical vapor cell MOTs are inefficient for two major reasons. First, the probability of an individual atom in the vapor to be captured by the MOT is not optimized, in part because the volume of the vacuum chamber far exceeds the capture volume of the MOT (ie. the region of overlap of all 6 laser beams). Second, the alkali atoms tend to stick to and react with metal and glass surfaces, so that the majority of the atoms of interest in the chamber are adsorbed in a monolayer on the surface, and therefore cannot be trapped.

To circumvent the first problem, a redesigned vacuum chamber minimizes the chamber volume while maximizing the capture volume [30]. To solve the second, non-stick dryfilm coatings similar to those developed for optical pumping vapor cells are used to coat the trapping cell [31]. In addition, large, high-powered laser beams and optimized detunings improve the capture probability [32]. By using very large laser beams and high powers, along with a coated trapping cell almost completely illuminated with the trapping lasers, we demonstrated a ^{221}Fr trapping efficiency of over 50%. This represents a large improvement over previous radioactive trapping results. In addition, this experiment offers the advantage of a laboratory source to produce Fr [33] instead of a particle accelerator.

Other groups have continued to pursue trapping of radioactive atoms since the demonstration of the ^{221}Fr trap [34]. The Stony Brook collaboration has maintained an

active pursuit of spectroscopy in neutron-deficient isotopes of Fr (see for example Ref. [35]). Large samples of radioactive ^{82}Rb have been trapped using a technique similar to that described here, but with a trapping efficiency of only 0.3%. The poor trapping efficiency was largely due to poor coating performance, most likely caused by inductive heating of the foil to 800^{o}C inside the cell, which damaged the dryfilm coatings. Using a Zeeman slower, 40,000 atoms of ^{21}Na [36] have been trapped in preparation for a β-decay asymmetry measurement.

1.3 Optical Dipole Traps

The optical dipole trap, another confinement technique developed in the 1980s, is based on an effect quite different from the spontaneous scattering force described above. While the scattering force acts in the direction of laser propagation, the dipole force acts in the direction of the gradient of the laser intensity. The optical dipole force was first observed in 1978 (See Ref. [37]), when researchers co-propagated a tightly-focused laser beam with an atomic beam. They observed that when the laser was tuned close to the atomic resonance frequency, the laser beam caused deflection and focusing of the atoms. Thus the light exerted a force on the atoms perpendicular to the direction of laser propagation!

The energy shift of atoms in a light field is often referred to as the AC Stark shift or the light shift, and the gradient of this energy shift gives the dipole force. The dipole force can be understood simply in terms of the atom electric polarizability. In free space, an atom in its ground state has no electric dipole moment. However, a static electric field induces a dipole moment in the atom, reducing its potential energy. Therefore a gradient in electric field draws the atom toward the region of space with higher field. The AC Stark shift arises in a similar fashion; the laser light is simply an electromagnetic field that reverses direction every few femtoseconds. If the laser frequency is below the atomic resonance, the dipole induced in the atom can “keep up”, or stay in phase with the light, and atoms are drawn to regions of highest intensity. If instead the light frequency is tuned above the atomic resonance, the dipole moment always opposes the electric field, and atoms are expelled from regions of highest intensity.

The dipole force was used to demonstrate the first optical trap for atoms in 1986 [38]. In this experiment, about 500 Na atoms were confined at the waist of a focused Gaussian laser beam. The laser beam contained about 220 mW, detuned about 650 GHz below the atomic resonance frequency and focused to a 10 μm spot size. The trap was loaded from an optical molasses by rapidly alternating between the optical molasses and the optical dipole trap. The trap laser detuning Δ was much larger than the width of the transition, but not large enough to completely suppress the spontaneous scattering force.

Soon after this experiment, the MOT was developed and could trap many more atoms at much higher densities. Therefore dipole traps were generally abandoned until in 1993 when the far off resonance trap (FORT) was demonstrated [39]. This trap employed more power and larger detunings, and captured a few thousand atoms. The increased detunings allowed the much longer trap lifetimes than those of the original

dipole traps, in order to have strong dipole forces and simultaneously have low spontaneous scattering rates that cause negative effects. The dipole trapping force that actually does the trapping scales as Δ^{-1}, while the spontaneous photon scattering rate scales as Δ^{-2}. Spontaneous scattering, although many orders of magnitude lower in the FORT than the MOT, can still cause heating, decoherence, and scrambling of the internal states. Thus even if atoms are spin-polarized before they are stored in the dipole trap, the spontaneous scattering rate will tend to depolarize them [40].

Many other types of dipole traps have been developed that rely on large detunings and high powers. Blue-detuned light traps are also used. They have the advantage that atoms spend the majority of their time in the dark where they cannot absorb photons. However, these typically shallow traps tend to be difficult construct and have large volumes and unusual heating effects.

Chapter 4 and Ref. [41] presents a novel kind of dipole trap called a circular FORT that takes advantage of an interesting aspect of the dipole force. When the dipole trapping beam is circularly polarized, the value of the light shift depends on the internal spin state of the atoms [42, 43]. Therefore, although we use small detunings of only a few nm, the spontaneous scattering of the circularly polarized light always returns the atoms to the same internal spin state. Although heating and decoherence still result, the atoms are not depolarized. Therefore this trap makes an excellent source of spin-polarized atoms for precision measurements.

Demonstration of the circularly polarized FORT, or "circular FORT," first requires the efficient loading of a large atom sample. Although many groups have described their specific techniques for loading atoms into a dipole trap, no one has offered a detailed understanding of the many physical processes that govern the loading of the FORT. Therefore, Chapter 5 and Ref. [44] present a detailed study of the loading of the FORT as a function of the parameters of the MOT. A simple model is developed for the loading process and the loss processes unique to the FORT in the presence of the MOT light. Use of this model led to techniques which increased the number of atoms loaded into the FORT to 7×10^6. Samples of this size are sufficient to consider precision measurements and novel dipole cooling schemes discussed below.

1.4 Cooling in Dipole Potentials

The spin states are non-degenerate in the circular FORT, much as they are in magnetic traps. Magnetic traps confine atoms using potentials arising from the interaction of the atomic magnetic moment with the magnetic field. Because they do not rely on light fields, spontaneous scattering does not occur, and trap heating can be limited to collisions with high temperature atoms in the vacuum chamber. In addition, two very powerful cooling schemes have been demonstrated in the trap. The first is forced evaporative cooling, in which the highest energy atoms of a thermal distribution are removed, leaving the cloud to return to thermal equilibrium at a lower temperature. This mechanism reduces the temperature rapidly, with minimal loss of atoms.

Because a magnetic trap relies on the Zeeman effect to produce confinement, different spin states of the atom have different dipole moments and therefore differ-

ing strengths of confinement. Using two of these spin states, a Sisyphus cooling was effectively demonstrated [45]. Atoms confined in a deeper potential were allowed to oscillate to their turning point, at which point they were transferred into the shallower state. After waiting a quarter oscillation period for the atoms to reach the bottom of the potential, they were transferred back to the deeper state. This powerful refrigeration technique cooled the atoms to nearly the recoil limit (ie. the temperature of an atom with the kinetic energy equivalent to 1 photon recoil). This mechanism is similar to the Sisyphus cooling described earlier; the biggest difference is that in this case, the potentials used for cooling are also used for confinement.

Both forced evaporation and this type of Sisyphus cooling are not feasible in traditional dipole traps. However, in the circular FORT the AC Stark shift splits the spin states, and both these cooling mechanisms become possible. In Chapter 6 the preliminary results of cooling in the circular FORT invoking the above methods is described. In this initial work, cooling from 280 μK to 40 μK is observed, due to one or both of the mechansims described above. While substantial number loss accompanied this cooling, optimization of the cooling procedure should improve these initially promising results.

Chapter 2

A Low-Velocity Intense Source of Atoms from a Magneto-Optical Trap

2.1 Introduction

Cold atomic beams are useful in a variety of applications: in ultra-high resolution spectroscopy, as frequency standards, and in studies of cold atomic collisions [46]. An intense beam of cold atoms is valuable for atom interferometers [47], particularly those sensing rotational and gravitational effects. A cold atomic beam coupled into an atom fiber guide [48] will provide much larger guided atom flux. Current experiments studying Bose-Einstein condensation [1] and trapping of radioactive atoms for fundamental symmetry tests [49, 30] require a system of two magneto-optical traps (MOTs) with the capturing and the measurement processes separated in space. Our experiment reveals a simple and efficient way to transfer atoms between two MOT's via a cold atomic beam.

Many examples of cold atomic beams have been demonstrated, such as Zeeman slowers [50, 7], chirped-cooled beams [8], and beams slowed by broadband light [51] or isotropic light [52]. These beams all experience serious transverse diffusion effects as the atoms are slowed to very low velocities ($\lesssim$15 m/s). This causes a loss of atoms and reduced collimation. To counteract these effects, slow atoms are passed through a two-dimensional MOT, or atom funnel, to compress and cool them[20, 22, 23]. To date, the brightest slow beams employ this technique and include a beam of Na atoms traveling 2.7 m/s with a brightness of 3×10^{11} atoms/sr/s[20], and a beam of Ne* traveling 19 m/s with a brightness of 3×10^{10} atoms/sr/s[22]. In contrast, we have created a low-velocity intense source (LVIS) of atoms with a brightness of 5×10^{12} atoms/sr/s. This atomic beam, the brightest beam of atoms moving slow enough to be easily captured by a MOT ($\lesssim$20 m/s), offers the advantage of simplicity, for it is made merely by adding a small modification to the simple vapor cell magneto-optical trap (VCMOT)[15].

In this Chapter we report a detailed study of the LVIS beam. We observed the longitudinal velocity distribution by making time-of-flight studies; and we obtained transverse velocity distributions and absolute measures of both pulsed and continuous brightness by adding atomic beam fluorescence measurements. Our model of the system explains most of our results quantitatively, and all of them qualitatively.

2.2 Description

The LVIS system is nearly identical to a standard VCMOT with six orthogonal intersecting laser beams. The only difference is that one of the six trapping laser beams has a narrow dark column in its center. Atoms in the low-velocity tail of the thermal vapor enter the VCMOT trapping volume and slow down. After they diffuse into the trap center, they enter the central column ("extraction column") and are accelerated out of the trap by the counter-propagating laser beam ("forcing beam"). The velocity of the extracted atoms is determined by the number of photons they scatter from the forcing beam before leaving the trap. A key feature of this scheme is that these extracted atoms are continuously apertured by laser light along the beam. Those diverging atoms that move out of the extraction column are recaptured and returned to the trap center. This mechanism of recycling the diverging atoms provides a very efficient way of transferring trapped atoms into a collimated atomic beam.

The atomic beam flux is determined by the capture rate of the VCMOT. In a conventional VCMOT, the equilibrium number of trapped atoms N_{eq} is the steady-state solution to the differential equation

$$\dot{N} = R - N/r_c.$$

Then $N_{eq} = R/r_c$, where R is the capture rate and r_c is the collisional loss rate[15, 32]. In LVIS, most of the atoms are "lost" into the atomic beam. An additional term is then added to describe the LVIS beam flux $F = N/r_t$, where r_t is the rate of transferring atoms into the beam. The steady-state solution to

$$\dot{N} = R - N/r_c - N/r_t$$

is given by $F=R/(1+r_c/r_t)$. Typically $r_c \ll r_t$, e.g., $1/r_c$ =1.0 sec and $1/r_t$=30 msec, so $F \approx R$.

The collisional loss also affects atoms in the beam. Since it takes much less energy to knock an atom out of the LVIS beam than out of a VCMOT, the beam collisional loss rate is roughly 5 times that of the VCMOT. The trade-off between collection rate of the VCMOT and collisional loss rate from the LVIS beam limits the flux and determines the optimum thermal vapor pressure ($\sim 1 \times 10^{-7}$ Torr). The low-energy collisional cross section in Ref. [53] agrees well with the dependence of collimation and flux on Rb vapor pressure that we observe with LVIS.

2.3 Experimental Setup

A schematic of the ^{87}Rb LVIS apparatus is shown in Fig. 2.1. A Ti:Sapphire ring laser provides about 500 mW of "trapping" light at a typical frequency 30 MHz detuned from the 5s $^2S_{1/2}$(F=2)$\rightarrow$5p $^2P_{3/2}$(F′=3) transition. A diode laser supplies 20 mW of "repump" light, tuned to the 5s $^2S_{1/2}$(F=1)$\rightarrow$5p $^2P_{3/2}$(F′=2) transition. As in a conventional VCMOT, the trapping beam is split into three beams which intersect inside a vacuum chamber containing Rb vapor. Each of the three beams is reflected back in

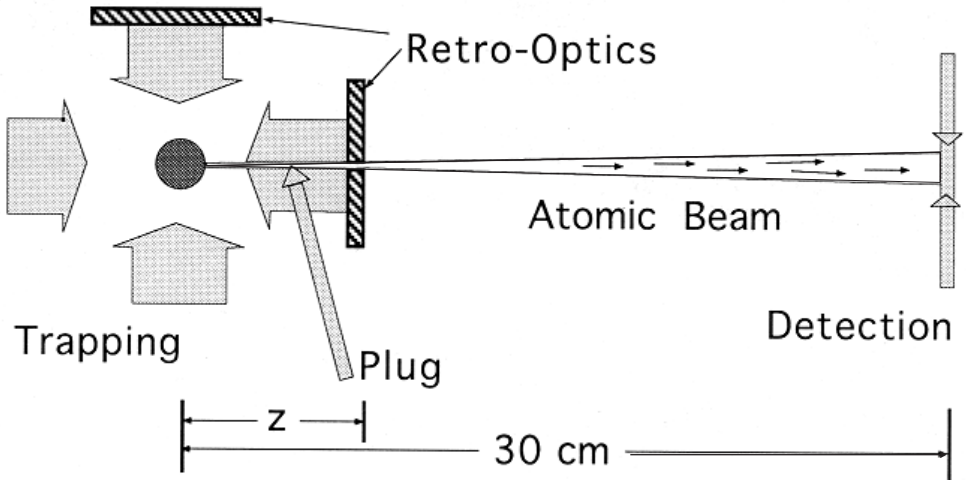

Figure 2.1: Schematic of the LVIS system. Large shaded arrows represent the 4 cm diameter trapping laser beams. A repump laser (not shown) illuminates the trapping volume up to the edge of the retro-optic, which has a small hole and is placed inside the vacuum chamber. This hole, a distance z from the trap center, creates an extraction column through the trap center and causes atoms to accelerate out of the VCMOT. A standing-wave light field 30 cm downstream forms the detection region. The plug is a thin beam of trapping laser light; when present, it prevents atoms from leaving the trap via the atomic beam.

the opposite direction to make six counter-propagating laser beams in a retro-reflecting configuration. The VCMOT beams are relatively large ($\sim$ 4 cm diameter) in order to maximize R. To produce the extraction column, a millimeter sized hole is drilled through the center of one of the retro-reflecting assemblies which consist of a quarter-wave plate and mirror [1] . The atomic beam is extracted from the trapping region through this hole. A pair of anti-Helmholtz coils generates the quadrupole magnetic field for the trap, with a gradient of $\sim$5 G/cm along the atomic beam direction. To position the trap center in the extraction column, the point of zero magnetic field is moved with a set of orthogonal magnetic shim coils. In normal operation, the plug beam is blocked by a mechanical shutter. When making measurements, the plug beam is unblocked so that the atoms are forced out of the extraction column and returned to the center of the trap. This capability of quickly turning the atomic beam on and off allows us to measure the longitudinal velocity distribution, and to run LVIS in a pulsed mode. With a CCD camera and a photo-diode, we monitor the fluorescence emitted when the atoms cross the detection region. This allows us to measure the flux, spatial distribution, and velocity distribution of the atomic beam.

[1] A hole was drilled in the quarter wave plate and then the back surface was coated with a reflecting layer of gold.

2.4 Results

2.4.1 Optimum Detuning

Given the trap parameters described above and in Fig. 2.1, we found that the trapping laser frequency which maximizes the LVIS beam flux is 5 Γ detuned (where Γ is the natural line width) from the cycling transition, while the detuning that maximizes N in the normal VCMOT is 3.2 Γ. This difference presumably occurs because the transverse light beams can heat and, if there are any imbalances, deflect the atomic beam as it exits the trap. At lower detunings, the scattering rates and hence these deleterious effects increase.

2.4.2 Longitudinal velocity

The longitudinal velocity distribution in the LVIS beam, as shown in Fig. 2.2, is measured by the time-of-flight method. Typically, we observe v$\sim$15 m/s, consistent with our simple model based on a calculation of the photon scattering rate from the forcing beam. In our model the acceleration begins when an atom enters the extraction column. As the atom is accelerated, the scattering rate slows due to Doppler shift and Zeeman shift. Scattering and acceleration cease when the atoms finally leave the region of repump light. Figure 2.3 shows the dependence of the longitudinal velocity on the intensity and frequency detuning of the forcing beam. Both plots indicate that the final velocity increases with the scattering rate in a manner consistent with our model. Note that the range of useful velocities is limited because the flux decreases rapidly when the intensity and detuning are far from those which optimize the trap capturing process.

A narrow longitudinal velocity distribution is usually desired in the applications of cold atomic beams. The velocity spread, about 2.7 m/s FWHM, is much larger than the Doppler cooling limit of 0.12 m/s. The velocity spreads due to a random distribution over magnetic sublevels and statistical fluctuations in the number of scattered photons were both estimated to be $\sim$0.7 m/s. We believe the dominant contribution to the longitudinal spread arises because the atoms enter the extraction column within the trap at different positions along the beam axis, and are therefore accelerated over different distances. A calculated velocity and spread match the experimentally observed values (v=14 m/s, FWHM=2.7 m/s) if we assume that the acceleration distance covers the range 2.2 to 3.4 cm. This is reasonable since in this case z is 2.5 cm (see Fig. 2.1), and the atoms trapped in the VCMOT with the plug beam unblocked form a cloud $\sim$1 cm in diameter.

The fractional FWHM of the longitudinal velocity distribution depends on the forcing beam's polarization. Figure 2.4 shows that the fractional FWHM can be minimized by making the polarization significantly elliptical. For circularly polarized light, the Zeeman shift causes an atom to feel an acceleration which is much larger on the upstream side of the trap center than on the downstream side. This principle is essential to the operation of a MOT, but in a LVIS, atoms entering the extraction column on the upstream side experience a larger acceleration than those entering on the downstream side. However, an elliptically polarized forcing beam makes the accelerations more

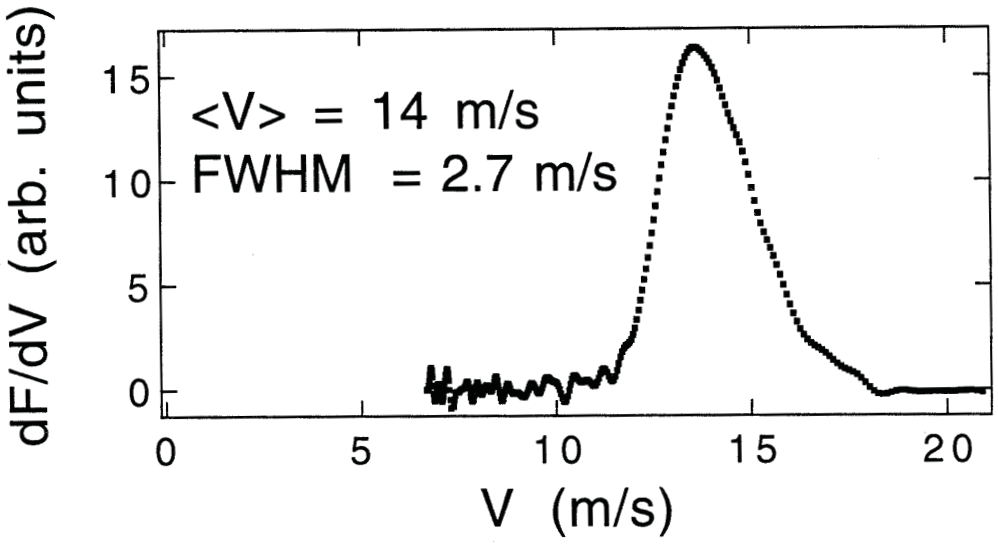

Figure 2.2: A typical longitudinal velocity distribution. In this case, the average velocity is 14 m/s and the FWHM is 2.7 m/s. This curve is made by first recording the shape of the time-of-flight (TOF) signal. The derivative of the TOF signal is then taken with respect to time, and time is converted into velocity using the known distance between the plug and the detection region. This yields the derivative of atom flux with respect to velocity, or the longitudinal velocity distribution.

nearly equal on the upstream and downstream sides. This results in a smaller final velocity spread. For angles $<20^o$ and $>70^o$, the increased spatial spread in the trapped atom cloud outweighs this decreased variation in the acceleration.

2.4.3 Collimation

Many factors contribute at some level to the transverse collimation. Initially we expected transverse cooling and focusing within the extraction column to dominate. Instead, the measurements described below show that the transverse velocity distribution is primarily determined by a simple geometrical collimation mechanism. Although it is similar to the transverse velocity distribution of a conventional atomic beam collimated with physical apertures, the LVIS beam benefits because the apertured atoms are recycled. In LVIS, the collimation length (z) extends from the point where atoms enter the extraction column to the mirror. The divergence angle of the atomic beam, θ, is given by $\theta \approx$d/z, where d is the diameter of the extraction column. The spatial profile is consistent with the triangular profile expected from a geometrical collimation mechanism. When the extraction column was produced by placing the retro-optic with a hole at 2.9 cm from the trap center, the observed divergence angle (36 mrad) agrees well with d/z (40 mrad).

To further study this collimation mechanism, the retro-optic with a hole was re-

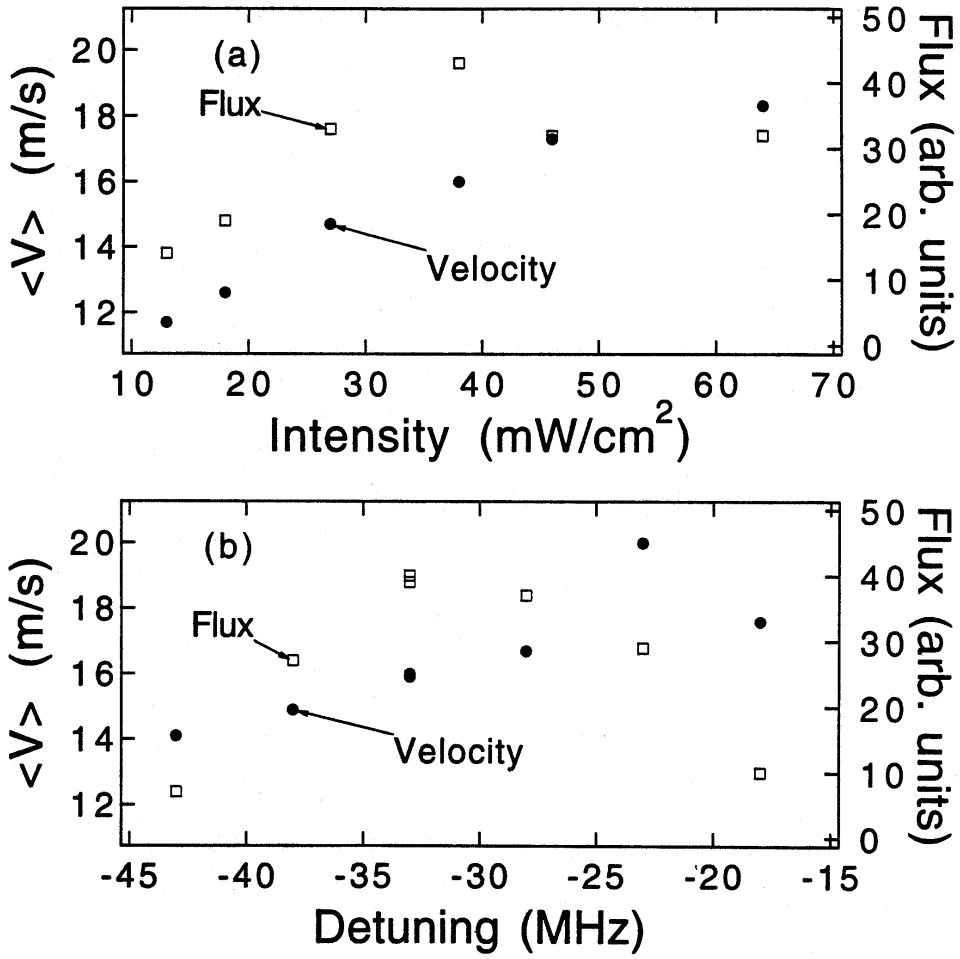

Figure 2.3: The average longitudinal velocity and flux as a function of (a) the forcing laser intensity (with detuning at 32 MHz) and (b) the detuning (with I=38 mW/cm^2). In both cases the final velocity increases with increasing scattering rate from the forcing beam, while the fractional spread remains nearly unchanged.

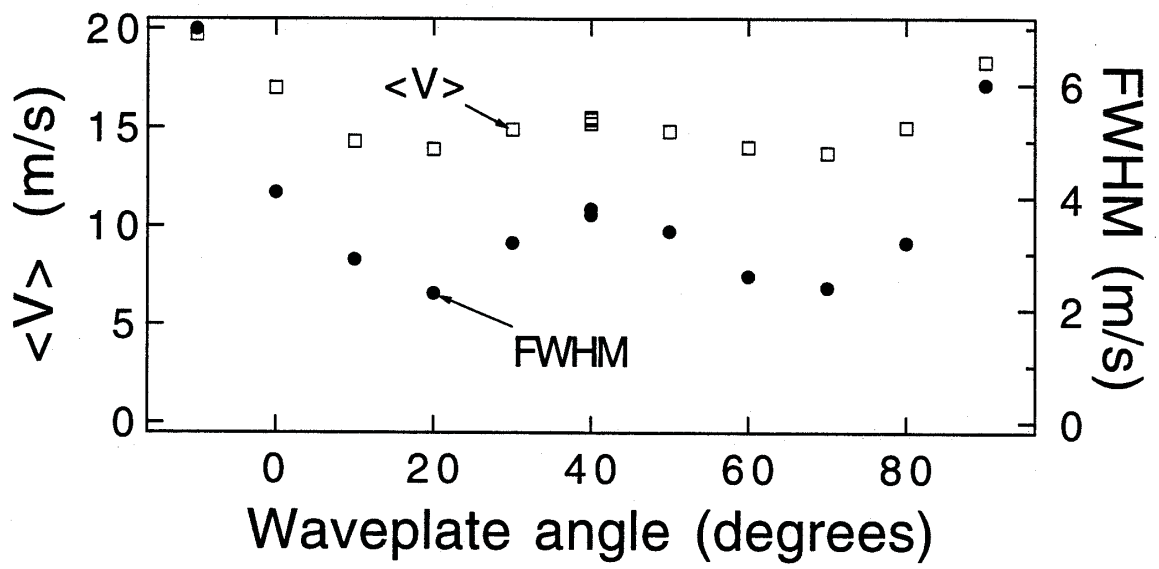

Figure 2.4: The average longitudinal velocity and spread as a function of the forcing beam polarization. The quarter-wave plate at 45^o gives circularly polarized light. Below 10^o and above 80^o the flux falls rapidly because the trap capture rate decreases, but the flux varies by less than 30% between 10^o and 80^o. Also, the mean velocity has a much weaker dependence on polarization than the fractional spread.

placed by a standard retro-optic outside the vacuum chamber. We inserted a piece of glass with opaque spots of various sizes into the laser beam in front of the retro-optic to create the extraction column. To vary the collimation length, we varied the distance (z) over which the repump laser illuminated the atomic beam. The divergence scaled with d/z over a wide range of conditions. Angle vs z is shown in Fig. 2.5. Note that while θ scales as 1/z, the measured values are consistently smaller than the opaque spot diameter divided by z. This is presumably due to diffraction of light into the extraction column which effectively makes d smaller than the diameter of the opaque spot.

The tightest collimation was achieved with our maximum collimation length (30 cm) and a 1.6 mm diameter opaque spot. We observed a divergence angle of 5 mrad, implying a transverse temperature of 20 μK. This configuration requires careful alignment, and the atomic beam must be sent in a vertical direction to prevent gravity from pulling the atoms out of the extraction column.

To better understand the beam collimation, we replaced the conventional MOT field gradient with a quasi-two-dimensional MOT which had a magnetic field gradient of 7 G/cm in the transverse direction and $<$1 G/cm in the longitudinal direction. We kept all other conditions the same. The atomic beam width changed from 1.1 mm to 0.65 mm when measured 3 cm above the trap center, but did not change when measured 30 cm above. Thus the quasi-two-dimensional configuration produced transverse focusing but not cooling.

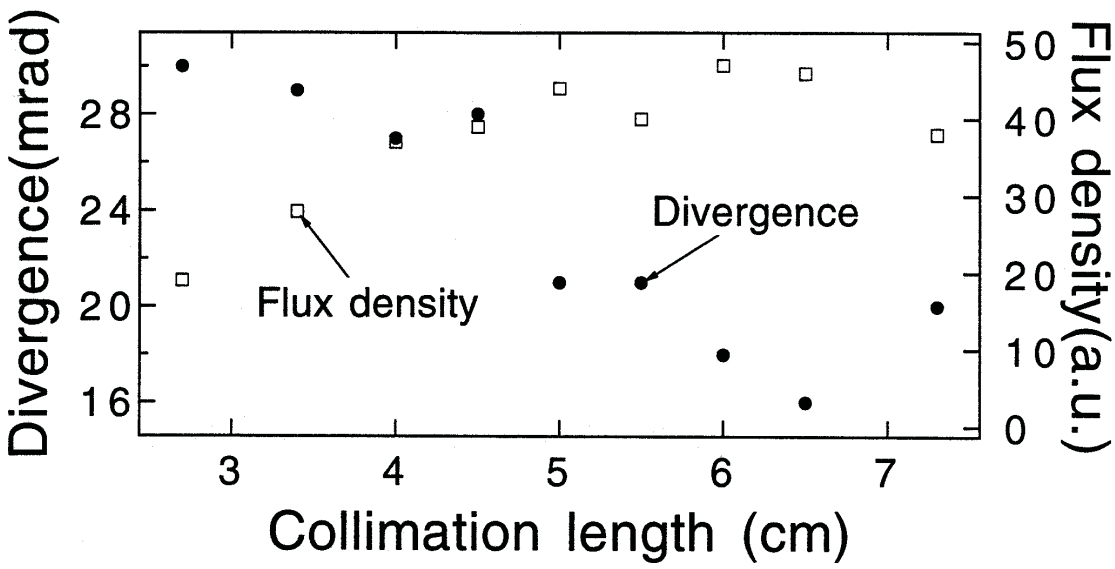

Figure 2.5: The measured divergence angle as a function of the collimation length z. The divergence angle decreases, consistent with a geometrical collimation mechanism. The flux density (in arbitrary units) increases until z≈6 cm, indicating that the atoms are being captured back into the trap and recycled. For these measurements, the retro-optic was removed to the outside of the chamber, and the extraction column was generated by a 1.6 mm opaque spot such that the atoms were accelerated vertically.

2.4.4 Flux

We measured the absolute atom flux in the LVIS beam and determined the atom transfer efficiency by comparing this flux with the capture rate of the VCMOT. The capture rate of the trap was determined from measurements of N and r_c with the plug beam in place. Our measurements indicated that essentially 100% of the atoms were transferred into the atomic beam for typical values of z. However, the fraction extracted through the hole in the retro-optic into a field-free region varied. The highest flux we achieved was 5×10^9/s, with an extraction efficiency of 30% (θ=30 mrad, d=0.7 mm, z = 2.7 cm) which was limited by light scattering around the hole edges. By making a cleaner hole through the retro-optic, (θ= 36 mrad, d=0.8 mm, z=2.0 cm) we increased the efficiency to 70%, but by that time, our deteriorating Ar^+ laser tube allowed us to trap an order of magnitude fewer atoms. However, with this 70% efficiency and ∼500 mW of Ti:Sapphire laser power, we expect to achieve a beam flux $>10^{10}$/s. When operated at lower power the LVIS flux drops in proportion to the reduced capture rate for the MOT. However, the beam collimation and velocity remain nearly the same so LVIS would still produce a nice beam with low power diode lasers. Finally, we observed a much higher peak flux when the LVIS system was operated in a pulsed mode. In these geometries, the VCMOT empties in 50 ms, providing nearly the same time-averaged flux but ten times the peak flux and brightness.

The flux and flux density depend on the collimation angle and geometry of the LVIS setup in the manner predicted above. Although we achieved 70% extraction efficiency when θ=36 mrad, we only achieved a transfer efficiency of 20% when θ=5 mrad. Figure 2.5 shows the tradeoff between flux density and collimation of the atomic beam. Recycling causes the flux density (number s^{-1} cm^2) at the detection region to increase while the divergence decreases. Total flux decreases beyond 4.5 cm because for a collimation this tight, the atomic beam transverse temperature becomes comparable to the temperature of atoms in the VCMOT. With tight collimations, an atom must make many more attempts to be successfully transferred into the atomic beam. This makes r_c/r_t larger, decreasing the flux as predicted.

2.5 Conclusion

We have created a slow, bright beam of cold atoms. We have observed the optimum detuning, beam collimation, and flux, and find them consistent with a geometrical collimation mechanism. A quasi two-dimensional quadrapole magnetic field did not improve the collimation. Finally, up to 70% of the atoms loaded into the MOT were continuously extracted into the beam, consistent with a recycling mechanism. The simplicity, brightness, and versatility of LVIS will make it useful in a wide range of applications.

Chapter 3

Efficient Collection of ^{221}Fr into a Vapor Cell Magneto-optical Trap

3.1 Introduction

There has recently been considerable activity in the field of laser trapping of short-lived radioactive atoms. While a wide range of isotopes are being pursued, laser trapping of ^{21}Na [49], ^{37,38}K [54], ^{79}Rb [3], and ^{209,210,211}Fr [55] atoms has been experimentally realized. Efficient optical trapping is essential for creating large samples of rare atoms. Such samples are very appealing for tests of the standard model including atomic parity non-conservation (PNC), the electric dipole moment (EDM), and β decay [49]. Francium, which has no long-lived isotopes, is particularly interesting for these tests, because calculations predict PNC amplitudes and EDM enhancements to be 10 times larger in Fr than Cs [56, 57]. In this letter we demonstrate efficient trapping of ^{221}Fr. The general approach should work as well with any alkali isotope, and should make tests of the standard model possible in rare trapped atoms.

Various techniques have been developed to collect atoms into traps [7, 8], but since short-lived radioactive atoms are only available in limited quantities, improving the optical trap collection efficiency is a central issue. The highest efficiency yet demonstrated used a vapor cell magneto-optical trap (VCMOT) [15] in a glass cell coated with dryfilm. Using coated cells, Stephens *et al*. [30] and Guckert *et al*. [58] have demonstrated respectively 6% and 20% collection efficiencies of stable cesium. Similar techniques have been applied to trapping radioactive species of K, Rb, and Fr atoms [54, 3, 55], but with far lower trap efficiencies. We have created a highly efficient (56%) ^{221}Fr VCMOT in a coated cell and used it in spectroscopic measurements on ^{221}Fr.

A conventional VCMOT [15] traps a very small fraction of the available atoms. To obtain high collection efficiency, one must raise the collection rate and lower the vapor loss rate. The dependence and optimization of collection rate on various trap parameters has been previously investigated[32]. To have a high collection rate, a trap should have large, high-power laser beams. The trapping cell should be designed to maximize the ratio of the trap volume (region of laser beam overlap) to the cell surface area. To minimize the loss rate from the cell, the opening through which the radioactive atoms enter the cell must be small enough to minimize the leak rate, and the loss of atoms via adsorption to the glass walls must be significantly reduced. The latter is accomplished by coating the glass surfaces with dryfilm coatings made of silicon-based hydrocarbon polymers, which are then “cured” by exposure to alkali vapor. [31]

3.2 Theory

The analysis of the capture process differs from that of a conventional VCMOT. In a highly efficient VCMOT, the number of atoms in the vapor and the number of atoms in the trap are so strongly coupled that the vapor density cannot be considered constant. The time evolution of such a coupled system of N_t atoms in the trap and N_v atoms in the vapor depends on three rates: L, the loading rate of atoms from the vapor to the trap; C, the loss rate of atoms from the trap to the vapor due to collisions with background vapor atoms; and W, the loss rate of atoms from the vapor to the cell walls or out of the cell. In the case where a constant flux, I, of atoms enter the cell, the dependence can be described by two coupled differential equations:

$$\frac{d(N_t)}{dt} = -CN_t + LN_v,$$

$$\frac{d(N_v)}{dt} = CN_t - LN_v - WN_v + I.$$

The time evolution of the number of trapped atoms follows a double-exponential function,

$$N_t(t) = a_1 e^{-k_1 t} + a_2 e^{-k_2 t} + \frac{LI}{WC},$$

where $k_1 + k_2 = L + C + W$ and $k_1 k_2 = WC$. N_t(t=0) and N_v(t=0) fully determine a_1 and a_2. We define trap efficiency (η) as the probability of trapping an atom that has entered the cell,[1]

$$\eta = \frac{L}{(L+W)} = \frac{CN_t}{(CN_t + I)}.$$

3.3 Experimental Setup

3.3.1 Fr Source

The ^{221}Fr nuclei are produced in the decay chain

$$^{229}\mathrm{Th}(\mathrm{t}_{1/2} = 7300\mathrm{y}) \xrightarrow{\alpha} {}^{225}\mathrm{Ra}(\mathrm{t}_{1/2} = 15\mathrm{d})$$
$$\xrightarrow{\beta} {}^{225}\mathrm{Ac}(\mathrm{t}_{1/2} = 10\mathrm{d}) \xrightarrow{\alpha} {}^{221}\mathrm{Fr}(\mathrm{t}_{1/2} = 4.9\mathrm{min}).$$

In order to produce a portable ^{221}Fr source with short-lived radioactivity, ^{225}Ac was first extracted out of a long-lived ^{229}Th sample, and deposited onto a small piece of platinum using one of two methods. Results reported here were obtained from a sample of ^{225}Ac chemically extracted from a ^{229}Th solution [59] and electroplated onto a Pt ribbon. In our preliminary measurements, we used ^{225}Ac implanted onto Pt via electrostatic collection [33]. The Pt ribbon was then placed in the cavity of an orthotropic oven [33] where ^{221}Fr daughters were continuously produced and distilled into a collimated

[1] Ref. [30] defines a recapture efficiency which is in general lower than η, but equal to η in the limit of a small collisional loss rate (C$\ll$L,W)

atomic beam. At the beginning of the experiment, the oven was loaded with 50 μCi ^{225}Ac, which produced 2×10^6 s^{-1} of ^{221}Fr inside the oven. The full divergence angle of the atomic beam exiting the oven was measured to be 180 mrad. By counting the α particles from the decay of the ^{221}Fr, we measured a ^{221}Fr atomic beam flux of 3.8×10^4 s^{-1}, or about 2% of the ^{221}Fr atom production rate inside the oven. Thirty days later, at the end of the experiment, the ^{221}Fr beam flux was 5.1×10^3 s^{-1}, reflecting a decrease matching the natural decay of ^{225}Ac.

3.3.2 The Magneto-optical Trap

A schematic of the apparatus is shown in Fig. 3.1. Both the francium oven and the vapor cell were situated inside a chamber where the vacuum was maintained at 2×10^{-8} Torr even when the oven was heated to the operating temperature of 1050 ^{o}C. The cell was a quartz glass cube (4.4 cm inside dimension) whose top lid could be opened and closed via a mechanical feedthrough. Following the recipe developed by Stephens *et al.*[31], the cell walls were coated with a short-chain dryfilm called SC-77 (Silar Laboratories), and then cured by opening the cell lid and maintaining a Rb vapor in the cell at about 2×10^{-7} Torr for ten hours. The Fr atoms from the oven entered the cell through a 2 mm diameter hole at a lower edge of the cell. Over several days, the coating performance deteriorated, reducing the number of trapped Fr atoms by a factor of 3. This damage to the coatings could be attributed to heat or material evaporating from the oven, and was repaired by providing a continuous, low level curing with $\sim 1 \times 10^{-8}$ Torr of rubidium in the cell.

Up to 1W of light from a Ti:Sapphire ring laser was tuned to the D_2 line of Fr at 718 nm for trapping. The laser frequency was locked to the side of a Doppler-broadened I_2 absorption peak[60] that conveniently covered the frequency of the $7S_{1/2}$, F=3 $\rightarrow$ $7P_{3/2}$, F=4 cycling transition (Fig. 3.2). In addition, an SDL 100 mW diode laser at 817 nm was tuned to the D_1 line to pump atoms out of the $7S_{1/2}$, F=2 state. The frequency of the diode laser was tuned to the $7S_{1/2}$, F=2 $\rightarrow$ $7P_{1/2}$, F=3 transition and locked to a Fabry-Perot cavity, which was in turn actively stabilized to the rubidium D_2 line. This lock is described in detail in Appendix B.

3.3.3 Sensitive Detection

We assessed the performance of the wall coatings and found the correct laser frequencies by observing fluorescence from the room-temperature Fr vapor. We used an optical-optical double resonance technique to separate the fluorescence from light scattered off the cell walls. For this technique, a beam from the Ti:Sapphire laser was sent through the center of the cell, while its frequency scanned over one Doppler width (300 MHz) about the $7S_{1/2}$, F=3 $\rightarrow$ $7P_{3/2}$, F=4 cycling transition. A 60 mW beam from the 817 nm diode laser, chopped at 100 Hz, co-propagated and overlapped the Ti:Sapphire beam through the cell. The diode laser frequency was tuned close to the $7S_{1/2}$, F=2 $\rightarrow$ $7P_{1/2}$, F=3 transition to pump atoms from the $7S_{1/2}$, F=2 to the $7S_{1/2}$, F=3 state. The population of the $7S_{1/2}$, F=3 state was therefore fully modulated for

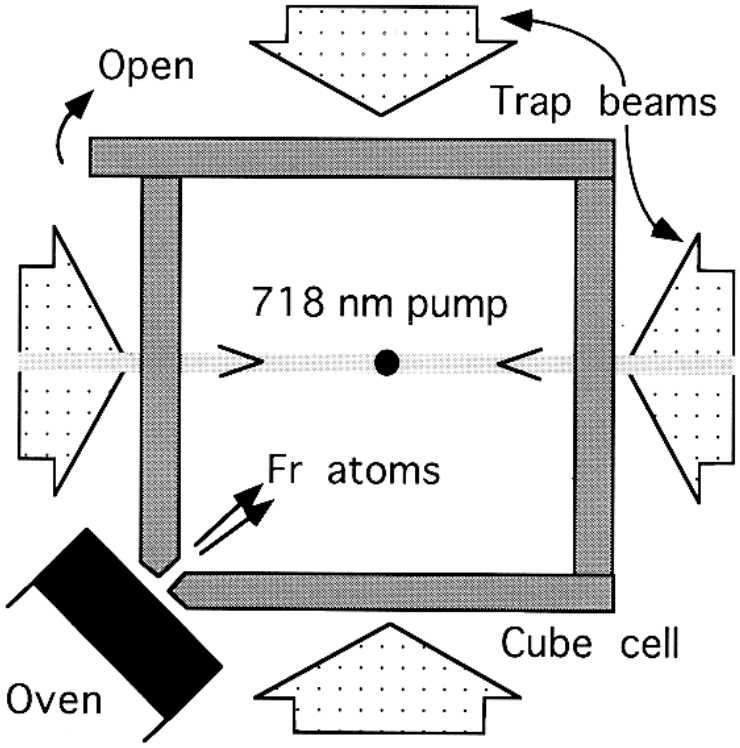

Figure 3.1: A diagram of the ^{221}Fr trap setup. Both the oven and the cell were situated inside a vacuum chamber with 10 cm diameter windows. The same oven and cell assembly was used for the ^{221}Fr vapor fluorescence measurements.

the group of atoms in resonance with both laser beams. Because this was a narrow velocity group, the resulting resonance feature was sub-Doppler (50 MHz FWHM). The resulting modulated fluorescence at 718 nm generated near the center of the cell was imaged onto a low noise photo-diode through a 718 nm interference filter and demodulated with a lock-in amplifier. Thus we were capable of detecting as few as 600 atoms in the entire cell, or equivalently 1 Fr atom in resonance in the viewing region, with a signal to noise ratio (SNR) of $1/\sqrt{s}$. By monitoring the exponential buildup of the number after the cell lid was closed, we determined the loss rate of Fr atoms from the vapor (W) to be 1.59(9) s^{-1}, and a constant flux of 2.3×10^3 s^{-1} Fr atoms entering the cell.

We then trapped the Fr atoms in a VCMOT using 4 cm diameter laser beams. These beams provided a six-beam-total intensity of up to 110 mW/cm^2 in the cell. In addition, a 60 mW, 4 cm diameter beam from the diode laser at 817 nm was sent through the cell four times along two normal axes of the cube cell. A set of anti-Helmholtz coils generated the MOT quadrupole field gradient of $\sim$7 Gauss/cm.

The laser light scattered from the six cell walls made detection of the 718 nm fluorescence from the trapped Fr atoms impossible. Instead, to further avoid scattered light and thereby increase our sensitivity, we imaged the 817 nm repump fluorescence

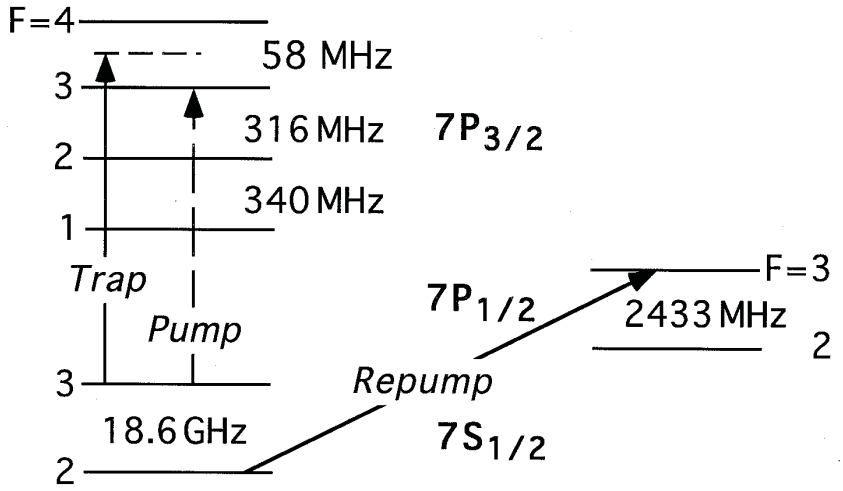

Figure 3.2: The atomic level diagram of ^{221}Fr. In our ^{221}Fr trap, the trap laser (718 nm) was tuned to $\sim$ 30 MHz below the $7S_{1/2}$, F=3 $\rightarrow$ $7P_{3/2}$, F=4 cycling transition, and the repump laser (817 nm) was tuned to the $7S_{1/2}$, F=2 $\rightarrow$ $7P_{1/2}$, F=3 transition. To detect the trapped atoms, a 718 nm pump beam (2 mm diameter, 50 mW/cm^2), tuned to the $7S_{1/2}$, F=3 $\rightarrow$ $7P_{3/2}$, F=3 transition, was chopped to modulate the 817 nm fluorescence from the trap.

from the trapped atoms onto a photodetector. This light was observed through a cell window not illuminated by any repump beams and through a 817 nm bandpass interference filter. The 817 nm fluorescence was modulated using a small, frequency-shifted 718 nm pump beam that was chopped and retro-reflected through the trap center (see Fig. 3.1). This beam increased the fractional population in the $7S_{1/2}$, F=2 state to 70% without affecting the trap loading rate. This detection scheme allowed us to detect as few as 15 trapped Fr atoms with a SNR of $1/\sqrt{s}$ in the presence of large amounts of scattered light. The trap contained an estimated 900 atoms, but this is a lower limit assuming that both the 718 nm pump and the repump lasers were tuned to resonance. This trapped atom sample could be maintained for many hours.

3.4 Results

3.4.1 Trapping Efficiency

Figure 3.3 shows a trap loading curve fitted to the double-exponential function predicted by our model. The fit gives the trap rate constants, from which we calculate the trapping efficiency to be $\eta = \frac{L}{(L+W)} = 56(10)\%$. As a check, $\eta = \frac{CN_t}{(CN_t+I)}$ gives a lower limit of 30% assuming the repump laser is tuned to resonance, but can be as high as 50% when plausible detunings are assumed in calculating N_t. The atomic fluxes at various stages of the experiment are listed in Table 3.2, showing a total efficiency of 0.4% from production to trapping. Engineering improvements in the oven and in the

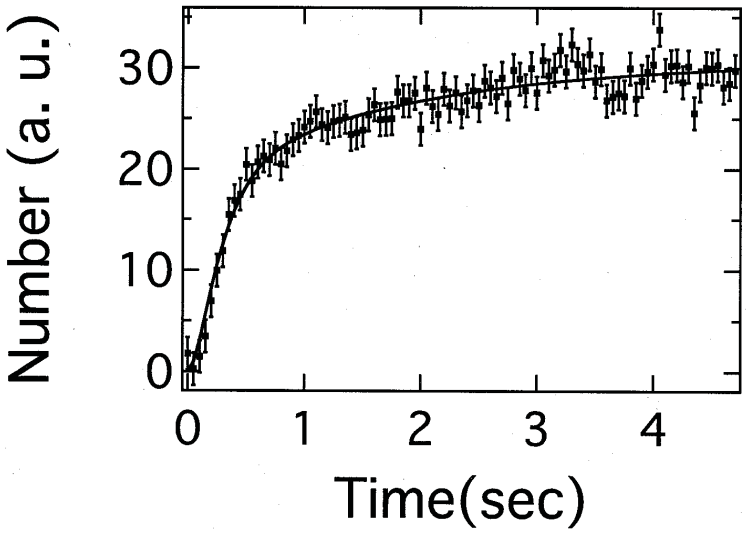

Figure 3.3: The number of atoms (in arbitrary units) loaded into a ^{221}Fr trap vs. time. In a trap with a high collection efficiency, the loading signal is expected to be a double-exponential function. Because the signal was filtered by a low-pass network with a time constant τ = 100 ms, it was fitted with the function b_1[1-exp(-k_1t)] + b_2[1-exp(-k_2 t)] - τ[b_1k_1 + b_2k_2][1 - exp(-t/τ)]. The best fitting results were k_1 = 4.8(1.0) s^{-1} and k_2 = 0.57(23) s^{-1}. Combining these rates with the measured result that on average a Fr atom stayed in the vapor for 1/W = 0.63(4) s, we derived that, on average, a Fr atom stayed in the trap for 1/C = 0.58(27) s and it takes 1/L = 0.48(19) s to load a Fr atom from the vapor into the trap. These rates are consistent with those found in Rb traps, and imply a trap efficiency of L/(L+W) = 56(10)%.

coupling into the cell would significantly improve the total efficiency. An orthotropic source has operated with a 15% efficiency, and 50% (limited by diffusion of Fr into the oven walls) is theoretically possible[33].

3.4.2 Spectroscopy

We have made spectroscopic measurements on ^{221}Fr using our apparatus. In the thermal vapor, we measured the hyperfine splittings of the $7P_{3/2}$ and $7P_{1/2}$ levels. We observed the individual hyperfine transitions by scanning the 718 nm laser, while the 817 nm diode laser was set (to either the F=2$\rightarrow$F'=3 or F=2$\rightarrow$F'=2 transition) to select one velocity group of atoms. We obtained the splittings by measuring the frequency differences between each hyperfine line (Table 3.1) using a high-resolution λ-meter[61]. By checking against known splittings and wavelengths in rubidium, we found the accuracy of the λ-meter to be 3 MHz or less when measuring small differences, but 50 MHz when measuring absolute frequency. This is because uncertainties in the refractive index of air and laser beam alignment are largely canceled in a frequency difference measurement.

Table 3.1: Various rates, fluxes, and efficiencies on Dec. 17-18, when the source strength was 9 μCi. Total efficiency is 0.4%. Data in row (4) are deduced from flux entering cell and trap efficiency.

	Stage	^{221}Fr Flux (s^{-1})	Efficiency
(1)	Produced in oven	3.3×10^5	
(2)	Exit oven	7×10^3	2% of (1)
(3)	Enter cell	2.3×10^3	33% of (2)
(4)	Collected into trap	1.3×10^3	56% of (3)

Using the trapped atoms as a frequency reference, we have measured the wavenumbers of the D_1 and D_2 transitions of ^{221}Fr (Table 3.1). While the wavenumber of the D_1 transition measured here is in agreement with the number measured by the ISOLDE collaboration[62, 63], our value of the D_2 transition is lower by 3 σ_{STD}. As a check on our calibration, we measured the wavenumber of the I_2 line that is only 0.5 GHz away from the D_2 trapping transition and found an excellent agreement (difference = $1(3)\times10^{-3}$ cm^{-1}) with the I_2 atlas[60].

3.5 Conclusions

We have demonstrated and analyzed the dynamics of highly efficient collection of short-lived radioactive alkali atoms in an optical trap. The techniques used here, including the optimized VCMOT, the orthotropic source, and sensitive detection, can be easily applied to other alkalis as well [2] Future applications will likely employ immediate, efficient transfer of trapped atoms out of the cell into a much longer-lived trap (see, for example, Refs. [18, 24, 64] and Chapter 2. By combining a stronger and currently available ^{221}Fr source (flux $\sim 10^6$/s) with a double-MOT system (trap lifetime $\sim 10^2$ s), a sample of 10^8 trapped ^{221}Fr atoms could be prepared for the next generation of

[2] Most alkalis would be easier than ^{221}Fr, which has an unusually small excited state splitting combined with a large ground state splitting.

Table 3.2: The hyperfine constants and wavenumbers of ^{221}Fr. The wavenumbers of the previous work were derived from the published wavenumbers of ^{212}Fr and isotope shifts [17].

	ISOLDE [62, 63]	Current Work
A ($7P_{3/2}$) MHz	65.4(2.9)	66.5(0.9)
B ($7P_{3/2}$) MHz	-259(16)	-260.0(4.8)
A ($7P_{1/2}$) MHz	808(12)	811.0(1.3)
σ (D_1) cm^{-1}	12236.6601(20)	12236.6579(17)
σ (D_2) cm^{-1}	13923.2118(20)	13923.2041(17)

high precision spectroscopy measurements to test fundamental symmetries.

Chapter 4

Spin-Polarized Atoms in a Circularly Polarized Optical Dipole Trap

4.1 Introduction

Many precision measurements require spin-polarized neutral atoms and would be improved with trapped samples. However, no trap provides the necessary characteristics: atomic spin-polarization, tight confinement, ease of control, and a low photon-scattering rate. An imbalanced magneto-optical trap (MOT) has some modest polarization [65], and small spin-polarized samples have been maintained with repeated optical pumping cycles in standard dipole traps [66]. Magnetic traps can confine spin-polarized samples, and offer the advantage of RF transitions between non-degenerate Zeeman states that can be used to drive a variety of cooling schemes, including evaporative cooling and gravitational Sisyphus cooling [67, 45]. Unfortunately, magnetic traps have relatively weak spring constants, and strong magnetic fields are often undesirable and difficult to rapidly control. In contrast, an optical far-off resonance trap (FORT) [38, 39] offers superior confinement and rapid control. As noted in Ref. [43], a dipole trap made with circularly polarized laser light offers all the advantages of an optical trap, plus energy splittings between spin states that make cooling schemes possible in an inherently spin-polarizing trap. In this chapter, we report the creation of such a spin-polarizing FORT for Rb atoms using circularly polarized light.

4.2 Theory

A conventional FORT consists of a linearly polarized laser beam focused to a tight waist [38, 39]. Due to a spatially varying AC Stark shift, laser light tuned below an atom's resonant frequency attracts the atom to regions of high intensity. For alkali atoms in linearly-polarized light fields, the potential is the same for all internal spin states of the atom in the ground n ($S_{1/2}$) electronic state [1] . This degeneracy is lifted when the light is circularly polarized; the laser field acts as a "fictitious magnetic field" [42]. When the laser is tuned between the D_1 (n $S_{1/2} \rightarrow$ n $P_{1/2}$) and D_2 (n $S_{1/2} \rightarrow$ n $P_{3/2}$) transitions, the energy splitting between the spin states is largest (Fig. 4.1). Also, the absorption of the circularly polarized FORT photons optically pumps the atoms into the deepest potential of the $F = 3$ manifold, shown for σ_+ polarization in Fig. 4.2.

[1] This is true if the laser detuning is much larger than the hyperfine splitting.

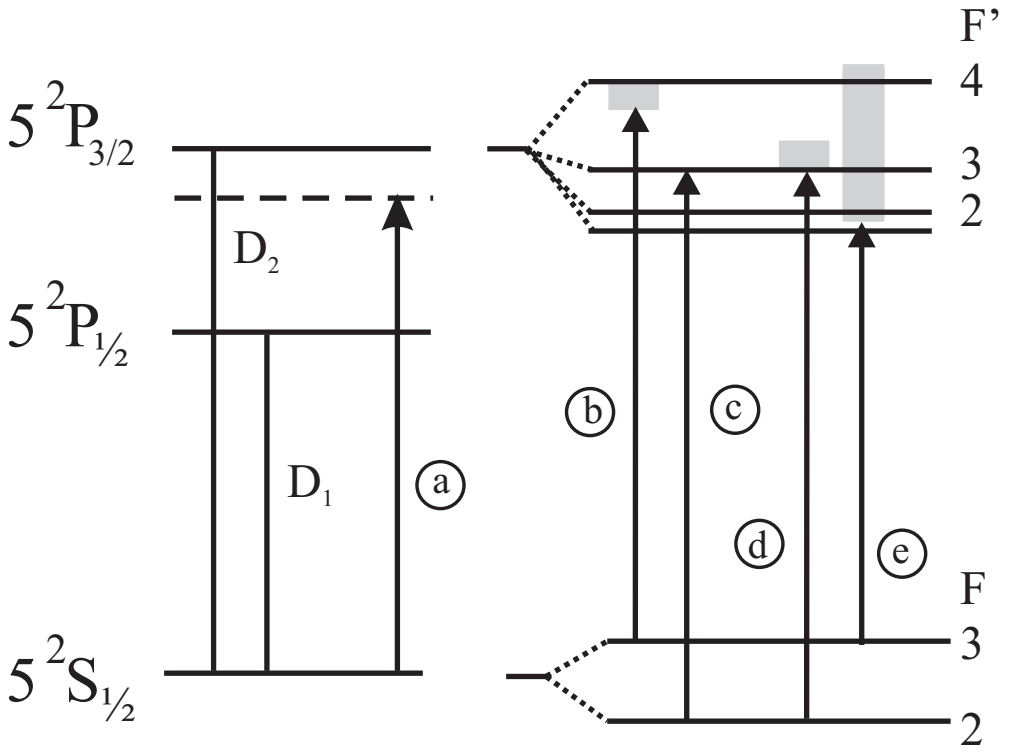

Figure 4.1: Schematic level diagram for ^{85}Rb (I= $5/2$). Laser beams are identified in the text as (a) FORT at 784.1 nm, (b) MOT cooling, (c) MOT repump, (d) transfer, and (e) probe. In vacuum, λ_{D_2} = 780.2 nm, λ_{D_1} = 795.0 nm [68].

The potential energy of atoms in an elliptically polarized FORT may depend on the laser polarization vector $\hat{\varepsilon} \equiv 1/\sqrt{2}(\hat{x}\sqrt{1+\epsilon} + i\hat{y}\sqrt{1-\epsilon})$, with ϵ the ellipticity. [2] The potential depth $U_0(I, \lambda, F, m_F, \epsilon)$ is then

$$U_0 = \frac{\hbar\gamma I_0}{24 I_S}[(\frac{1}{\delta_{\frac{1}{2}}} + \frac{2}{\delta_{\frac{3}{2}}}) - g_F\, m_F \sqrt{1-\epsilon^2}(\frac{1}{\delta_{\frac{1}{2}}} - \frac{1}{\delta_{\frac{3}{2}}})] \tag{4.1}$$

where the natural line width $\gamma = 2\pi$ 6.1 MHz in Rb, m_F is the Zeeman sublevel of the atom, g_F = [F(F+1) + S(S+1) - I(I+1)]/[F(F+1)], the saturation intensity $I_S = 2\pi^2\hbar c\gamma/(3\lambda^3)$, and the intensity $I_0 = 2P/(\pi w_0^2)$ in terms of power P. [3] The detunings $\delta_{1/2}$ and $\delta_{3/2}$ (in units of γ) represent the difference between the laser frequency and the D_1 and D_2 transition frequencies, respectively. Figure 4.3 shows U_0 versus the laser wavelength for each m_F level. The potentials are described in terms of the Gaussian beam waist w_0 by

$$U(\rho) = U_0 \exp(-2\rho^2/w_0^2), \tag{4.2}$$

[2] ϵ is measured by rotating an analyzing polarizer in the laser beam and recording the highest and lowest power (P_h and P_l) transmitted through the analyzer. Then $\epsilon = (P_h - P_l)/(P_h + P_l)$.

[3] Equation (4.1) is obtained by rewriting the expression for U_{AC} in Ref. [43] in terms of experimentally accessible quantities. For $\epsilon = 1$, Eq. (4.1) agrees with the expressions for U_0 in Ref. [69].

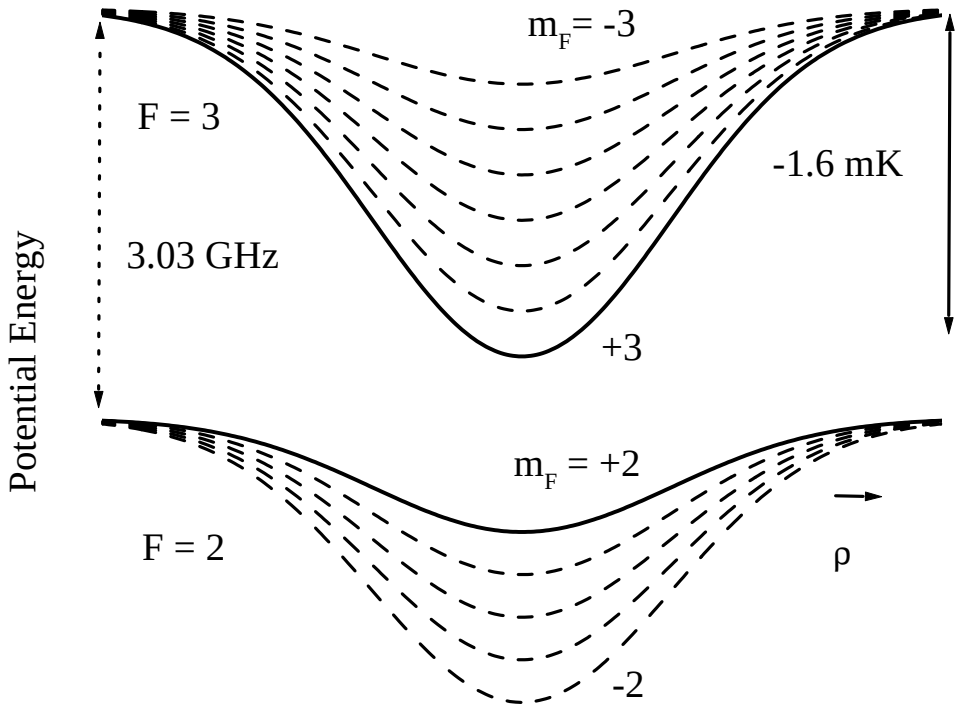

Figure 4.2: AC Stark shift $U(\rho)$ in the focus of a circularly polarized Gaussian laser beam for both hyperfine levels in the ^{85}Rb 5 ^{2}S$_{1/2}$ ground state ($g_3 = 1/3$) under typical experimental parameters, for P = 240 mW. Solid lines indicate the spin states toward which the atoms are driven by absorption of the trapping light.

where $\rho = \sqrt{x^2 + y^2}$ is the radial spatial coordinate. Radial cross-sections of these potentials for ^{85}Rb are plotted in Fig. 4.2.

4.3 Experimental Setup

4.3.1 The Lasers

The experimental apparatus is shown in Fig. 4.4. The MOT [14, 15] collects Rb atoms from a 5×10^{-10} torr vapor, and contains a maximum of $\sim 3\times10^8$ atoms in steady state with a filling time constant of $\sim$12 s. The MOT is made with two external-cavity diode lasers stabilized to atomic lines in Rb at 780 nm with a dichroic atomic vapor laser lock (DAVLL)(See Ref. [70] and Appendix A), which allows rapid and convenient tuning over $>$ 100 MHz range. One laser, the "cooling" laser, provides 6 mW (divided between three retro-reflected beams) and is tuned to 5 ^{2}S$_{1/2}$ $F = 3 \rightarrow 5\,^2$P$_{3/2}$ $F' = 4$. A second laser, the "repump" laser, is tuned to 5 ^{2}S$_{1/2}$ $F = 2 \rightarrow 5\,^2P_{3/2}$ $F' = 3$. Both the cooling and repump lasers pass through acoustooptical modulators (AOMs) to control their power.

The dipole trap with adjustable polarization is created from up to 1 W of laser

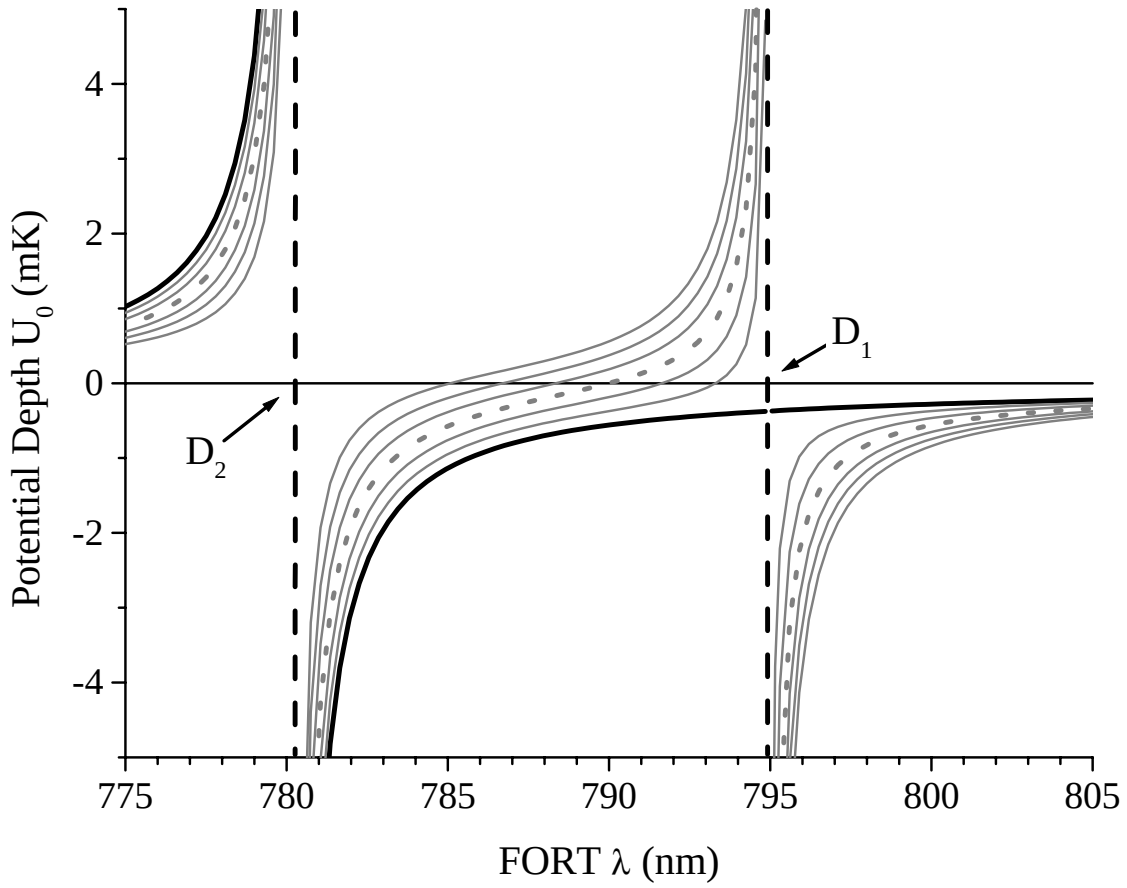

Figure 4.3: Maximum FORT Potential depth as a function of FORT wavelength, for the F=3 manifold with the following laser parameters; P = 600 mW, w_0 = 26 μm. The darkest line indicates the potentials for m_F = +3, into which the atoms are optically pumped by the FORT beam. The dashed line indicates the potential for atoms in the m_F = 0 state, which are insensitive to polarization.

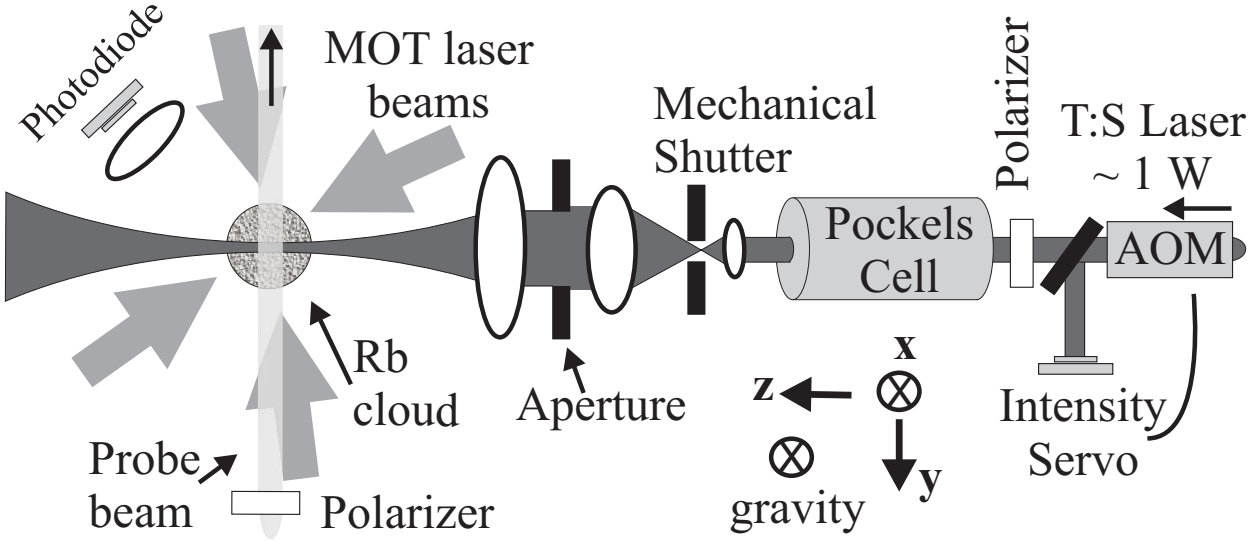

Figure 4.4: Schematic of the experimental apparatus. A “transfer” laser, not shown, counter-propagates with the FORT laser. Also not shown, a two-mirror periscope after the aperture elevates the FORT laser beam and turns it 90^o. (See text.)

light from a Titanium:Sapphire laser, typically tuned to 784.1 nm. The laser beam passes through an AOM and the output power in the first diffraction order (70%) is usually actively stabilized to prevent parametric heating in the trap[71]. This beam passes through a Glan-Thompson polarizer and into a Pockels cell, which acts as a quarter-wave retarder when the applied voltage is about 2200 V. This voltage can be switched in a matter of 100 ms using a Hg relay. A mechanical shutter follows that can turn the FORT off in 60μs. Finally the FORT beam (ω_0 = 4.2 mm) is incident on an aperture and then a cemented doublet (f = 18 cm) that focuses it to w_0 = 26 μm.

The FORT laser beam waist w_0 is measured by inserting a mirror after the doublet lens such that the FORT laser comes to a focus outside the chamber. A razor blade is then translated across the beam while monitoring the position of the blade x and the amount of power that is not blocked by the razor blade $P(x)$. The resulting data are fit to the following function $P(x) = P_{\max}/2[1\pm\text{erf}(\sqrt{2} \times (x - x_c)/w)]$ to determine the width w of the beam. This measurement was repeated at many longitudinal positions until the narrowest waist w_0 was found. By examining the dependence of w on z, the effective Raleigh range could be found. This often exceeded the Raleigh range calculated from w_0 using Gaussian optics [72] by as much as a factor of 3, perhaps due to aberrations in the lens.

4.3.2 The Pockels Cell and Polarization Issues

Establishing the proper polarization of the laser using a Pockels cell requires precision and patience. As will be shown later, a very well-defined polarization is essential to the performance of the circular FORT. This requires careful alignment of the Pockels cell. Our Pockels cell comes from Cleveland Crystals, model number Q1020S. As with all Pockels cells, it relies on the Pockels effect [73], which is a birefringence induced in a crystal that is proportional to the applied voltage. This linear effect is present only in crystals that lack a center of symmetry, such as KDP and KD*P.

To align the Pockels cell, first two crossed polarizers are aligned in the FORT beam such that the first polarizer gives maximum transmission and the analyzer provides extinction. Next, the Pockels cell is inserted in the beam between the polarizers and a large voltage (approximately the λ/2 voltage if safely possible) induces birefringence. Then the cell is rotated until extinction is again observed after the analyzer. This establishes that the "fast axis" of the cell is aligned with the incident polarization. The cell is then rotated such that the fast axis is at a 45^o angle with respect to the incident polarization. The applied voltage is reduced to nearly the nominal λ/4 value and then adjusted until λ/4 voltage is obtained, and the polarization is as nearly circular as possible. Figure 4.5 shows the measured polarization ellipticity as a function of applied voltage.

The angle that the cell's longitudinal axis makes with the laser's direction of propagation is also important. One alignment trick is to place a piece of cellophane tape across the input port of the Pockels cell. This creates diffuse, unpolarized scattered light at the input, some of which passes through the Pockels cell. If a piece of paper is placed along the beam path after the analyzing polarizer, the diffuse light forms a large round

spot. When the Pockels cell has a large applied voltage, a cross-shaped interference pattern appears in the diffuse spot when it is viewed through the analyzing polarizer. By tilting and translating the Pockels cell, this cross shape can be centered within the diffuse spot. The incoming laser beam, when not passing through the transparent tape, should also strike the center of the cross. To perform this alignment, it is necessary to insert and remove the transparent tape repeatedly.

By iteratively rotating, tilting, and translating the Pockels cell, optimum alignment can be obtained, in which the light can be switched from completely linear to completely circular by changing the applied voltage. However, after the Pockels cell a periscope composed of two mirrors is required to elevate the beam so that it can enter the vacuum chamber. This presents a problem because mirrors induce large, angle- and polarization-dependent phase shifts in reflected beams, they are therefore not in general polarization-preserving. However, the polarization can be preserved by using two gold-coated mirrors each of which reflects the beam at right angles such that the final beam is above and perpendicular to the incoming laser beam. By monitoring the polarization after the periscope and the vacuum chamber, small changes in the periscope alignment can be used to optimize the polarization. Residual phase shifts in circular light induced by the periscope can also be compensated by the Pockels cell voltage, as in Fig. 4.5. Any time the alignment of the laser through the periscope changes, one must verify the $\lambda/4$ voltage. In measuring the beam polarization, one must use high-quality polarizers such as calcite Glan-Thompson polarizers. It is also important to use the entire laser beam when measuring the polarization, because both the periscope and the Pockels cell can introduce non-uniformity in the polarization that can limit the lifetime of the atoms in the circular FORT.

4.3.3 Diagnostics and Loading

The number and lifetime of atoms in the FORT are characterized using the following timing sequence. The MOT is allowed to fill for some time τ_f before the atoms are transferred from the MOT into the FORT. They are then stored in the FORT in the absence of any other light sources or the quadrupole magnetic field for some time τ_S. To detect the atoms, the FORT is turned off and the MOT quadrupole magnetic field remains off while the MOT cooling and repump lasers are turned on again, tuned closer to resonance (-$\gamma/2$). The number of atoms N is then inferred from the measured fluorescence [74] and plotted as a function of τ_S (Fig. 4.6). The decay in N is governed by the differential equation

$$\dot{N} = -\Gamma N - \beta' N^2, \tag{4.3}$$

where Γ describes exponential loss processes involving a single trapped atom and β' characterizes the density-dependent losses. The prime on β' is used to refer to atom number loss, instead of density loss. The data are fit to the solution [75]

$$N = N_0\, e^{-\Gamma t}/[1 + (\frac{\beta' N_0}{\Gamma})(1 - e^{-\Gamma t})], \tag{4.4}$$

as shown in Fig. 4.6. From this fit, the initial number N_0, Γ, and β' are extracted.

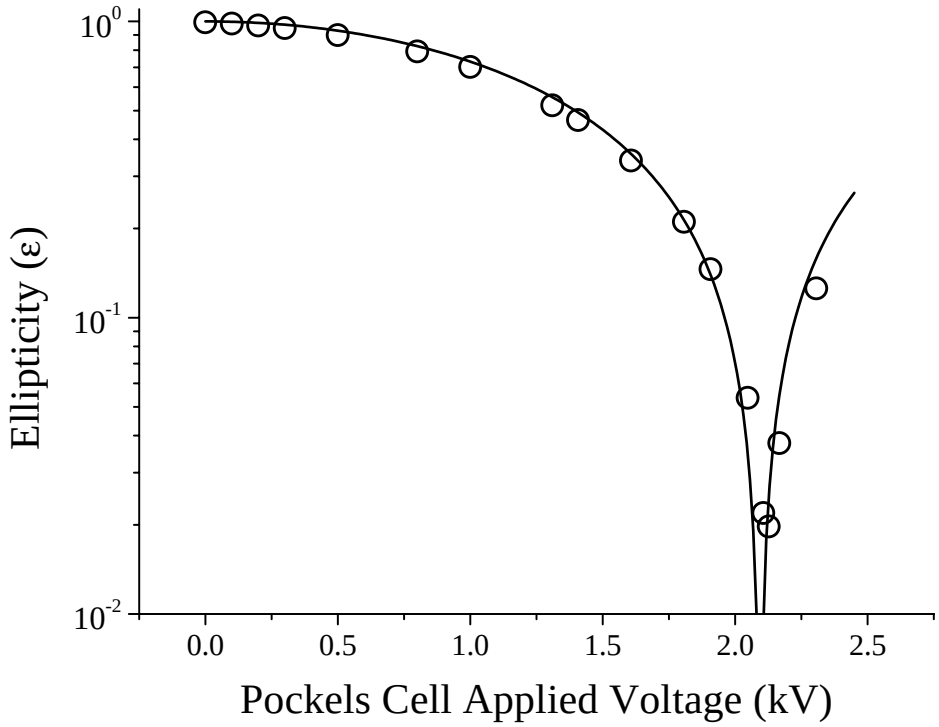

Figure 4.5: Characterization of FORT laser beam polarization after Pockels cell and periscope, as a function of the voltage applied to the Pockels cell. Ellipticity is described in Section 4.2. The black line represents a fit to $\epsilon = |\cos^2(\pi/4(V/V_R) - \sin^2(\pi/4(V/V_R)|$, where V_R is the desired reference voltage that provides perfectly circular light after the periscope.

The physics involved in the transfer of atoms from the MOT to the FORT is quite complicated and will be discussed elsewhere (See Ref. [44] and Chapter 5). Here, we give a summary of results. For the parameters in Fig. 4.6, simple "geometrical loading," in which the FORT laser is turned on immediately after the MOT turns off, traps about 2 $\times 10^5$ atoms. N_0 can be increased by leaving the MOT on with different detuning and power parameters while the FORT is loading. This increase indicates that the MOT lasers cool atoms as they fall into the FORT. For the same FORT parameters, the best loading is typically achieved by detuning the cooling laser to -5 γ and reducing the intensity of the hyperfine pump to 10 μW/cm^2 for 70 ms before the MOT lasers and magnetic fields are switched off. This procedure transfers up to 20% of the MOT atoms into the FORT.

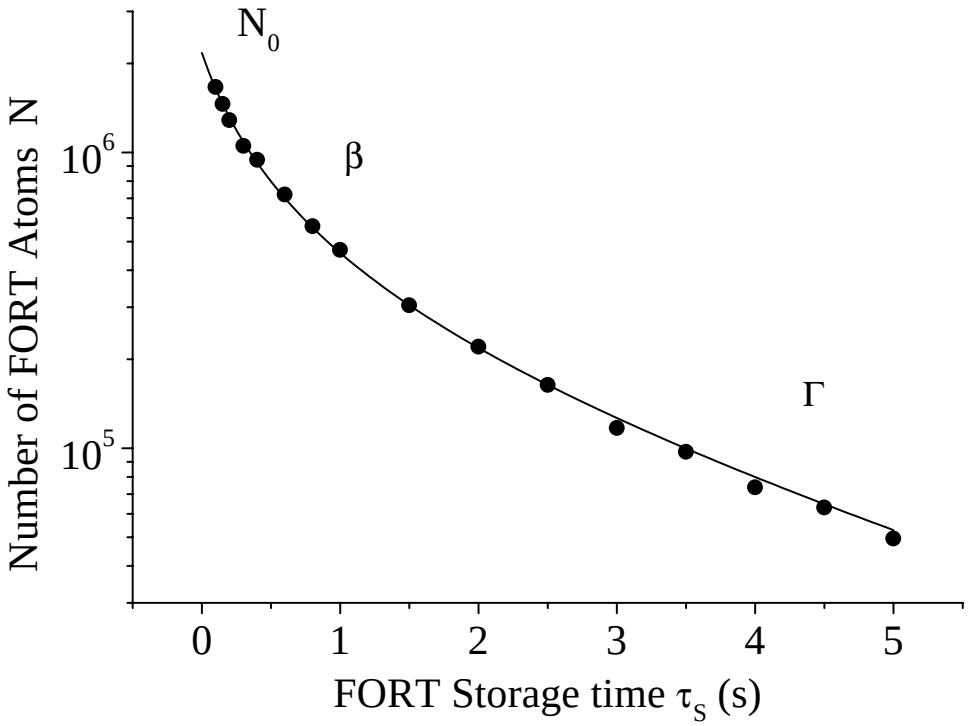

Figure 4.6: Number of atoms stored in a linearly polarized FORT (U_0 = -1.8 mK at 540 mW) as a function of trapping time, after filling the MOT for $\tau_f = 1$ s. No data is taken for the first 100 ms while the MOT atoms fall away. The solid line is a fit to Eq. (4.4), giving N_0 = 2.2$\times 10^6$ atoms, β' = 1.3$\times 10^{-6}$ (atoms s)$^{-1}$, and 1/Γ = 3.0 s. For τ_f= 4 s, 4×10^6 atoms are initially trapped in the linear FORT.

4.4 The Elliptically and Circularly Polarized FORTs

4.4.1 Loading Atoms into the Circular FORT

Optimum loading into an elliptically polarized FORT ($\epsilon < 1$) is different from simply loading into the linear FORT. While geometrical loading still gives similar numbers, only about half as many atoms can be loaded using MOT cooling. The most efficient way to transfer atoms into an elliptical FORT is to first load the linear FORT, and then use the Pockels cell to quickly change the polarization from linear to the desired polarization. This procedure transfers about 70% of the atoms originally held in the linear FORT, regardless of the time constant that governs the change in polarization (from 0.2 to 20 ms). Up to 100% of the atoms in the linear FORT are transferred to the circularly polarized FORT ("circular FORT") by a "transfer" laser beam, circularly polarized and aligned anti-parallel to the FORT laser. This beam, tuned to the 5 ^{2}S$_{1/2}$ $F = 2 \rightarrow 5\ ^2$P$_{3/2}$ F' transition, is applied for 20 ms after the FORT polarization changes to circular. When σ_+-polarized, this transfer beam assists the FORT in optically pumping the atoms into positive m_F levels, and tends to keep them in the F=3

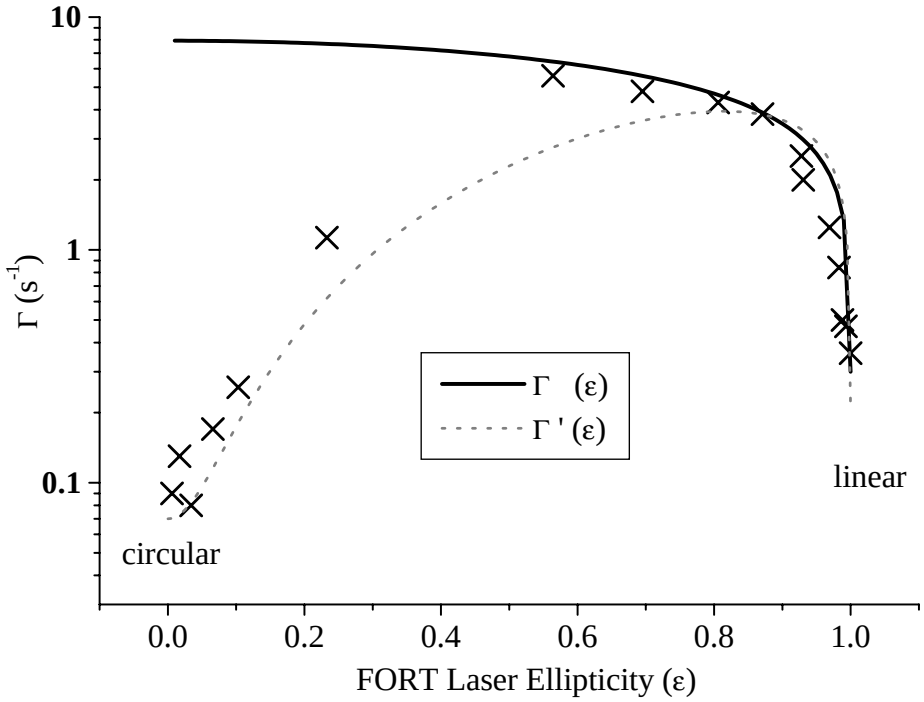

Figure 4.7: Dependence of the FORT exponential loss rate Γ on the ellipticity ϵ of the FORT laser polarization. Crosses indicate the measured loss rate, which is small for purely linear $(\epsilon = 1)$ and purely circular $(\epsilon = 0)$ polarizations. Because the circular potentials are deeper as indicated in Fig. 4.2, $\Gamma(\epsilon = 0) < \Gamma(\epsilon = 1)$. P= 280 mW, U_0 $(m_F = 0)$ = -0.77 mK, and U_0 $(m_F = +3,\ \epsilon = 0)$ = -1.5 mK. The solid and dashed curves represent models of the ground-state dipole-force fluctuation heating described by Eq. (4.5), plus a small offset due to collisions with the background vapor.

states. Thus atoms are pumped to the deep $F = 3$, $m_F = +3$ potential whence they are not readily lost. In this fashion, 4×10^6 atoms were loaded into a circular FORT at λ = 782.3 nm with $U_0(m_F = 0) = -2.0$ mK.

4.4.2 Elliptically Polarized FORT Decay Rates

The lifetime τ of the FORT depends dramatically on the polarization of the FORT laser. A measurement of the decay rate $\Gamma = 1/\tau$ as a function of the ellipticity ϵ of the FORT laser polarization is shown in Fig. 4.7. Γ is smallest when the polarization is perfectly linear or perfectly circular. In addition, Fig. 4.8 shows how Γ changes with FORT intensity for each of these polarizations. Above a trap depth of about $U_0 = -0.2$ mK, the decay rate is independent of intensity for both linear and circular light, but increases linearly with FORT intensity for an intermediate elliptical polarization.

The large losses at imperfect polarizations are due to ground-state dipole-force

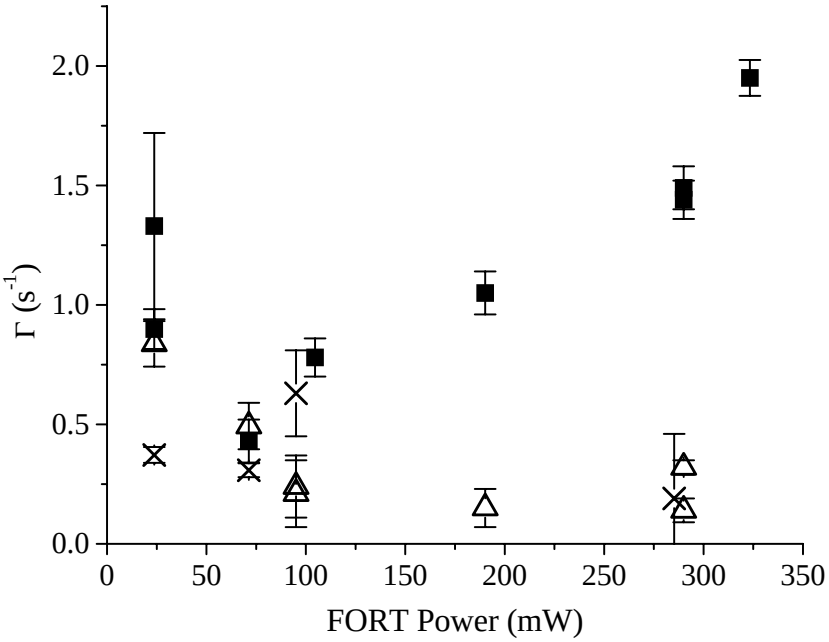

Figure 4.8: Exponential decay rate Γ vs. FORT peak intensity for three different FORT polarizations: linear ($\times$, $\epsilon = 99.995\%$), circular ($\triangle$, $\epsilon = 0.6\%$), and elliptical ($\blacksquare$, $\epsilon = 21\%$). FORT λ = 784.2 nm, $w_0 = 31$ μm, and the maximum U_0 = -0.8 mK for linear polarization at 330 mW.

fluctuation heating that arises when atoms change internal spin state [10]. In the linear FORT, all the ground-state potentials are degenerate, so there is no heating associated with changing the ground level m_F state. However, when the polarization is elliptical, these levels are no longer degenerate, and changes between the levels cause instantaneous changes in the dipole force acting on the atom. These changes result in heating, which evaporates atoms from the trap. The heating rate depends on the rate at which the atoms change state, which in turn depends on the FORT scattering rate. Therefore this heating mechanism increases linearly with intensity. In the circular FORT, however, only $\Delta m_F = +1$ transitions can be excited, and the atoms are all pumped into the $F = 3$, $m_F = +3$ state in about 30 ms. After that, they no longer change their ground state and this heating process turns off.

4.4.3 Model of Lifetime vs. Ellipticity

Agreement between the data and a simple model supports this picture. The dependence of heating on FORT polarization can be modeled with a two-level system using the two trapping potentials of the 5 ^{2}S$_{1/2}$ $F = 3$, $m_F = +3$ and $F = 2$, $m_F = +2$

states, labeled $|a>$ and $|b>$. These states are selected because the U_0 for each is very different, and yet they are closely coupled via off-resonant excitation by the FORT beam. We approximate the potentials as harmonic. Atoms initially held in $|a>$ spread out when they are transferred to $|b>$, which has a smaller spring constant, and then heated when they re-enter $|a>$ with a larger spatial extent and therefore more potential energy. Assuming the atoms hop between the two potentials at a constant rate $\Gamma_{\rm h}$, we derive the exponential time constant as a function of FORT ellipticity:

$$\Gamma(\epsilon) = \Gamma_{\rm h} \ln\frac{U_a(\epsilon)}{U_b(\epsilon)} / \ln\frac{T_f}{T_i}, \tag{4.5}$$

where $U_a(\epsilon)$ and $U_b(\epsilon)$ are calculated for states $|a>$ and $|b>$ using Eq. (4.1), and T_i and T_f are the initial and final temperatures, chosen to be 100 μK and U_0/k_B, respectively. As shown by the solid curve in Fig. 4.7, Eq. (4.5) explains the rapid decrease in Γ as ellipticity approaches linear, but does not fit well near circular.

The decrease in Γ near circular polarization arises from a dependence of the hopping rate on FORT ellipticity. Because the system actually contains many hyperfine and spin states, it is difficult to model exactly. A simplified approach assumes that absorption of a σ_- photon causes transfer from $|a>$ to $|b>$ and absorption of a σ_+ photon transfers atoms back to $|a>$. This gives a new rate of hopping between potentials $\Gamma'_{\rm h} = \epsilon^2\,\Gamma_{\rm h}$ and modifies the expression for the exponential heating rate in the trap to be $\Gamma'(\epsilon) = \epsilon^2\,\Gamma(\epsilon)$. Figure 4.7 shows fits to both $\Gamma(\epsilon)$ and $\Gamma'(\epsilon)$, with $\Gamma_{\rm h}$ the only free parameter in each case. They yield $\Gamma_{\rm h}$ = 13/s and $\Gamma_{\rm h}$=17/s, respectively. To calculate an optical scattering rate from these values, we simply divide by the product of the appropriate Clebsch-Gordon coefficients (0.05) for the four-photon heating process (absorption, emission to $F = 2$, absorption, emission to $F = 3$). The resulting scattering rates (260/s and 340/s) agree well with the estimated average scattering rate in the FORT to within its 50% uncertainty.

4.4.4 FORT $\lambda > \lambda_{D_1}$

The decay of atoms from the FORT behaves very differently depending on the wavelength of the FORT laser light. All the data preceding and following this section were taken with the FORT wavelength smaller that 795 nm. In these cases, the circular FORT decay curves fit well to Eq. (4.4). In contrast, when the circular FORT wavelength is red of both the D_1 and D_2 transition, Fig. 4.9 shows that the decay of atoms occurs over two very different exponential time scales. In Fig. 4.9, (■) are fit to

$$N = A_1 e^{-t/\tau_1} + A_2 e^{-t/\tau_2} \tag{4.6}$$

yielding τ_1 = 65 ± 8 ms and τ_2 = 3.2 ± 0.2 s. Time constant τ_2 comes from the same background collisional loss rate observed in the decay of atoms from the CFORT tuned between the D_1 and D_2 lines, and in the linear FORT. However, the new, faster decay rate τ_1 is due to optical pumping and evaporative loss of atoms by the circular FORT.

Optical pumping of atoms in the circular FORT only causes additional losses when the FORT is tuned red of the D_1 transition. In this case, the sign of the second

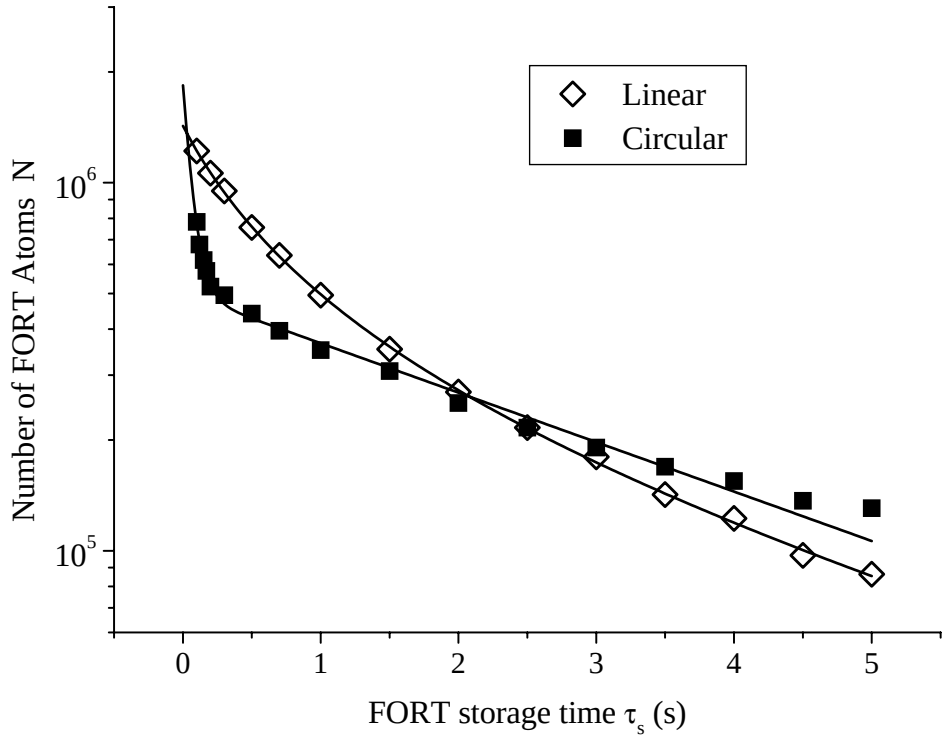

Figure 4.9: FORT decay curve with FORT $\lambda = 798.4$ nm, P = 290 mW, and w_0 = 31 μm for both linear ($\Diamond$, $U_0 = -0.7$ mK) and circular [■, $U_0(m_F = +3) = -0.3$ mK] polarizations. Solid lines represent fits to Eq. (4.4) and Eq. (4.6) respectively.

term of Eq. (4.1) is such that the circular FORT tends to optically pump atoms into the shallowest potential. Measurements described in the next chapter (Section 5.5) indicate that the FORT holds the temperature of the atoms at $T = 0.4 \times U_0/k_B$. Therefore, atoms initially held in the linear FORT have temperatures too large to be confined in the shallower potentials of the circular FORT once they are pumped into them. Atoms initially in the $m_F = 3$ state evaporatively cool until they can be held by the shallow potential. In addition, atoms in the deeper states are optically pumped into the shallowest state, and also evaporatively cool. Once all the atoms are optically pumped and have evaporated to a reasonable temperature, this source of loss ceases to contribute to the decay in the number of atoms.

Brief attempts to minimize the losses due to optical pumping were unsuccessful. These included varying the time over which the polarization was switched, and using the circularly-polarized "transfer beam" to optically pump the atoms before the potential is switched. Neither of these can eliminate the essential problem: atoms originally held in the linear FORT have too much kinetic energy to be retained by the shallower $F = 3$, $m_F = 3$, regardless of how they make the transition. One technique that may work well is to reduce the linear FORT power to some fraction f of maximum at the beginning of the cycle, where f is the ratio between $U_0(m_F = 3)$ and $U_0(m_F = 0)$;

$f = 2$ at FORT λ = 800.0 nm. Then one should apply the transfer beam to optically pump most of the atoms into the $F = 3$, $m_F = 3$ state, and then simultaneously restore the FORT power to its maximum value and turn on the Pockels cell. In this way, the depth of the well containing the atoms would not change, and evaporative losses could be eliminated.

4.5 Spin-Polarization Demonstration

The inherent spin-polarizing nature of the circular FORT is confirmed by measuring the fraction of atoms that populate the $F = 3$, $m_F = +3$ state. Exciting the atoms in the $F = 3$ state with an additional laser causes loss by pumping them to the weakly trapped $F = 2$ state. We compare the loss when all m_F states are excited to the loss when all but $m_F = +3$ is excited. The probe laser beam (Figs. 4.1 and 4.4) is linearly polarized and tuned to excite $^2\mathrm{S}_{1/2}\, F = 3 \rightarrow {}^2\mathrm{P}_{3/2}\, F'$ transitions. When this beam is aligned as shown in Fig. 4.4, it induces either $\Delta m = 0$ or $\Delta m = \pm 1$ transitions, depending on whether the polarization is oriented horizontally or vertically. The probe beam is pulsed on for 20 ms at an intensity of 1 μW/cm^2, 45 ms after the MOT is switched off. We then measure the resulting decrease in the number of atoms in the circular FORT. This signal is plotted as a function of frequency in Fig. 4.10 for both polarizations. When the laser is tuned to the $F = 3 \rightarrow F' = 2$ transition and the polarization is vertical (•), we find that the loss saturates at 33%. However, when the polarization is horizontal ($\diamond$), unsaturated loss is only 4%. The difference in fractional loss indicates a large population in the $m_F = +3$ state, because horizontal polarization does not excite atoms in this state, while vertical excites all spin states. After including a factor of 2 for saturation, the ratio of the two losses implies that 7% of the atoms are not in the $F = 3$, m_F = +3 stretched state. Because these atoms are most likely to be in the m_F = +2 state, the spin-polarization is 98(1)%.

4.6 Conclusion

We have demonstrated and characterized a circularly polarized FORT. We have also shown that the trap provides a high degree of spin-polarization. The splittings of m_F levels in the circular FORT should allow RF cooling techniques in the trap similar to methods employed in magnetic traps. Finally, we have shown that small polarization imperfections in circular or linear FORTs can lead to heating and subsequent loss due to ground-state dipole-force fluctuations.

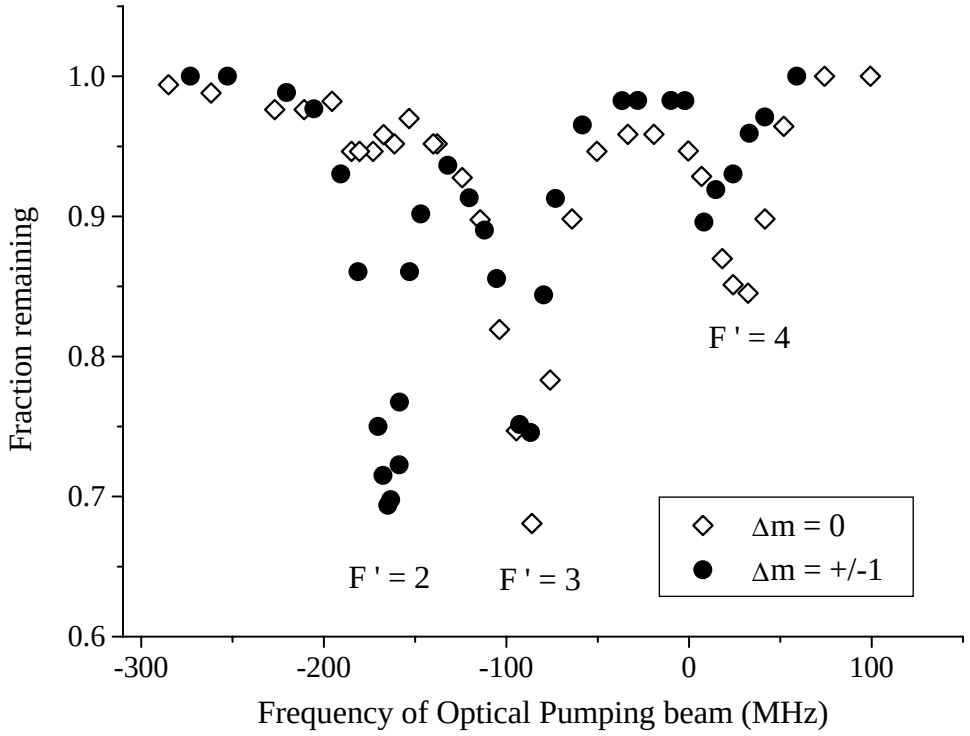

Figure 4.10: Fraction of atoms remaining in the FORT as a function of the frequency of an applied optical pumping beam for two different polarizations: ($\diamond$ and $\bullet$). Frequency is measured with respect to the frequency of the unshifted 5 ^{2}S$_{1/2}$ F=3 $\rightarrow$ 5 ^{2}P$_{3/2}$ F' = 4 transition. Signals are normalized to the number of atoms held in the trap without the optical pumping beam (8×10^5 atoms). Resonances are AC Stark-shifted about 30 MHz with respect to the resonances in free atoms, and separations are consistent with the 5 ^{2}P$_{3/2}$ hyperfine splitting. The difference between $\diamond$ and $\bullet$ for $F' = 2$ is clear evidence for spin-polarization. This shallow trap [P=190 mW, $U_0(m_F = 0)$ = -0.63 mK, and $U_0(m_F = 3)$ = -1.2 mK] allows resolution of the hyperfine structure. In deeper traps, the spin-polarization should only improve.

Chapter 5

The Physics of Loading an Optical Dipole Trap

5.1 Introduction

In the last decade, many different schemes for preparing and trapping ultra cold and dense samples of atoms have been demonstrated. Of these, the optical dipole trap [38] requires no magnetic fields and relatively few optical excitations to provide a conservative and tightly confining trapping potential. These characteristics make it an appealing option for various metrology applications such as parity nonconservation and β-decay asymmetry measurements. It may also be an option for reaching BEC in a purely optical trap. For these applications, large samples of atoms must be transfered into the dipole trap. This is almost always done from a magneto-optical trap (MOT) [14]. However, the processes determining the transfer between the MOT and the optical dipole trap are poorly understood. Here we give a detailed description and explanation of the loading process and suggest ways in which to improve the loading.

The simplest optical dipole trap consists of a focused single Gaussian laser beam. Typically the light is detuned below the atomic resonance, from a few tenths of a nm to several tens of nm. The latter are called far off resonance traps (FORT) [39]. We will use the abbreviation FORT in discussing optical dipole traps. Conceptually a FORT works as follows: the AC Stark shift induced by the trapping light lowers the ground state energy of the atoms proportionally to the local intensity. The spatial dependence of the light intensity is therefore equivalent to a spatial dependence of the atomic potential energy. The atom has the lowest energy in the focus of the trapping beam and can therefore be trapped there. For very large detuning, typically several nm, the photon scattering rate becomes so low that the potential is truly conservative.

The first FORTs were running-wave Gaussian laser beams focused to a waist of about $10\,\mu\mathrm{m}$ [38, 39]. By alternating the FORT with an optical molasses that cooled atoms into the trap [38, 39], about 500 to 1300 atoms were loaded. In later work [69, 76, 77], the FORT was loaded by overlapping it with a MOT continuously, which improved the number of atoms that was transfered to 10^6.

A key step in the loading of a FORT from a MOT is a strong reduction of the hyperfine repump in the last 10-30 ms of the overlap between the traps. It has been conjectured [76] that this reduction helps because it reduces three density limiting processes, namely, radiative repulsion forces, photo-associative collisions, and ground state hyperfine changing collisions. However, to our knowledge, there has not yet been an ex-

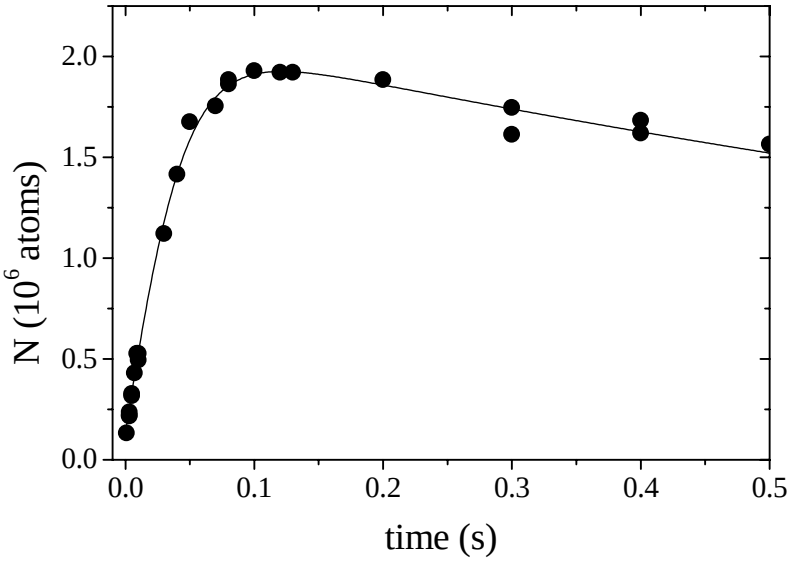

Figure 5.1: Number of atoms N in the FORT as a function of time spent loading, for a trap depth of -1 mK and a waist of $26\ \mu\mathrm{m}$.

tensive study of the loading process. Therefore, in this paper we present a detailed and comprehensive investigation of the many mechanisms that govern the loading process.

We find that loading a FORT from a MOT is an interesting dynamical process rich in physics. As illustrated in Fig. 5.1, the number of atoms in the FORT first increases rapidly and nearly linearly in time until loss mechanisms set a limit to the maximum number. The loading rate and loss processes both depend in complex ways on the laser fields involved. One factor that determines the loading rate is the flux of atoms into the trapping volume. This flux depends on the MOT density and temperature, i.e., average velocity of the atoms in the MOT. For the atoms to be trapped in the FORT, cooling mechanisms must also be active in the region where the MOT and FORT overlap Both the flux and the probability for trapping depend on the trap depth and light-shifts inherent to the FORT.

Losses from the trap can be caused by heating mechanisms and collisional processes. Contributions to heating arise from spontaneously scattered FORT light photons, background gas collisions [16, 17], intensity fluctuations, and the pointing stability of the FORT beam [71]. However, for large numbers of atoms the losses are dominated by collisional processes [78], including photo-association, spin exchange/ground state hyperfine changing collisions, and radiative escape. Photo-associative collisions can be induced by the FORT light itself and lead to untrapped molecules. During a ground state hyperfine changing collision, a pair of atoms gains as much as the hyperfine energy splitting in kinetic energy (0.14 K for $^{85}\mathrm{Rb}$), which is enough to eject it out of the FORT. In radiative escape, an atom is optically excited and reemits during

a collision, and the attractive dipole-induced interaction between the excited and non-excited atom leads to an increase of kinetic energy which is enough to eject an atom from the trap.

The loading and loss rates depend on the shape and depth of the optical potential, as well as the intensity and detuning of the MOT light fields. By studying the loading rate and loss rate separately as a function of these parameters, we have obtained a detailed understanding of the FORT loading process. This understanding has allowed us to optimize parameters in order to improve our loading efficiency to high values (47% of the MOT atoms were loaded into the FORT). Although we studied the loading of $^{85}\mathrm{Rb}$ into a dipole trap with a detuning of a few nm, the physical processes and optimization should be generally applicable to other alkali species and FORTs, when the FORT trap depth exceeds the MOT atom temperature. In the opposite regime, O'Hara et al. [79] have shown that a static equilibration model applies in CO_2 laser traps.

This Chapter is organized as follows. In Sec. 5.2 a more detailed expression for the depth and shape of the FORT potential is given. In Sec. 5.3 our experimental setup is discussed, including the loading of the FORT and the diagnostic tools for measuring the number of atoms and size of the trapped sample. In Sec. 5.4 we present measurements of the loading rate and loss rate as a function of different MOT and FORT parameters. In Sec. 5.5 the temperature of the atoms in the FORT is given. In Sec. 5.6 the loss rates of the FORT in the absence of MOT light are discussed. In Sec. 5.7 we present a physical model of the loading process which explains the data presented in Sec. 5.4. In Sec. 5.8 we discuss how our model explains the interdependencies of the MOT and FORT parameters. In Sec. 5.9 we demonstrate how, based on our understanding of the FORT loading process, the number of trapped atoms can be improved using a shadowed repump beam. Finally, Sec. 5.10 contains summarizing remarks and discusses the general applicability of these results to other traps.

5.2 The FORT potential

The trapping potential formed by the focused laser beam has been described in detail in Section 4.2. The most general form for the spatial dependence of U is given by

$$U(r,z) = U_0 \frac{\exp[-2r^2/w(z)^2]}{1+(z/z_R)^2}\,, \tag{5.1}$$

with z the longitudinal coordinate and r the radial coordinate (denoted ρ in previous chapter). Then the beam radius $w(z)$ is given as a function of longitudinal position, $w(z) = w_0\sqrt{1+(z/z_R)^2}$ where z_R is the beam Rayleigh range [72]. Equation (4.1) gives U_0 as a function of many parameters, including the laser beam polarization ellipticity ϵ.

This chapter focuses primarily on the loading of a FORT made with linearly polarized trapping light. This is because loading the linear FORT is the most efficient process, and therefore usually a first step toward loading the circular FORT. We justify this approach in Sec. 5.4.6, where we discuss how the loading of the FORT is affected

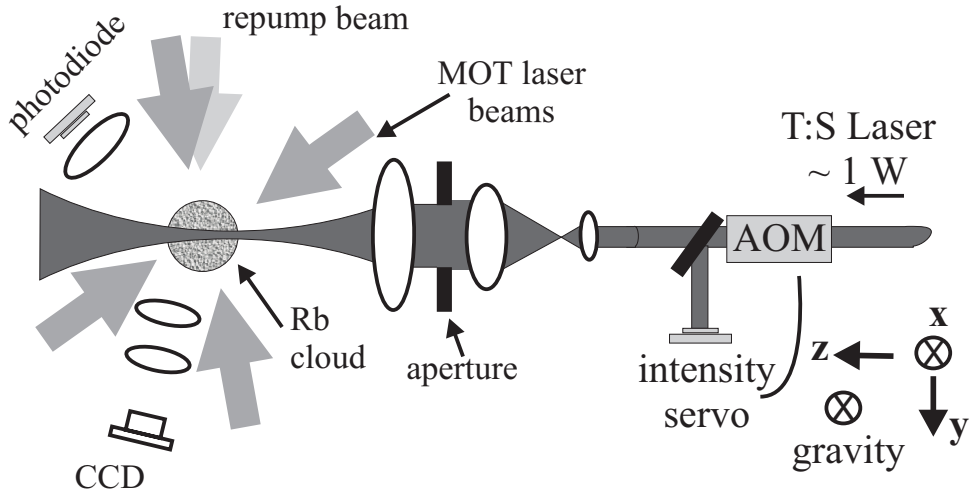

Figure 5.2: Experimental setup

when optical Zeeman splittings are present due to elliptical polarization of the FORT light.

5.3 Experiment

The experimental setup is very similar to that described in the previous chapter, and shown schematically in Fig. 5.2. The starting point of all the experiments described here is a MOT, which collects $^{85}\mathrm{Rb}$ atoms from a 5×10^{-10} Torr vapor, and contains a maximum of about 3×10^8 atoms in steady state with a filling time constant of $\approx 12\,\mathrm{s}$. Two extended-cavity diode lasers, both stabilized to atomic lines in $^{85}\mathrm{Rb}$ at 780 nm with a dichroic atomic vapor laser lock (DAVLL) are used for the MOT (see [70] and Appendix A). One laser provides 6 mW for trapping and cooling (divided between three retro-reflected beams) and is tuned red of the $5\,^2S_{1/2}\,F = 3 \rightarrow 5\,^2P_{3/2}\,F' = 4$ transition by an amount denoted as Δ_{M}. We refer to this light as the "primary" MOT light (previously called the "cooling" laser), and denote its total six beam intensity by I_{M}. The beams have a Gaussian beam radius of $9.3\ \mathrm{mm}$. The other MOT laser is used for hyperfine repumping and is tuned near the $5\,^2S_{1/2}\,F = 2 \rightarrow 5\,^2P_{3/2}\,F' = 3$ transition. We refer to this light as the "repump" light, and denote its detuning as Δ_{R} ($\Delta_{\mathrm{R}} = 0$ unless otherwise indicated). We use one single retro-reflected beam of intensity $I_{\mathrm{R}} = 3\,\mathrm{mW/cm^2}$ for repumping the MOT. Both laser beams have acoustooptic modulators (AOM) in them for temporal control of the light intensity. The magnetic field gradient of the quadrupole field along the strong axis is 5 Gauss/cm, and can be switched off within 3 ms.

The FORT light is generated with a home-built Titanium:Sapphire laser, with a nominal output power of 1.2 W. After passing through an AOM, the first order is intensity stabilized, collimated, and expanded. The beam is focused into the vacuum chamber with a $20\ \mathrm{cm}$ focal length doublet lens to a focus of radius $w_0 = 26\ \mu\mathrm{m}$

($1/e^2$ intensity), unless stated otherwise. The detuning from the D_2 line is typically $2\,\mathrm{to}\,4$ nm to the red. For $P = 300\,\mathrm{mW}$, $w_0 = 26\mu\mathrm{m}$, and $\lambda = 784\,\mathrm{nm}$ the well depth $U_0/k_\mathrm{B} = -1.4\,\mathrm{mK}$. Approximating the center region of the FORT potential as harmonic, the trap oscillation frequencies are $4.6\mathrm{kHz}$ and $34\mathrm{Hz}$ in the transverse and longitudinal direction, respectively. Note that the trap as a whole is highly anharmonic at the edges. The peak photon scattering rate (Γ_sc) for these parameters is $1.3\,\mathrm{kHz}$, as calculated from the well known expression

$$\Gamma_\mathrm{sc} = \frac{1}{2\tau_0}\frac{1}{1+\frac{I_S}{I}(1+\frac{4\Delta^2}{\gamma^2})} \tag{5.2}$$

where the natural lifetime $\tau_0 \approx 30$ ns, the saturation intensity $I_S \approx 1.6$ mW/cm^2, the laser detuning is given by Δ, and the full width half maximum of the natural linewidth $\gamma \approx 6$ MHz.

5.3.1 Loading and diagnostics

The sequence for loading the FORT from the MOT and measuring the number of atoms is as follows. The MOT fills for typically 3 s at an optimum detuning of $\Delta_\mathrm{M} = -2\,\gamma$, and at maximum repump intensity. This results in typically 3×10^7 atoms in the MOT. We then switch on the FORT while simultaneously increasing the detuning of the primary MOT light and reducing the repump light intensity. We will refer to this stage in the timing cycle as the "FORT loading stage," which is typically $20 - 200$ ms long, depending on FORT parameters. The primary MOT light, MOT repump light and magnetic fields are switched off, and the atoms are held in the FORT for a variable length of time, but at least 100 ms before the detection light comes on, so that the MOT cloud can fall out of the detection region. The atoms are then released from the FORT and detected by turning on the MOT light (primary and repump) but no magnetic field, the primary MOT light frequency now closer to resonance $\Delta_\mathrm{M} = -\gamma/2$. The number of atoms N is determined from the amount of fluorescence [74] collected with a low noise photo-diode. Under some circumstances the cloud of atoms trapped in the FORT is so large that it extends beyond the field of view of our photo detector. In this case the number is measured by recapturing them into a MOT. For this case the detection must be delayed for at least 250 ms to give the MOT cloud time to fall out of the MOT beams, thus making sure that we are detecting FORT atoms and not MOT atoms.

The number of atoms in the FORT is measured as a function of storage time, as in the previous chapter. We call this a lifetime curve. A typical example of a lifetime curve is shown in Fig. 5.3. Note that the number of atoms does not have a simple exponential dependence on time. We find that the loss of atoms is well described by Eq. (4.3) and its solution [Eq.(4.4)], as was the circular FORT. We use the analytical solution of Eq. (4.3) as a fit function to the data to find the number N_0 initially trapped, as well as values of Γ and β' (see Sec. 5.6). The prime on β' is used to refer to atom number loss instead of density loss.

Absorption imaging is used to measure the size and temperature of the MOT cloud as well as the cloud of atoms in the FORT. The imaging system consists of a two

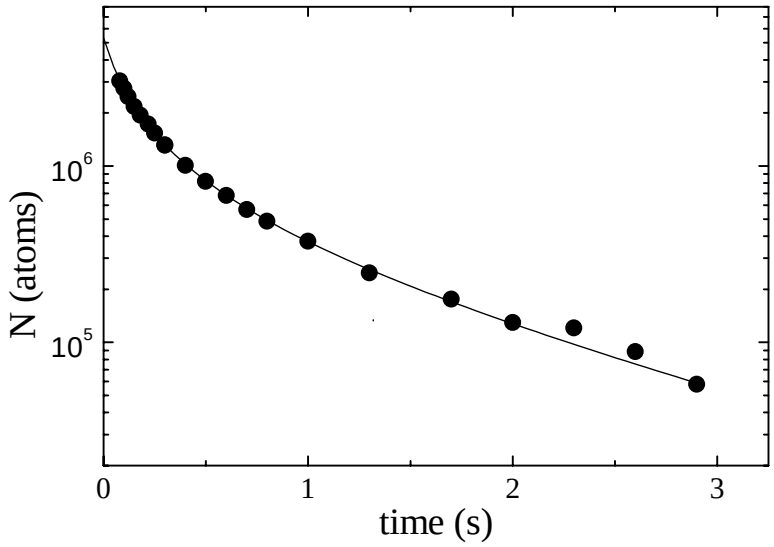

Figure 5.3: Number of atoms remaining in the FORT as a function of time, for trap parameters $w_0 = 26\mu\mathrm{m}$, $P = 290\,\mathrm{mW}$, $\lambda = 782.5\,\mathrm{nm}$. The trap depth is $U_0/k_\mathrm{B} = -2.3\,\mathrm{mK}$. The solid curve is a fit of Eq. (4.3) to the data.

lens telescope making a one to one image onto a CCD array. The lenses are 18 cm focal length cemented doublets. The line of view is perpendicular to the FORT beam. This allows us to observe the transverse as well as longitudinal shape of the cloud of atoms trapped in the FORT.

5.4 Dynamics of the loading process

In Fig. 5.1 we showed that the transfer of atoms from the MOT to the FORT is a dynamical process, in which the number of atoms loaded into the FORT increases rapidly until a competing process causes the number to reach a maximum and then decrease at later times. Here we investigate the precise shape of the loading curve in more detail. The number of atoms in the FORT for longer loading times is shown in Fig. 5.4.

The shape of the loading curve is explained as follows. Initially, the number of atoms in the FORT increases as $N(t) = R_0 t$. But at larger times the number starts to roll over. This occurs for two reasons. First, the MOT loses atoms due to the reduced repump intensity and different detuning of the primary MOT light. This reduces the loading rate. Second, the trap loss rates become large enough to counteract the loading.

In a similar fashion as Eq. (4.3) we find that the shape of the FORT loading curve

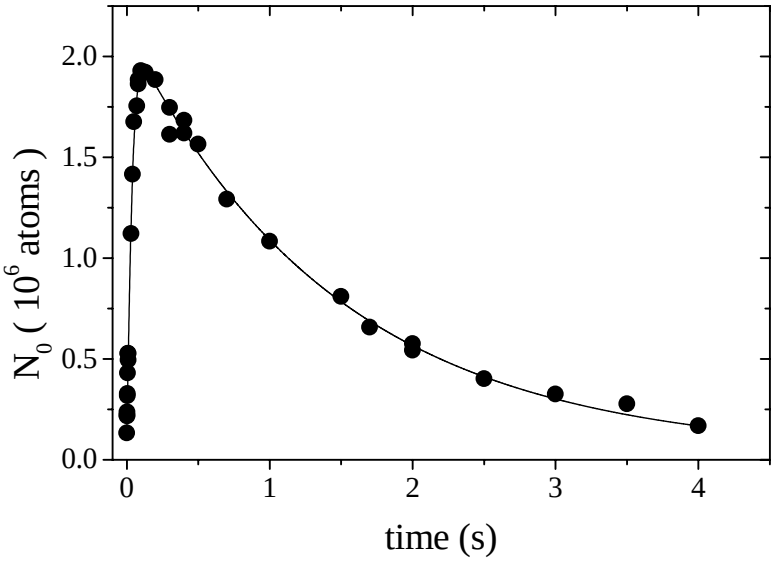

Figure 5.4: Number of atoms loaded in the FORT as a function of FORT loading stage duration, for trap parameters $w_0 = 26\,\mu\mathrm{m}$, $P = 305\mathrm{mW}$, and $\lambda = 784.5\,\mathrm{nm}$. Primary MOT intensity $I_\mathrm{M} = 8.2\,\mathrm{mW/cm^2}$ and MOT repump intensity $I_\mathrm{R} = 4.7\,\mu\mathrm{W/cm^2}$. The solid curve is a fit of Eq. (5.3) to the data. The loss coefficient $\beta'_\mathrm{L} = (1.56 \pm 0.22) \times 10^{-5}(\mathrm{atoms\,s})^{-1}$, see text.

is well described by

$$\frac{dN}{dt} = R_0 \exp(-\gamma_\mathrm{MOT} t) - \Gamma_\mathrm{L} N - \beta'_\mathrm{L} N^2\,, \tag{5.3}$$

where γ_MOT is the rate at which the MOT loses atoms due to the change of MOT light detuning and repump intensity. And Γ_L and β'_L characterize density-independent and density-dependent losses. The subscript L expresses the fact that the loss rates during loading are generally different from those during storage in the FORT without any MOT light present.

Four parameters determine the loading: R_0, γ_MOT, Γ_L, and β'_L. To understand the physics of the loading process we must therefore determine these four parameters under a variety of conditions. The initial loading rate, R_0, can be determined directly from the initial slope of the loading curve. Then γ_MOT can be determined by measuring the rate at which the MOT fluorescence decreases during the FORT loading stage. We confirmed this explicitly by allowing the MOT to dissipate for a variable length of time, τ_d, before the start of the FORT loading stage. The initial slope of the loading curve $R(\tau_d)$ was observed to be $R(\tau_d) = R_0\ \exp(-\gamma_\mathrm{MOT}\tau_d)$, consistent with the MOT fluorescence measurement. The rate constants β'_L and Γ_L can then be determined by fitting the numerical solution of Eq. (5.3) to the data. The solid curve in Fig. 5.4 is

such a fit, indicating how well the loading process is described by Eq. (5.3). With R_0 and $\gamma_{\rm MOT}$ constrained to the directly measured values, as mentioned above, the extracted values of $\beta'_{\rm L}$ and $\gamma_{\rm L}$ show that the $-\beta'_{\rm L}N^2$ loss term clearly dominates over the $-\gamma_{\rm L}N$ term. This is most apparent in the slope of the tail of the load curve. Thus collisional processes dominate the losses from the FORT during its loading.

The losses during the loading of the FORT can be studied independent of the loading rate. This is done as follows. The FORT is first loaded under optimum conditions and the atoms stored for 100 ms, after which the MOT lasers are switched back on, but there is no magnetic field, for the remainder of the FORT storage time. We refer to such a measurement as a loss curve measurement. In this way we can study the effect of the MOT light field parameters on the loss rate, i.e., we eliminated the loading term in Eq. (5.3). With the MOT lasers on, the loss rate is much larger than in the absence of any MOT light and completely dominated by density dependent losses $\beta'_{\rm L}$. The result of such a measurement is shown in Fig. 5.5 (▲), which also contains the lifetime curve (•) recorded in the absence of MOT light. Comparing corresponding loading and loss curves we find the same values of $\beta'_{\rm L}$ from the different types of data sets to within a 30% spread. The advantage of measuring a loss curve is that we can independently change all the MOT light field parameters without altering the number of atoms initially loaded into the FORT.

The nice agreement between the value of $\beta'_{\rm L}$ determined from the loading curve in Fig. 5.4 and the loss curve in Fig. 5.5, taken for identical MOT and FORT parameters, gives good confidence that Eq. (5.3) gives a good description of the physics involved in loading the FORT.

The fact that collisional losses, $\beta'_{\rm L}$, dominate the tail of the loading curve can also be seen in another way. If one neglects the $-\Gamma_{\rm L}\,N$ term in Eq. (5.3) and sets the loading rate to be constant at R_0, i.e. assuming that the MOT does not lose atoms during the loading of the FORT, the steady state solution of Eq. (5.3) is

$$N_{\rm st} = \sqrt{R_0/\beta'_{\rm L}}\,. \tag{5.4}$$

Substituting the values of R_0 and $\beta'_{\rm L}$ obtained as discussed above, the calculated $N_{\rm st}$ agrees to within 10% with the maxima of the loading curve.

Several consistency checks were performed on the accuracy of fitting Eq. (5.3) to the data. One test was to set all four parameters in Eq. (5.3) free. This reproduced the independently determined values of R_0 and $\gamma_{\rm MOT}$, as well as those of $\Gamma_{\rm L}$ and $\beta'_{\rm L}$, with $\Gamma_{\rm L}$ least well determined. Both $\gamma_{\rm MOT}$ and $\Gamma_{\rm L}$ give rise to exponential decay and are therefore strongly coupled in the least squares fit. We find that most often $\Gamma_{\rm L}$ comes out of the fit as zero, and $\gamma_{\rm MOT}$ to within 20% of the value determined directly from the MOT fluorescence. Assuming that the value of $\Gamma_{\rm L}$ should at least be as big as that of the trap in the absence of the MOT light, we set it to that value and see no significant change in the value of $\beta'_{\rm L}$. Fitting the loading curves with these constraints and different combinations of free parameters, we find a spread in the $\beta'_{\rm L}$ values of up to 30% for a given data set, which is more than adequate for the analysis of the data given below. We are now in the position to investigate the loading of the FORT in terms of R_0 and $\beta'_{\rm L}$ separately, by either measuring load curves or loss curves.

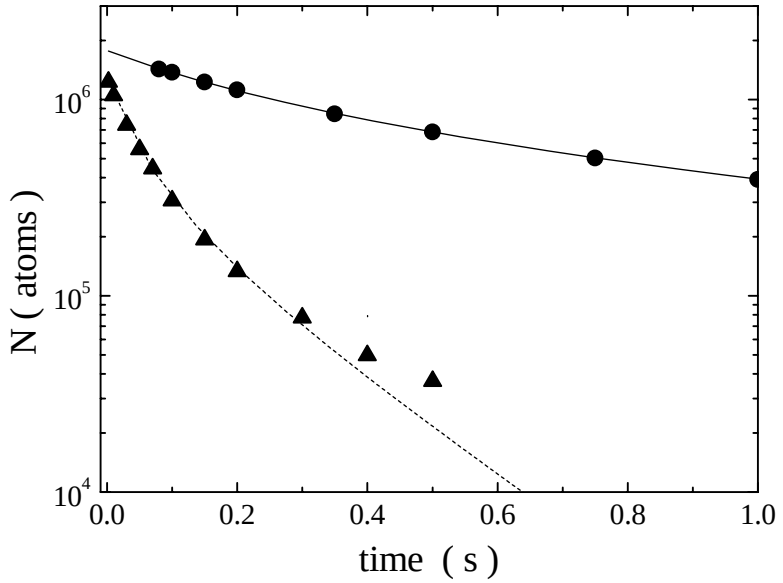

Figure 5.5: Number of atoms in the FORT vs time, without any MOT light (•) and with MOT light on (▲), primary MOT intensity $I_{\rm M} = 8.2\,{\rm mW/cm^2}$, and MOT repump intensity $I_{\rm R} = 4.7\,\mu{\rm W/cm^2}$. For trap parameters $w_0 = 26\,\mu$m, $P = 305{\rm mW}$ and $\lambda = 784.5\,{\rm nm}$. The curves are fits of Eq. (4.3) to the data. The number dependent loss rates are $\beta' = (1.42\pm0.05\times10^{-6}\,({\rm atoms\,s})^{-1}$ and $\beta'_{\rm L} = (1.4\pm0.1)\times10^{-5}\,({\rm atoms\,s})^{-1}$, for the atoms stored in the FORT without any MOT and with MOT light, respectively.

5.4.1 Hyperfine repump intensity and detuning

A commonly used technique to improve the loading of a FORT is to reduce the hyperfine repump intensity. Here we show how the intensity and detuning of the repump light affect the loading rate R_0 as well as the loss rate $\beta'_{\rm L}$. We concentrate first on the dependence of the loading rate and loss rate on the hyperfine repump intensity at resonance ($F = 2 \rightarrow F' = 3$). The data in Fig. 5.6 show that for the maximum $I_{\rm M}$ there is a critical repump intensity below which the MOT is not sustained during the FORT loading stage and the loading rate goes to zero. For $I_{\rm R}$ above that critical value, the loading rate decreases because the density in the MOT decreases due to radiative repulsion. The optimum level is about $I_{\rm R} = 5\,\mu{\rm W/cm^2}$. Note that the loading rate of the FORT is as high as 5×10^7 atoms s^{-1}, which is a factor 2 higher than that of the MOT. The loss rate $\beta'_{\rm L}$ increases rapidly with repump intensity and starts to saturate at high repump intensity. For lower $I_{\rm M}$, saturation sets in at lower repump intensities and $\beta'_{\rm L}$ is smaller.

The optimum repump intensity is intimately linked to the repump detuning. This interdependence is shown in Fig. 5.7, where the maximum number of atoms loaded into the FORT is plotted versus $\Delta_{\rm R}$ for different values of $I_{\rm R}$. Increasing $I_{\rm R}$ from

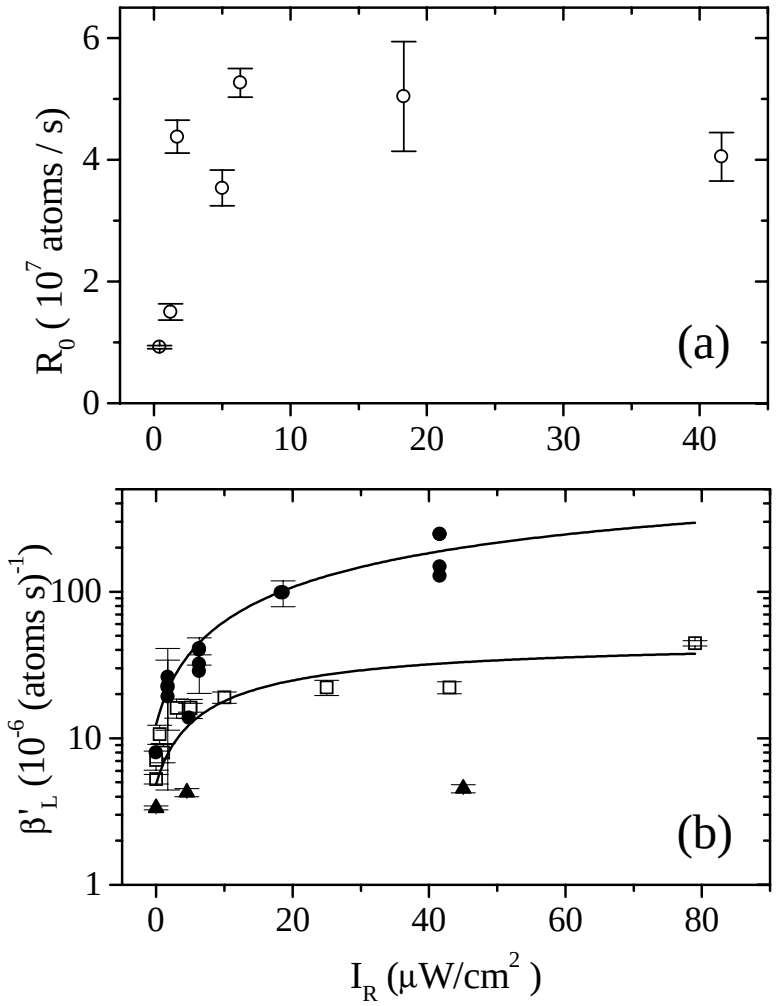

Figure 5.6: FORT loading rate R_0 (a) and loss coefficient $\beta'_{\rm L}$ (b) as a function of hyperfine repump light intensity. For trap parameters $w_0 = 26\,\mu$m, $P = 300$mW and $\lambda = 784.5$nm. The loss rate was measured for $I_{\rm M} = 8\,{\rm mW/cm^2}$ (•), reduced MOT intensity of $I_{\rm M} = 1\,{\rm mW/cm^2}$ (□), and complete absence of primary MOT light (▲). The solid lines are derived from the model described in Sec. 5.7.1. Error bars are statistical and do not reflect systematic uncertainties in $I_{\rm M}$.

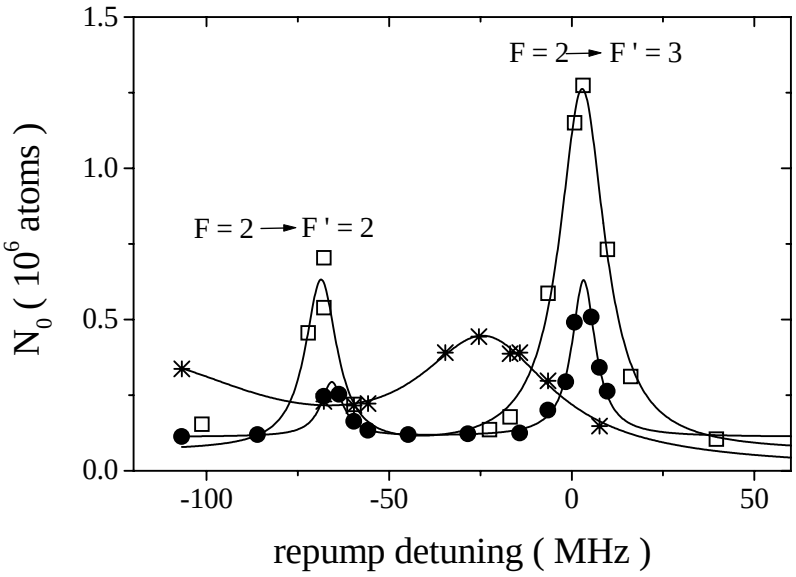

Figure 5.7: Number of atoms in FORT as a function of MOT hyperfine repump detuning for different repump intensities, $1.4\,\mu\mathrm{W/cm^2}$ (•), $4\,\mu\mathrm{W/cm^2}$ (□), and $280\,\mu\mathrm{W/cm^2}$ ($*$). The frequency offset is arbitrary. FORT parameters are $w_0 = 26\,\mu\mathrm{m}$, $P = 200\,\mathrm{mW}$, and $\lambda = 798.1\,\mathrm{nm}$. Solid curves are Lorentzians fitted to the data to guide the eye.

$1.4\,\mu\mathrm{W/cm^2}$ to $4\,\mu\mathrm{W/cm^2}$, we see that the number in the trap increases, but the optimum repump detuning stays on resonance. Increasing the intensity to $280\,\mu\mathrm{W/cm^2}$ causes the optimum repump detuning to shift red. Interestingly, the optimum number of atoms is loaded when the repump scattering rate is the same for both $I_\mathrm{R} = 4\,\mu\mathrm{W/cm^2}$ and $I_\mathrm{R} = 280\,\mu\mathrm{W/cm^2}$ due to the different detuning, indicating that an optimum repump scattering rate exists for loading the FORT. However, the number of atoms drops and the resonance broadens, which shows that the number of atoms in the FORT is not determined by the repump scattering rate alone. This will be explained in more detail in Sec. 5.8.

In summary, the loading rate R_0 is optimal for a very low repump intensity of about $5\,\mu\mathrm{W/cm^2}$ and zero detuning. The loss rate β'_L increases with repump intensity and is larger for higher intensity of the primary MOT light.

5.4.2 Primary MOT light intensity

Both R_0 and β'_L depend on the primary MOT intensity, I_M. The data in Fig. 5.8 show that β'_L rises rapidly and then saturates with increasing I_M. The MOT intensity at which saturation sets in is higher for higher repump intensities. Combined with the dependence of β'_L on repump intensity this suggests that excited state collisions leading

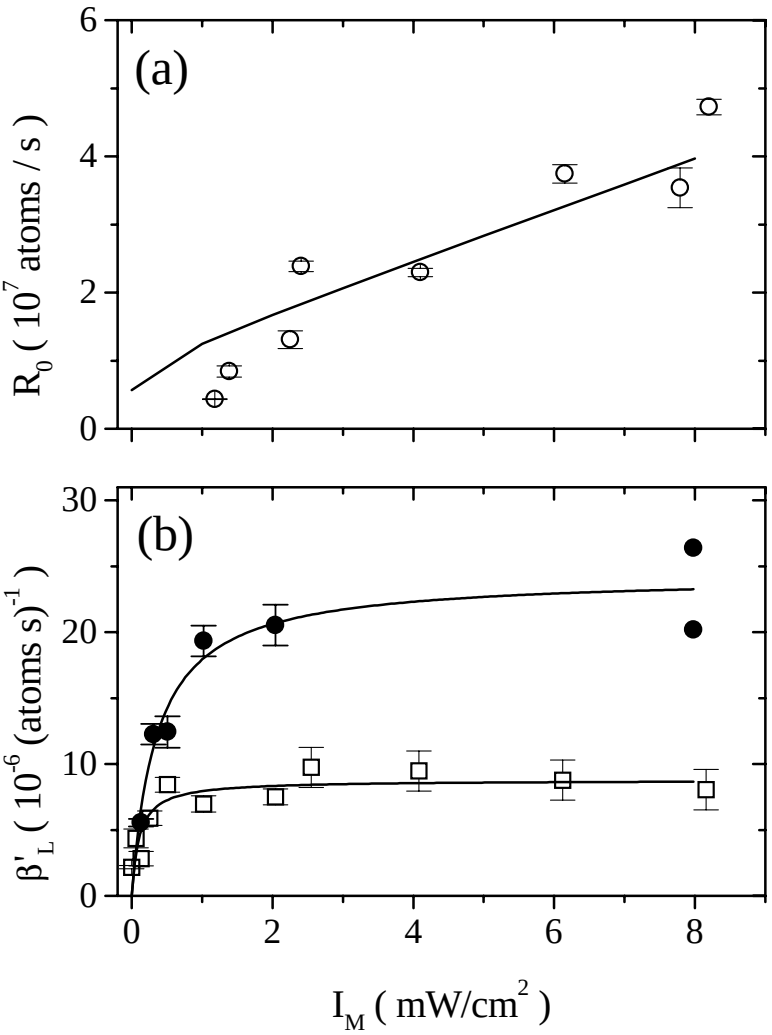

Figure 5.8: FORT loading rate R_0 (a) and loss coefficient $\beta'_{\rm L}$ (b) as a function of primary MOT light intensity, for a fixed repump intensity $I_{\rm R}$. Both (◯) and (•) represent $I_{\rm R} = 5\,\mu{\rm W}/{\rm cm}^2$, while in (□) I_R = 0. The solid lines are derived from the models in Secs.5.7.2 and 5.7.1 for (a) and (b), respectively. FORT parameters are those of Fig. 5.6.

to radiative escape are responsible for the losses during loading, as is confirmed by the model that we develop in Sec. 5.7. The solid curves in Fig. 5.6 are based on this model and agree very well with our data.

As shown in Fig. 5.8, the loading rate R_0 increases nearly linearly with $I_{\rm M}$. As will be argued in Sec. 5.7, this implies that the loading rate strongly depends on the cooling mechanisms in the MOT.

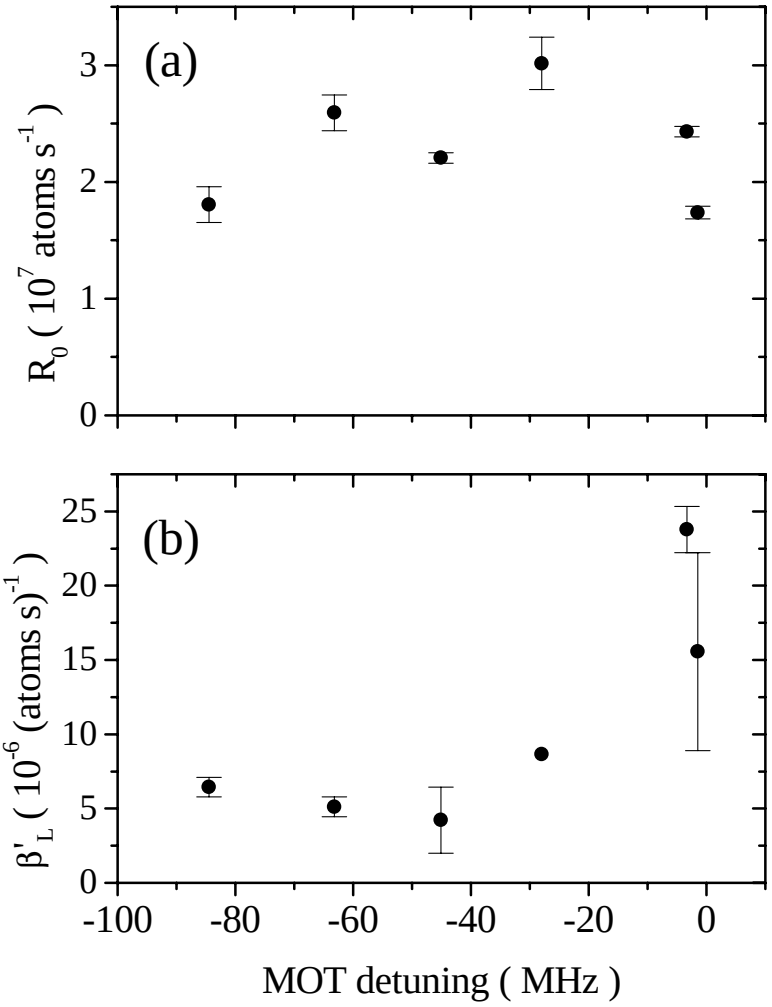

Figure 5.9: FORT loading rate R_0 (a) and loss coefficient $\beta'_{\rm L}$ (b) as a function of the primary MOT light detuning, $\Delta_{\rm M}$, during loading. The repump intensity is $5\mu{\rm W/cm}^2$. For trap parameters $w_0 = 26\,\mu{\rm m}$, $P = 300{\rm mW}$, and $\lambda = 784.5{\rm nm}$.

5.4.3 The role of MOT detuning

Both R_0 and $\beta'_{\rm L}$ also depend on MOT detuning, as shown in Fig. 5.9. For these data, $I_{\rm R}$ is reduced to the value that gives optimum loading into the FORT. A maximum in R_0 is observed at about $\Delta_{\rm M} \approx -30\,{\rm MHz}$. At slightly larger detunings the loss rate $\beta'_{\rm L}$ has a minimum. The maximum number of atoms is loaded into the FORT at a detuning that is simultaneously close to the maximum in the loading rate and close to the minimum in the loss rate.

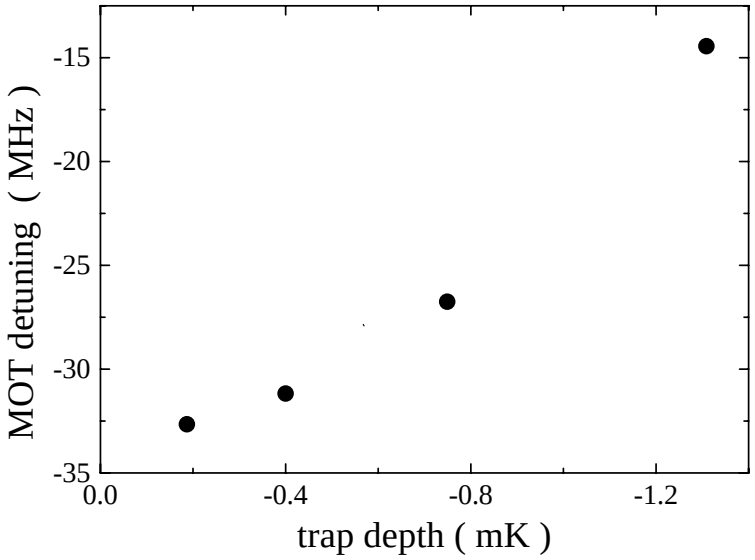

Figure 5.10: MOT detuning for maximum number of atoms loaded into the FORT versus trap depth, $w_0 = 26\,\mu\mathrm{m}$.

We also observe that the optimum detuning of the primary MOT light during the loading stage depends on the depth of the FORT. This is illustrated in Fig. 5.10. For deeper traps the optimum detuning is smaller. The FORT depth was varied by changing the wavelength and power of the FORT light.

5.4.4 Alignment with respect to the MOT

Another factor affecting the FORT loading is the relative alignment of the FORT with respect to the MOT. We find that the loading rate is optimum with a longitudinal displacement between the center of the FORT and the MOT. The optimum displacement depends on the FORT depth. Absorption imaging is used to determine the separation between the FORT and the MOT. We observe that as trap depth increases, the displacement must increase in order to maximize the number of atoms loaded. Typically the displacement between the focus of the FORT and the MOT is about half a MOT diameter.

In shallow traps the displaced loading of the atoms causes an initial sloshing of the atoms in the longitudinal direction. The sample of atoms can be seen to make one and a half oscillations before it thermalizes at the center of the FORT; this takes about 100 ms.

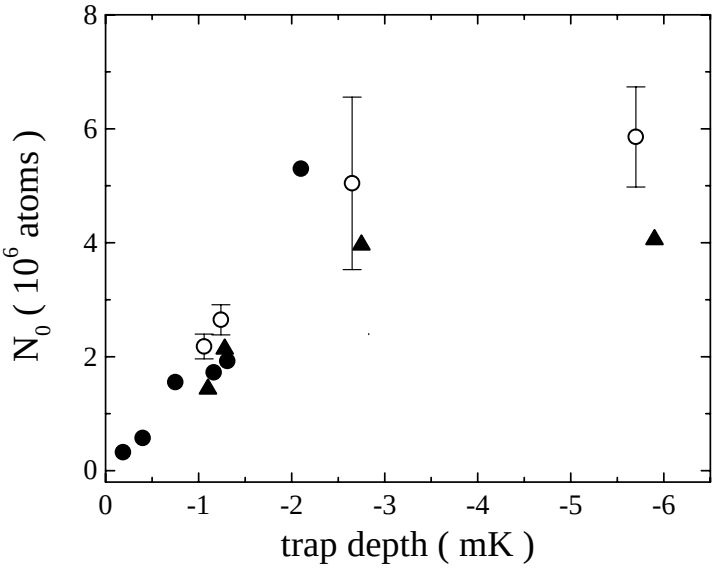

Figure 5.11: Number of atoms loaded into the FORT as a function of trap depth for $w_0 = 26\mu\mathrm{m}$ (•) and $w_0 = 22\mu\mathrm{m}$ (▲). For the latter data set the steady state number [see Eq. (5.4)] is calculated from R_0 and β'_{L} taken from Fig. 5.12, is plotted as ∘.

5.4.5 Dependence on FORT depth

We measured how the loading rate, loss rate, and total number of atoms trapped in the FORT depends on the trap depth. This is shown in Figs. 5.11 and 5.12. For each data point, the MOT detuning, repump intensity, and alignment of the FORT with respect to the MOT are optimized to give the highest number of atoms in the FORT. The waist of the trapping beam is fixed and the trap depth is varied by changing both the detuning and power of the FORT beam. The dependence of N_0 on trap depth can be explained as an increase in R_0 and a reduction of β'_{L} as the trap gets deeper. This is illustrated by the data shown in Fig. 5.12.

For comparison to the data in Fig. 5.11, we calculated N_{st} using Eq. (5.4) by inserting the measured R_0 and β'_{L} . The calculated values N_{st} (∘ in Fig. 5.11) agree well with the measured number, and depends linearly on trap depth up to 3 mK. At 6 mK, N_0 lies below the extrapolated straight line because β'_{L} cannot decrease below its value in the absence of MOT light.

For a waist of $26\,\mu\mathrm{m}$ we have observed transfer efficiencies from the MOT to the FORT of 20%. For traps with a larger waist, $w_0 = 40\,\mu\mathrm{m}$, transfer efficiencies of 40% and higher have been observed. If we compare FORTs with about the same depth of $U_0 \approx 1\,\mathrm{mK}$ but different waists, we observe that more atoms are loaded when the waist is bigger. This is mainly due to an increase of the loading rate (see Sec. 5.7.2). Changing the waist from $26\,\mu\mathrm{m}$ to $75\,\mu\mathrm{m}$, we observed a strong reduction of

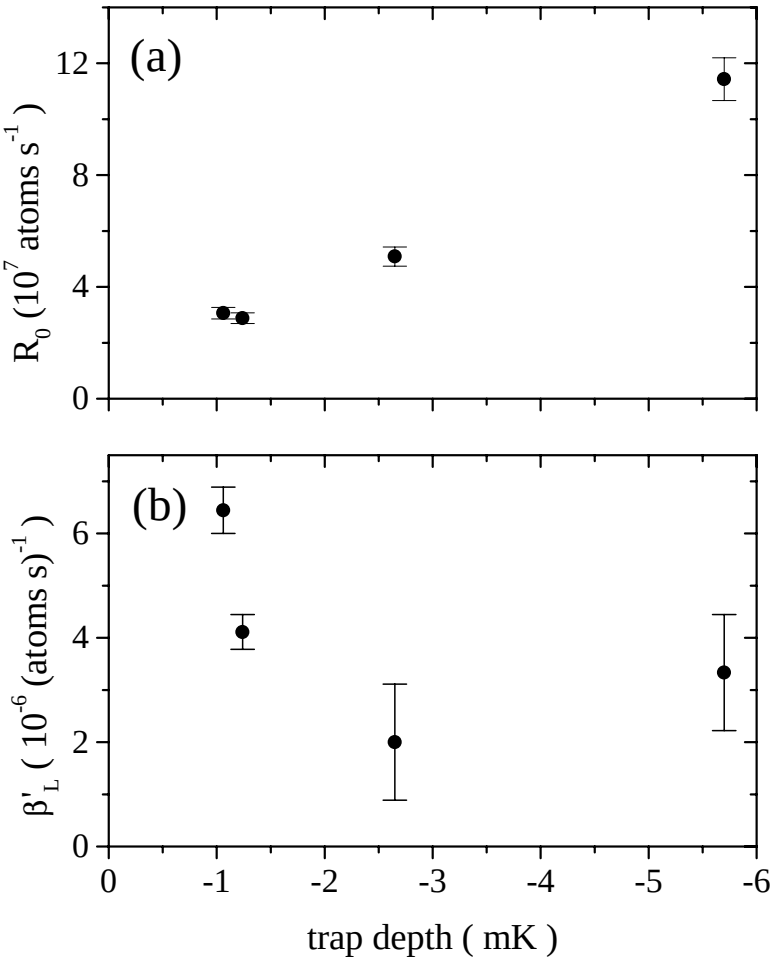

Figure 5.12: FORT Loading rate R_0 (a) and loss rate β'_{L} (b) as a function of trap depth U_0 for $w_0 = 26\,\mu\mathrm{m}$.

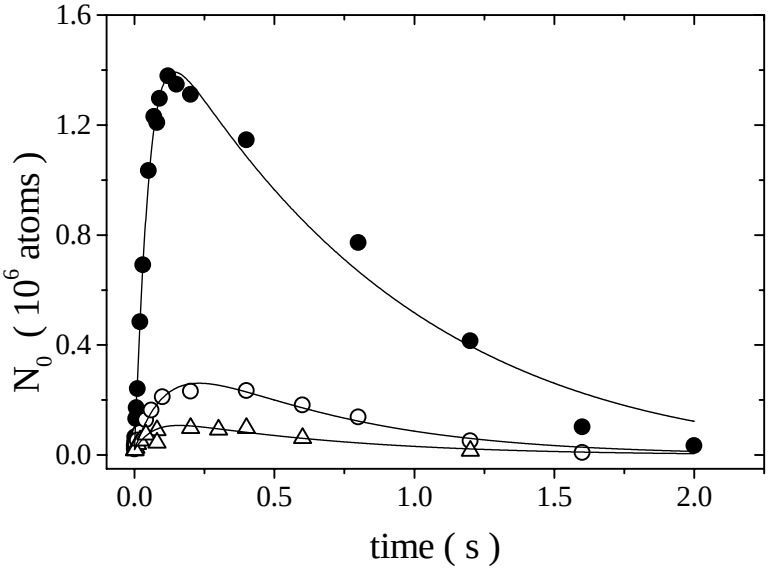

Figure 5.13: Number of atoms in the FORT as a function of loading time for three different ellipticities of the FORT light. In descending order of the curves, $\epsilon = 0.999,\ 0.915,\ \text{and}\ 0.852$. The FORT parameters are $w_0 = 22\mu\text{m}$, $P = 600\,\text{mW}$, and $\lambda = 784.5\,\text{nm}$.

the lifetime of the trapped sample. We attribute this reduction to the fact that in this regime, the scattering force becomes stronger than the trapping force and expels atoms from the trap[38].

5.4.6 The effect of elliptically polarized FORT light

As the data in Fig. 5.13 show, the polarization of the FORT light has a profound effect on the number of atoms loaded into the FORT. A change of the ellipticity (See Section 4.2) from linear polarization, $\epsilon = 0.999$, to slightly elliptical polarization, $\epsilon = 0.915$, causes the number of atoms to drop by a factor of 7. At $\epsilon = 0.852$ the number dropped by more than an order of magnitude. The drop in number is caused by a combination of effects. Analysis of the shape of the load curves in Fig. 5.13 shows that the loading rate is reduced by an order of magnitude and the exponential loss rate Γ_{L} is increased by a factor of 4. The increase of Γ_{L} we ascribe to the ground state dipole force fluctuations related to the optical Zeeman splittings [second term on right hand side of Eq. (4.1)] induced by the ellipticity of the light [41]. The optical Zeeman splittings can also be expected to interfere with the functioning of the MOT and thus reduce the loading rate. In the center of the FORT the splitting corresponds to that of a magnetic field of 13 Gauss, which is sufficient to disrupt both the cooling and trapping of the MOT.

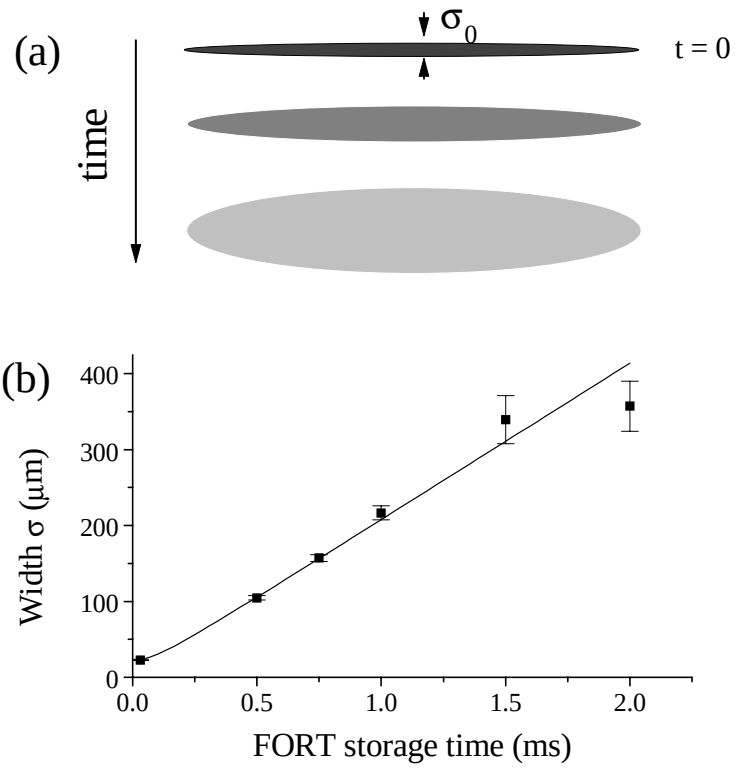

Figure 5.14: (a) Illustration of ballistic expansion and (b) an example of a temperature measurement.

5.5 Temperature

We measured the temperature of the atoms in the FORT for different trap depths. The temperature T of the atoms in the FORT was determined from the rate at which the cloud of trapped atoms expands after release. The density distribution is well described by a Gaussian of width σ that increases with expansion time t, as illustrated in Fig. 5.14 (a). The resulting σ vs. expansion time is plotted as in Fig. 5.14 (b). By fitting this data to the equation $\sigma = \sqrt{\sigma_0^2 + \frac{k_B T}{m} t^2}$, a temperature is readily extracted.

The temperature extracted from the transverse dimension was found to depend on potential well depth, as shown in Fig. 5.15. Although the transverse and longitudinal temperatures agree to within the experimental uncertainties, the transverse dimension

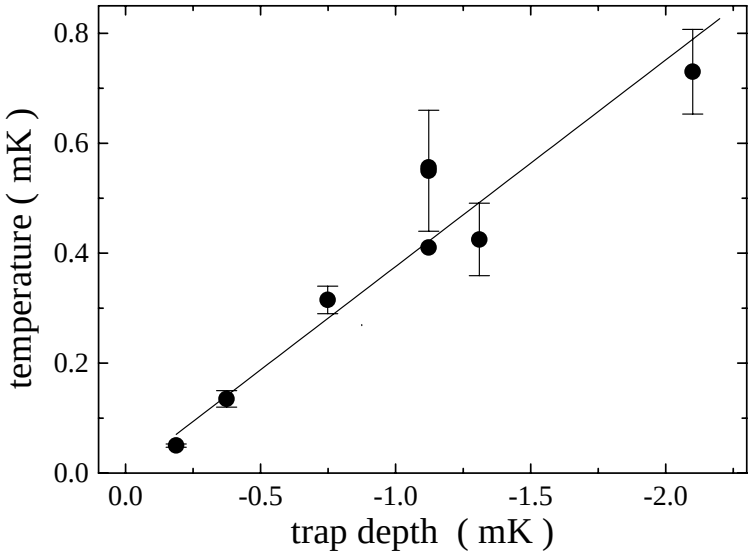

Figure 5.15: Temperature of the atoms in the FORT as a function of trap depth, for $w_0 = 26\,\mu\mathrm{m}$. Solid line is a linear regression giving a slope $T/U_0 = -0.4$.

is a much more sensitive probe of the temperature due to its smaller initial size. The initial aspect ratio of the cloud is 33 to 3000 μm. Note that for the deeper traps the temperature is much higher than that of the atoms in the MOT, which is about $30\,\mu\mathrm{K}$ to $120\,\mu\mathrm{K}$, depending on the MOT detuning. Over the range of trap depths that we investigated the temperature is a fixed fraction 0.4 of the FORT depth.

5.6 Trap Lifetime

The number of atoms in the trap decreases after the trap is loaded, as is shown in Fig.5.3. In the absence of any MOT light the loss of the trapped sample has a number dependent (collisional) portion and a purely exponential part, as described by Eq. (4.3).

Typically, the exponential lifetime $1/\Gamma$ is between 1 s and 10 s, depending on the trap parameters. The lifetime increases with decreasing FORT scattering rate, until a limit ($\approx 10\,\mathrm{s}$) is reached that we believe is set by the background vapor pressure.

The collisional loss, characterized by β', depends on the wavelength and waist size of the FORT beam. We observe clear resonances in β', consistent with photoassociation lines. Between these lines we see a nonzero background level that presumably is due to ground state hyperfine changing collisions. This background level depends on the FORT light polarization. In a circularly polarized FORT [41], the atoms are spin polarized in one of the stretched states of the $F = 3$ ground state, from which hyperfine changing collisions are suppressed. In our trap we see a factor of 2 reduction of β' in between the photo-association lines when the polarization is changed from linear to

circular.

5.7 Analysis

5.7.1 Analysis of density dependent losses

The main features that we have observed in our data are the strong increase ($\times 100$) of the collisional loss coefficient $\beta'_{\rm L}$ when the MOT light is present and that this loss rate depends strongly on the MOT parameters. As we will show in this section, density dependent losses during the loading of the FORT are mainly due to radiative escape collisions induced by the MOT light. In the unperturbed FORT, ground-state hyperfine changing collisions are the dominant loss process.

5.7.1.1 Conversion to density dependent loss

The typical mechanism driving the collisional loss process in the FORT is more easily identified when the measured rate coefficients β' and $\beta'_{\rm L}$ are converted to density related, volume independent rate coefficients β and $\beta_{\rm L}$. The relation between these is $\beta = \beta' V$, with V the volume of the sample of atoms. The volume is found by approximating the trapped sample of atoms as a cylinder with radius and length determined by the size of the FORT beam focus and the temperature of the atoms. The volume is then given by,

$$V = \pi w_0^2 z_R \ln(\frac{1}{1-\eta})\sqrt{\frac{\eta}{1-\eta}}\,, \tag{5.5}$$

where $\eta = k_{\rm B}T/U_0$ is shown in Sec. 5.5 to be a constant 0.4, regardless of the FORT parameters. Thus the volume only changes when w_0 changes.

5.7.1.2 Density dependent loss from the FORT without the MOT present

Density dependent losses from the FORT when there is no MOT light present are due to both photo-association and ground state hyperfine changing collisions, as mentioned in Sec. 5.6. Between photo-association lines, the values of β' do not depend strongly on the FORT laser power or wavelength, but change strongly with w_0. However, when β' is multiplied by $V \propto w_0^4$, the resulting $\beta = (4 \pm 2) \times 10^{-12}\,{\rm cm}^3\,{\rm s}^{-1}$, independent of w_0. This value agrees well with the value of $4 \times 10^{-12}\,{\rm cm}^3\,{\rm s}^{-1}$ reported by Miller *et al.* in Ref. [80].

5.7.1.3 Density dependent loss from the FORT during loading

In the case of loading the FORT, the density dependent losses are due to light-assisted collisions. To demonstrate this, we compare with measured rates in MOTs, where light-assisted collisions have been extensively studied. This comparison is complicated by the difference in trap depth between the MOT and the FORT (1 K vs. 1 mK), and also the difference in fractional occupation of the upper hyperfine component

of the ground state. In the case of a MOT the fractional population of the lower hyperfine component is negligible, and the loss term is written as βn^2, where n is the total density of atoms in the MOT. Then for constant temperature, β depends linearly on the intensity of the assisting light.

These light-assisted collisions, as described by Gallagher and Pritchard [81], are due to two mechanisms: fine-structure changing collisions and radiative escape. It has been shown that these two mechanisms contribute with the same order of magnitude to the trap loss [82, 83] in 1 K deep MOTs. Radiative escape is predicted to scale almost inversely with trap depth ($\beta \sim U_0^{-5/6}$) [83, 84] for trap depths $\sim$ 1 K, but the fractional contribution of fine structure changing collisions should decrease with decreasing trap depth. Therefore, we can neglect the contribution from fine structure changing collisions to β in describing the losses that occur during loading of the 1 mK deep FORT.

The fractional ground state population affects the loss rate in the following way. For radiative escape to occur, at least one of the two colliding atoms must be in the upper hyperfine ground state ($F = 3$). The MOT light is too far detuned to excite an atom from the lower ground state ($F = 2$) to a higher lying molecular state during a collision. Therefore, the loss term takes the form of $\beta n_3(n_2 + n_3)$, where n_3 is the density of atoms in the $F = 3$ state, n_2 is the density of atoms in the $F = 2$ state, and $n_2 + n_3 = n$.

The fraction of atoms in the $F = 3$ state depends on the relative optical pumping rates of the primary MOT laser ($F = 3 \rightarrow F' = 3 \rightarrow F = 2$) as compared with the repump laser ($F = 2 \rightarrow F' = 3 \rightarrow F = 3$). We derive the fraction of atoms in the $F = 3$ state from a simple two level rate equation model, which results in $n_3/n = I_{\rm R}/(I_{\rm R} + aI_{\rm M})$, where a is a constant that reflects the relative optical pumping rates. These rates depend on the AC stark shifts induced by the FORT, in addition to Clebsch-Gordon coefficients and the frequency of each laser. The average shift in the transition frequency for atoms in the FORT (Δ_{AC}) was extracted from Fig. 5.7 and found to be Δ_{AC} = 2.3 γ. This results in $a = 0.02$. The experimentally determined loss rate coefficient is then,

$$\beta'_{\rm L} = \frac{K\, I_{\rm M}}{V} \frac{I_{\rm R}}{I_{\rm R} + aI_{\rm M}}\,, \tag{5.6}$$

where K is a constant related to the density-dependent loss rates independent of optical pumping effects. We again use the volume V given by Eq. (5.5) to make the translation from the typical density-dependent loss rate to the loss coefficient that we measure in our experiments. For $w_0 = 26\,\mu{\rm m}$ we find $V = 1.3 \times 10^{-6}\,{\rm cm}^3$.

The behavior described by Eq. (5.6) is clearly seen in the measured dependence of $\beta'_{\rm L}$ on both $I_{\rm M}$ and $I_{\rm R}$ as shown in Figs.5.6(b) and 5.8 (b). The solid curves in these plots are fits of Eq. (5.6) to the data, with K the only free parameter. The fits to the different data sets give $K = (1.4 \pm 0.7) \times 10^{-16}\,{\rm cm}^5{\rm mW}^{-1}{\rm s}^{-1}$, where the spread is due to the different values we find by fitting different data sets. We see that Eq. (5.6) gives a good description of the measured MOT and repump intensity dependencies of the loss rate during loading of the FORT.

For a comparison of our numbers with those normally found in MOTs we set

$n_3/n = 1$, assuming all atoms are in the $F = 3$ ground state as they are in the MOT studies with which we want to compare. Thus $\beta_{\rm L} = K\, I_{\rm M}$. For $I_{\rm M} = 10{\rm mW/cm}^2$ we find $\beta_{\rm L} = 1 \times 10^{-9}$ cm^3/s. In contrast, a MOT with comparable powers and detunings has a loss rate of $1 - 4 \times 10^{-12}\,{\rm cm}^3/{\rm s}$ [85, 86, 87, 84], which is a factor of 250 to 1000 smaller than our measured value. As shown below, this difference is due to the smaller depth of the FORT.

In order to explain the increased loss rate observed during loading of the FORT as compared to a MOT we will discuss in more detail how the FORT depth affects the radiative escape loss rate. In the case of a MOT, the dependence of β, due to radiative escape, on the trap depth is predicted to go as $U_0^{-5/6}$ in the limit of large trap depths [83, 84]. However, some of the assumptions used to derive this dependence break down at smaller trap depths. Therefore, to calculate $\beta_{\rm L}$ for the FORT we perform a numerical calculation of the radiative escape process, using the semi-classical Gallagher-Pritchard (G-P) model [81]. Given the uncertainties in our measured $\beta_{\rm L}$, a more detailed calculation is unwarranted. Therefore, we do not include angular momentum considerations or enhanced survival probability as described by Julienne and Vigue [83] or any corrections for the hyperfine splittings as introduced by P. Lett et al. [82]. Instead, we approximate all of the involved intramolecular potentials as a single $-C_3/r^3$ in the GP model as formulated by Peters et al. [88] and integrate numerically.

Figure 5.16 shows an approximate intramolecular potential for Rb. For initial excitation at radius r_0, atoms are accelerated toward one another for some time before spontaneous emission leaves two ground-state atoms with more kinetic energy than they had initially. If the kinetic energy picked up in the collision exceeds the depth of the trap, both atoms will be lost. The radius at which the pair acquires exactly enough energy to be ejected from the trap is therefore called the critical radius r_c, and the time required for the atoms to reach this is called t_0.

Once the atoms reach r_c, acceleration is very fast, and the atom pair spends a short time t_1 accelerating to $r = 0$. If spontaneous emission does not occur during this second time interval, the intramolecular separation will oscillate between 0 and r_0, making multiple orbits until spontaneous emission occurs. The probability of a lossy radiative escape event thus depends on the excitation probability at r_0 and the probability of decay occurring when $r < r_c$. Following Refs.[88] and [89] we find

$$\beta \propto \int 4\pi r_0^2 dr_0 G(r_0) P_{RE}(r_0)\,, \tag{5.7}$$

where the photon scattering rate of atoms in the $F = 3$ state, $G(r_0)$, is a function of the effective detuning $\Delta(r_0) = -C_3/(r_0^3\hbar) + \Delta_M$ with respect to the unperturbed atomic transition frequency. The probability of a radiative escape event resulting in trap loss is $P_{RE} = \sinh(\gamma t_1)/\sinh[\gamma(t_0+t_1)]$, which reflects the important contribution of multiple orbits [88].

The result of the numerical integration of Eq. (5.7) for different trap depths is show in Fig. 5.17. The dashed line indicates a dependence of $\beta \sim U_0^{-5/6}$ as predicted by Refs. [83] and [84]. This clearly tracks our numerical integration at large trap depths, where it is expected to be valid. Examination of the change in β with U_0 shows that

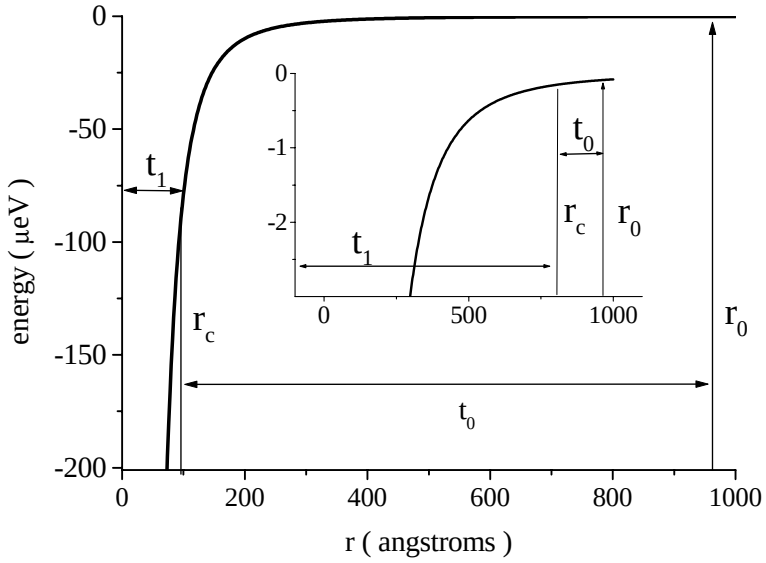

Figure 5.16: Approximate intramolecular potential for Rb, with $C_3 = 71\,\text{Å}^3\,\text{eV}$. The large graph shows the critical radius, r_c, for $U_0/k_\text{B} = 1\,\text{K}$, while the inset depicts the same parameters for $U_0/k_\text{B} = 1\,\text{mK}$.

for a change in U_0 from 1 K to 1 mK, β increases by a factor of $\sim$50 (for $n/n_3 = 1$). This ratio is at least a factor of 5 smaller than the experimentally observed ratio of 250. However, given the large uncertainties in the experimental determination of n and n_3/n, as well as the approximations that go into the calculations and the steep dependence of the results, the measured and calculated numbers are not inconsistent. Therefore we believe that the enhanced loss rates we observe during loading are consistent with light-assisted collisions.

5.7.2 A model for the FORT loading rate

The initial loading rate is the flux of atoms into the volume of the FORT times the probability for an atom in this volume to become trapped;

$$R_0 = \frac{1}{4} n_\text{MOT} \bar{v} A P_\text{trap}\,, \tag{5.8}$$

where n_MOT is the density in the center of the MOT, $\bar{v} = k_\text{B}T/m$ is one dimensional component of the root mean square thermal velocity of the atoms in the MOT, A is the effective surface area of the FORT, and P_trap is the trapping probability. For the discussion below we will assume that the MOT density is constant in time, i.e. n_MOT is the density at the start of the loading stage.

The dependence of R_0 on MOT detuning is plotted in Fig. 5.9. The loading rate shows a maximum at $\Delta_\text{M} = -30\,\text{MHz}$, the same detuning at which the measured

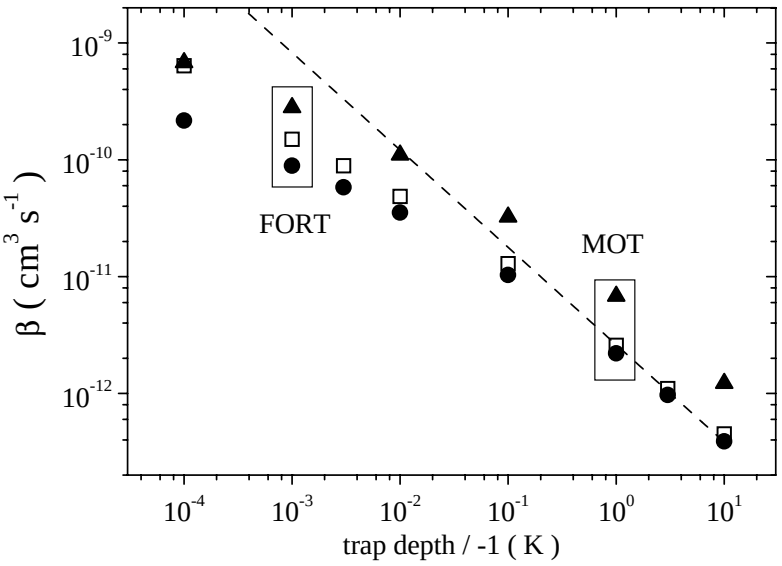

Figure 5.17: Radiative escape loss rate coefficient β calculated as a function of the absolute value of the trap depth. When the atoms have zero initial kinetic energy, (▲) correspond to β values for $\Delta_{\rm AC} + \Delta_{\rm M} = 2\gamma$ and (•) to 8γ. (□) depict 8γ, but with an initial relative velocity $v = k_{\rm B}T/m$, corresponding to $T = 800\,\mu$K. The dashed line represents $\beta \propto U_0^{-5/6}$ as mentioned in the text.

product $n_{\rm MOT}\sqrt{T}$ plotted in Fig. 5.18 has a maximum. This supports the idea that $R_0 \propto n_{\rm MOT}\bar{v}$, assuming that $AP_{\rm trap}$ is constant with MOT detuning.

The loss rate $\beta'_{\rm L}$ has a minimum at a slightly larger detuning. The maximum number of atoms will be loaded into the FORT at a detuning close to the maximum in the loading rate and simultaneous minimum in the loss rate. This is illustrated by substituting the measured R_0 and $\beta_{\rm L}$ into Eq. (5.4). Thus calculated the number of atoms transfered into the FORT clearly shows a maximum at a detuning of 35 MHz (see Fig. 5.18). In the same figure we plotted the actual measured number of atoms. The agreement is very good over the detuning range of interest, 0-30 MHz. The difference between the calculated and measured numbers at large detunings is caused by the rapid loss of atoms from the MOT, which prevents N from reaching the value predicted by Eq. (5.4).

The loading rate R_0 depends on A, in addition to $n_{\rm MOT}\sqrt{T}$. For a trap with a waist of 26μm the Rayleigh range is $1.5\,$mm. This is a few times larger than the diameter of the cloud of atoms trapped in the MOT, $D_{\rm MOT}$. This means that the FORT radius hardly changes over the width of the MOT. Therefore we approximate A by the surface area of a cylinder with length given by the MOT diameter $D_{\rm MOT}$ and an effective radius $r_{\rm eff}$, that is a function of z and depends on the FORT waist. The radius

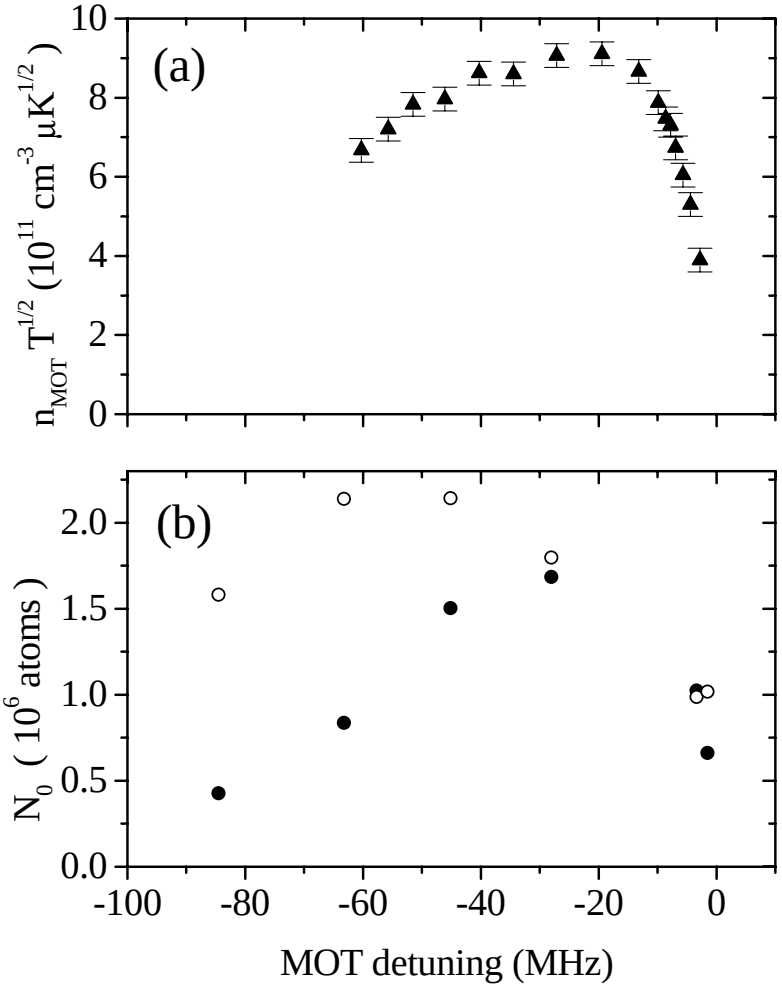

Figure 5.18: Product of MOT density and the square root of temperature (a) and number loaded into FORT (b) as a function of the MOT detuning during FORT loading. The actually measured number (●) and the number calculated from Eq. (5.4) (○) are both shown in (b). The FORT parameters are those of Fig. 5.9.

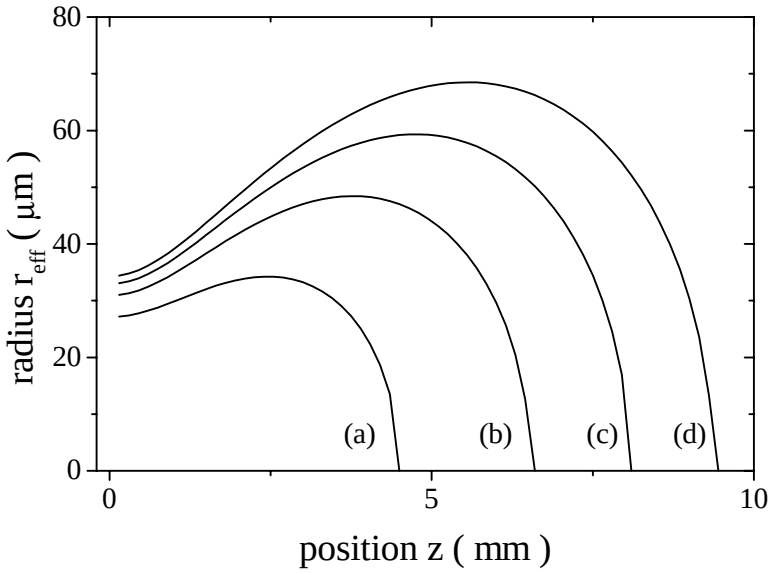

Figure 5.19: Equipotential contours of the FORT for $E/k_{\rm B} = -100\,\mu{\rm K}$ and $U_0/k_{\rm B} = -1,\ -2,\ -3,\ {\rm and}\ -4\,{\rm mK}$ depth , (a)-(d) and $w_0 = 26\,\mu{\rm m}$.

is set by the coordinates at which the FORT potential becomes the same size as the temperature of the atoms in the MOT, $U(r_{\rm eff}, z) = U_c \approx -k_{\rm B}T$. The effective radius $r_{\rm eff}(z)$ of the FORT, depending on z and U_c is then

$$r_{\rm eff}(z) = w_0 \left[(1 + (z/z_R)^2)\, \ln(\frac{U_0}{U_c} \frac{1}{2(1 + (z/z_R)^2)}) \right]^{\frac{1}{2}} . \qquad (5.9)$$

In Fig. 5.19 this equipotential contour is plotted for different values of U_0 and $U(r_{\rm eff}, z) = -100\mu{\rm K}$. The bow tie shape of these contours explains why the best loading is achieved when the FORT and MOT are displaced. The radius has a maximum away from the focus. Moreover, for deeper traps the z at which the maximum radius occurs shifts to bigger z values, just as in the data.

A typical initial MOT density during the FORT loading stage is $2 \times 10^{11}\,{\rm cm}^{-3}$, and the temperature ranges from $30\,\mu{\rm K}\,{\rm to}\,100\,\mu{\rm K}$ depending on detuning of the primary MOT light. A reasonable value for the average speed in one dimension is thus $\bar{v} = 5\,{\rm cm/s}$. The MOT diameter is $500\,\mu{\rm m}$ (FWHM). For $U_0 = -1\,{\rm mK}$ and $U_c = -100\,\mu{\rm K}$ the area $A = 1 \times 10^{-3}\,{\rm cm}^2$. Using these numbers the loading rate is $2.5 \times 10^8\,{\rm s}^{-1}$ if the trapping probability $P_{\rm trap} = 1$. The loading rate measured for such a trap is $3 \times 10^7\,{\rm s}^{-1}$, implying $P_{\rm trap} \approx 0.1$.

The data in Fig. 5.8 show that the loading rate increases nearly linearly with MOT intensity. However, it is known that the MOT temperature and density in the Sub-Doppler regime scale as intensity and the inverse square root of intensity, respectively [74, 90].

The product $n_{\rm MOT}\bar{v}$ is thus expected to show no strong dependence on MOT intensity. We have experimentally confirmed this by measuring the density and temperature of the cloud of MOT atoms as a function of MOT intensity. Over the range of MOT intensities as in Fig. 5.8 we find that $n_{\rm MOT}\bar{v}D_{\rm MOT}$ is nearly constant. Therefore, we conclude that the observed increase of the loading rate with increasing MOT intensity arises from an intensity dependence of the trapping probability $P_{\rm trap}$. From the data we find $P_{\rm trap} \approx 0.1$

We estimate $P_{\rm trap}$ by using the following simple model. The atoms come into the trapping volume with a narrow distribution of velocities around an average velocity $\bar{v}$. To be trapped, an atom's energy has to be reduced to below the edge of the trapping potential. The time scale for this to happen must be about half an oscillation period $\tau/2$ of the FORT in the strong direction, which is $150\ \mu$s for the above mentioned trap. The scattering of MOT laser photons affects the atomic velocity in two ways. First, the atom scatters photons that leads to heating, that is, a broadening of its velocity distribution. The spread in velocity due to photon scattering is $\sigma = \sqrt{\frac{1}{3}(\frac{\hbar k}{m})^2\Gamma_{\rm scat}\ \tau/2}$. Second, the frictional component of the scattering leads to a reduction of the atom's average kinetic energy. The rate at which the atom loses energy is $\dot{E} = -\alpha\bar{v}^2$. This damping leads to a change in average velocity of $\Delta v = \bar{v}\sqrt{\frac{\alpha\tau}{m}}$ in the characteristic time $\tau/2$.

The probability of being captured is the integral of the shifted and broadened distribution

$$P_{\rm trap} = \int_{\bar{v}-\Delta v}^{\infty} \frac{1}{\sqrt{2\pi}\sigma}\exp[-\frac{v^2}{2\sigma^2}]dv\ . \tag{5.10}$$

The integral leads to

$$P_{\rm trap} = \frac{1}{2}1 - {\rm erf}[\frac{\bar{v}}{\sqrt{2}\sigma}(1 - \sqrt{\frac{\alpha\tau}{m}})]\ . \tag{5.11}$$

For $\Delta_{\rm M} = 30\ {\rm MHz}$ and $I_{\rm M} = 6\ {\rm mW/cm^2}$ the MOT scattering rate $\Gamma_{\rm scat} = 9.5\times10^5{\rm s}^{-1}$, which makes $\sigma = 6\ {\rm cm/s}$.

We obtain a value of α from the formula given in Ref.[84]. The damping rate calculated from this formula increases linearly with MOT intensity for the velocities we are interested in. The values of α and σ also depend on MOT detuning. There is a strong spatial dependence of the effective MOT detuning due to the light-shift induced by the FORT. We make the crude approximation that the MOT is shifted out of resonance by half the FORT light-shift. This results in $\bar{v}/\sigma = 2$ and $\alpha/m = 200\,{\rm s}^{-1}$. The result of this model is plotted as a solid curve in Fig.5.8 and shows good agreement. This is a very approximate treatment but it clearly supports our general interpretation of the loading process.

5.8 Discussion

From our understanding of the loss process and the loading rate we are now in a position to explain the dependencies presented in Sec. 5.4. We saw that more atoms

are loaded into deeper FORTs, because the loading rate increases and the loss rate decreases. The loading rate increases because the effective FORT radius increases with trap depth, which enhances the flux of atoms into the trap. The loss rate decreases because the probability of light-assisted collisional loss decreases when the trap is deeper. In addition, the light-shift of the trap increases the effective detuning of the MOT light and repump light for the atoms in the trap, which reduces their excitation rate, and therefore reduces radiative escape.

The data in Fig. 5.10 shows that the MOT detuning at which loading is optimized is smaller for deeper FORTs. A deeper trap means larger light shifts of the atoms. The MOT detuning and the repump detuning are both shifted blue, so that the detuning of both lasers from the atoms becomes more negative (red) in both cases. Due to the increased effective detunings the MOT cooling rate decreases and thus the trapping probability decreases. By choosing a smaller MOT detuning the loading rate is increased.

The dependence on MOT detuning of the β'_{L} that we measured for a given trap depth (see Fig. 5.9) is also well described by Eq. (5.6). The detuning dependence enters through the parameter a. At small MOT detunings, the MOT excitation rate is highest and therefore β'_{L} is large. By increasing the MOT detuning further a becomes smaller. Therefore aI_{M} becomes negligible compared to I_{R} and β'_{L} becomes independent of detuning.

In Sec. 5.4.1 it was shown that loading is optimized for repump light of very low intensity that is tuned on resonance. We saw that the number of atoms in the FORT dropped when the repump intensity was increased but the repump scattering rate was maintained by changing the repump detuning. Increasing the repump intensity increases the loss rate. Although the detuning is increased for the atoms in the MOT such that the scattering rate is the same for the MOT atoms, the increased intensity still causes an increased scattering rate for the atoms trapped in the FORT.

5.9 Enhanced and quasi continuous loading

The previous data and analysis shows that β'_{L} is very small when the repump power is zero, and reducing the primary MOT intensity also helps to reduce the loss rate. However, reducing these light intensities also reduces the loading rate. It is possible to improve the ratio of loss to loading rate by changing the beam geometry. The loss rate only has to be eliminated in the volume where the FORT is, which can be done by inserting obstructions to block portions of the MOT beams and the repump beam.

To demonstrate this concept, we make a shadow in the repump beam. For this purpose an additional repump beam is used that co-propagates with the FORT beam. A $0.6\,\mathrm{mm}$ opaque disk in this beam is imaged into the MOT and FORT region, such that the shadow covers the length of the FORT. The peak intensity in this repump beam is increased from $5\,\mu\mathrm{W/cm^2}$ to 460 $\mu\mathrm{W/cm^2}$, which is sufficient to prevent the MOT from being lost while loading the FORT. The MOT is still loaded as before using a repump beam without a shadow. During the loading of the FORT, that repump beam is switched off, and the shadowed beam switched on. In Fig. 5.20 we show two measured

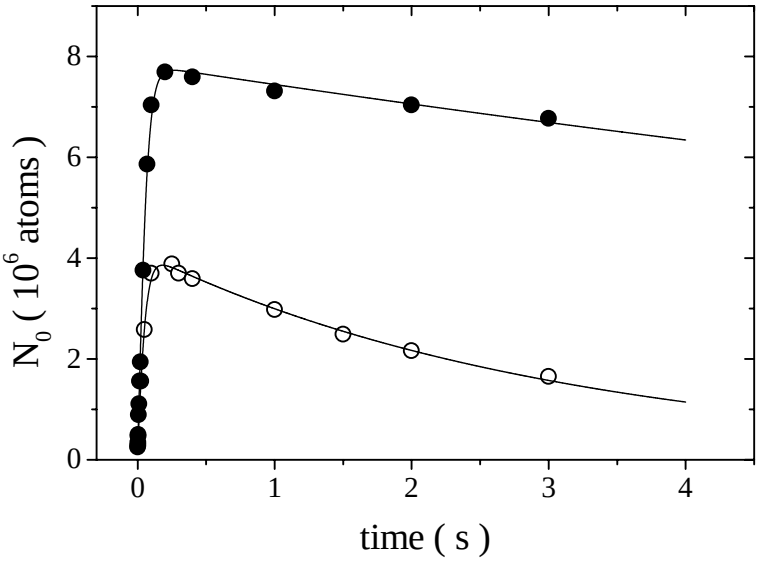

Figure 5.20: Number of atoms loaded into the FORT as a function of loading time, using normal loading (∘) and enhanced loading with a shadowed repump beam (•). The FORT parameters are $w_0 = 58\,\mu\mathrm{m}$, $P = 580\mathrm{mW}$ and $\lambda = 783.2\mathrm{nm}$. The solid curves are fits of Eq. (5.3) to the data.

loading curves. One shows loading using the conventional method without the shadow and with reduced repump power, and the second curve shows the new method with the shadowed beam and increased repump power. The maximum number of loaded atoms doubles from 3.9×10^6 to 7.7×10^6. The transfer efficiency from MOT to FORT increased from 21% to 42 %.

The increase in the number is caused by a decrease of the loss rate from $\beta'_{\mathrm{L}} = (3.5 \pm 0.5) \times 10^{-6}\mathrm{s}^{-1}$ to $\beta'_{\mathrm{L}} = (1.7 \pm 0.3) \times 10^{-6}\mathrm{s}^{-1}$ and a simultaneous increase of the loading rate, from $R_0 = 5.8 \times 10^7\mathrm{s}^{-1}$ to $R_0 = 10.2 \times 10^7\mathrm{s}^{-1}$, respectively. The loading rate is increased due to the fact that the MOT density increases by reducing the repump intensity in the center of the MOT.

The loss rate β'_{L} is still larger during loading with the shadow than in the absence of all MOT light, where the loss rate $\beta' = 2.3 \times 10^{-7}\,\mathrm{s}^{-1}$. This is due to the fact that the MOT light is not shadowed and the FORT acts as a very weak repump laser. Thus putting additional shadows in the main MOT light may improve the loading even more, but this requires a more complicated optical setup. By reducing β'_{L} to the limit of no MOT light, while maintaining the same loading rate, the steady state number of atoms would be 2×10^7, which would be nearly all of the MOT atoms.

5.10 Conclusions

Our study can be summarized as follows. Deeper traps load more atoms and the temperature is a fixed fraction of the trap depth. Optimum loading is achieved for very low repump scattering rate ($I_{\mathrm{RP}} = 5\,\mu\mathrm{W/cm^2}$), and a MOT detuning that depends on the FORT depth. Controlling the geometry of the overlap of the MOT and FORT beams gives substantial improvement. To maximize the number of atoms trapped in the FORT, these are the parameters to adjust.

However, underneath this recipe lies a lot of interesting physics. Loading the FORT from a MOT is a dynamical process, governed by a loading rate R_0 and density dependent losses characterized by β'_{L}. During the loading the MOT light fields increase the FORT loss rate considerably. The main loss mechanism during loading of the FORT is radiative escape collisions induced by the MOT light fields. The loss rate is higher than in a MOT because the FORT is only on the order of a mK deep, whereas a typical MOT is a K deep. In addition, the light-shift due to the FORT changes the balance of optical excitation of the MOT trapping and cooling light, which is responsible for the radiative escape, and the hyperfine repump rate. Taking these effects into account we were able to model how the loss rate depends on the intensities and detunings of the primary MOT and repump lasers, as well as the FORT depth. This model explains the experimentally observed dependencies of the loss rate on these parameters very well. The loading rate can be described in two parts: a flux of atoms into the volume of the FORT times a probability of being trapped. Both parts depend on the MOT and FORT parameters, including the size of the FORT.

Here we studied the loading of a FORT with a radius $\leq 60\,\mu\mathrm{m}$, which is much smaller than the radius of the MOT. Even with this mismatch of size between the MOT and the FORT we were able to transfer more than 40% of the atoms initially trapped in the MOT to the FORT. For FORTs with a radius comparable to that of the MOT the description of the loading rate changes, and also the loss rate may behave differently. However, we believe that radiative escape processes may still be enhanced as compared to a MOT. Working with a small waist enables one to make deeper traps and achieve tighter confinement. Such conditions may make it possible for instance to reach Bose Einstein condensation at high temperatures of tens of micro-Kelvin.

Chapter 6

Cooling in the Circularly Polarized Optical Dipole Trap

6.1 Motivation

Cooling of atoms in a trap using completely optical techniques is an important pursuit of atomic physicists. Optical traps offer rapid control and tight confinement. Optical cooling techniques allow the cooling process to be decoupled from the thermal collisional process, allowing very low temperatures to be achieved while minimizing potentially lossy collisions. A circularly-polarized dipole trap offers a variety of non-degenerate states in which to work, much like a magnetic trap does. Thus many cooling mechanisms previously available only in magnetic traps are available in the circular FORT, and can be implemented optically.

Many schemes exist to cool atoms in red-detuned optical dipole potentials. Evaporative cooling via relaxation of the potential has been used to reach temperatures of 4 μK [76], but so-called run-away evaporation was not possible in this scheme because the density of atoms decreases as the potential increases. Raman cooling has also been demonstrated in a dipole trap formed with YAG lasers [91].

Many techniques are employed in optical lattices as well. They include Raman cooling, evaporative cooling, adiabatic expansion, sideband and degenerate sideband cooling [92, 93]. However, optical lattices can be difficult to construct and leave atoms in many different potential wells instead of the same potential well.

Sisyphus cooling refers to any cooling process in which an atom dissipates kinetic energy by physically moving into a region of space in which it loses kinetic energy to potential energy, then changes its internal state to one with smaller potential energy before it leaves the elevated potential. In this way, the atom can be described as continually rolling up hill, much like the mythical Greek Sisyphus was forced to push a boulder eternally uphill. Many different types of Sisyphus cooling exist. It is an essential part of polarization-gradient cooling, which manifests itself as the sub-Doppler cooling mechanism in MOTs [12, 13]. In addition, gravitational Sisyphus cooling [45] employed the Sisyphus cooling concept to two potentials with nearly the same curvature, but displaced from one another. Evanescent wave cooling [94, 95] employs the mechanism as atoms bounce off an evanescent wave atom mirror. Sisyphus cooling is in general much more efficient than Doppler cooling, because a huge fraction of an atom's total energy can be carried away for the cost of 1 recoil photon. The ratio of the potential energies of the two internal states involved sets the amount of energy that can

be extracted in an event. A Sisyphus cooling mechanism clearly presents itself in the circular FORT, where internal energy levels are non-degenerate and separated by much more than the energy of one photon recoil.

Blue Sisyphus cooling (BSC) has been successfully employed to load a dipole trap [69]. Atoms were successfully loaded into linearly polarized YAG traps with temperatures of 2 – 10 μK. In this way, phase space densities of over 10^{-3} were achieved with 10^4 atoms in an individual potential. The BSC scheme is more similar to the Sisyphus cooling of MOTs, in that the potentials used for cooling are applied by additional lasers, and not supplied by the confining light.

Evaporative cooling is also a very powerful cooling mechanism. By removing the highest energy atoms and allowing the remainder to rethermalize, temperatures of alkali atoms have been reduced many orders of magnitude. In fact, to date it is the only cooling mechanism that remains powerful enough over many orders of magnitude in temperature to achieve Bose Einstein condensation [1]. Evaporative cooling has also been demonstrated in optical dipole potentials, but not without at the same time reducing the spring constant of the trap [76]. Unfortunately, this reduction simultaneously reduces the confinement of the potential, which therefore also reduces the density of the atoms and the collision rate of the atoms. Forced evaporation in magnetic traps, in contrast, can maintain the shape of the potential while removing the fastest atoms from the trap. Such a scheme is possible in the circular FORT just as it is in magnetic traps, and allows for close control of the rate of evaporation, which is necessary for optimization. Forced evaporative cooling has not yet been demonstrated in an optical dipole trap, to our knowledge.

In this chapter, we demonstrate significant cooling in the circular FORT coupled with an increase in phase-space density. The mechanism involved is most likely a combination of forced evaporative cooling and Sisyphus cooling. Preliminary results indicate that these cooling mechanisms are viable. Although these promising results are far from optimized, they point to a powerful new cooling technique for optical dipole traps.

6.2 Theory

6.2.1 Sisyphus Cooling Mechanism

Any Sisyphus cooling mechanism requires that an atom roll up a steep conservative potential gradient, undergo a transition to a different internal state, roll back down a shallower conservative potential, and then be "recycled" to the initial state. This can be accomplished in the circular FORT as shown in Fig. 6.1. Atoms start in the $|F, m_F >= |3, +3 >$ state, labeled $|a >$ and described with a potential depth U_a. An atom rolls up the side of the potential, converting kinetic energy to potential. Near the turning point of its oscillation, the atom is driven into an internal state with a smaller AC Stark shift labeled $|b >$ and described with a potential depth U_b. An example with $|b > = |3, +2 >$ is shown in Fig. 6.1 (a). The atom then rolls down the shallower potential, in which it gains less kinetic energy than it originally started with. By re-

pumping the atom back to the $|3,+3>$ state at the bottom of the potential, the atom returns to its initial position and internal state with less kinetic energy, closing the cooling cycle. It is then ready to be cooled again. The energy has been carried away by the electro-magnetic fields involved in the transitions.

Many types of transitions can be used to drive this cooling mechanism. Here they are discussed in two categories: the "drive" transitions that excite the atoms to shallower potentials near their turning points, and the "repumping" transitions used to return the atom to the deeper potentials at the bottom of the potential. Figure 6.1 (a) depicts one embodiment of the cooling scheme using a "rf drive", in which a rf photon drives the atoms into the $|3,+2>$ state, and then the atoms absorb a photon from the circular FORT laser beam to repump them. Figure 6.1 (b) depicts a similar mechanism, where the drive is now an optical two-photon stimulated Raman transition. This transition is induced by an additional "Raman" laser with two frequency components separated by the ground state hyperfine splitting of 3035 MHz plus the difference in their AC Stark shifts at the turning point of the atom. This "microwave drive" can be used in conjunction with the FORT repump described above. Or, an additional repumping laser can be added to provide better state selectivity and more preferentially repump the atoms back to the $|3,+3>$ state to complete the cycle.

The rf and microwave drives each have their advantages and disadvantages. The rf drive is conceptually simpler than the microwave drive as a means to initiate the Sisyphus cooling, since only one photon is required to cause a transition between neighboring m_F states. No additional spontaneous photon scattering is added using the RF drive, whereas the lasers used to create the two-photon Raman transitions also cause additional light scattering. This scattering can cause both simple recoil heating and also heating via the ground state dipole force fluctuations described in Chapter 4. However, one rf cycle generally extracts smaller amounts of energy because the potential energy differences between the levels involved in the rf cycle are generally smaller than those of the microwave cycle.

To implement cooling using the microwave drive, one must maximize the frequency of cooling cycles while minimizing the additional heating rates. Figure 6.2 shows both the spontaneous scattering rate and the resonant Rabi frequency induced by the Raman laser as a function of both the Raman laser frequency and intensity. The resonant Rabi frequency is an important factor in determining the probability that an atom undergoes the two-photon Raman transition. If the atoms were continually resonant with the microwave modulation, they would undergo Rabi flopping between the two states with this frequency. Because the microwave transition actually involves a two-photon stimulated Raman process, $\Omega^{eff}_{m_f m_i}$ depends on the intensity of each frequency component as [96]:

$$\Omega^{eff}_{m_f m_i} = 7.4 \times 10^{13} \frac{\sqrt{I_1 I_2}}{\Delta} f_A(m_f m_i), \tag{6.1}$$

where f_A is a numerical factor depending on the Clebsch-Gordon coefficients between the initial and intermediate states and between the final and intermediate states. For $\Delta m = +1$ transitions, $f_A \approx 0.2$. I_1 and I_2 are the intensities of the two frequency

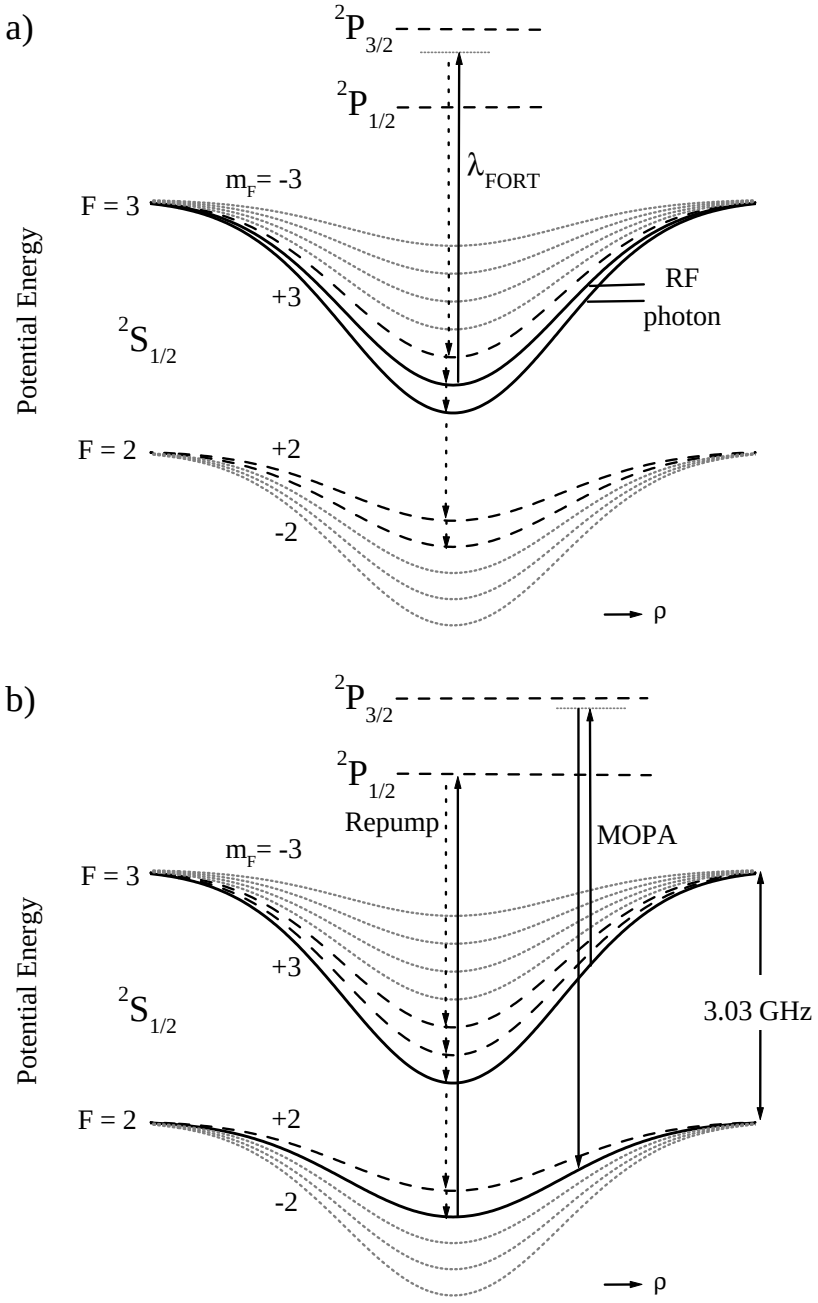

Figure 6.1: Schematic of Sisyphus cooling mechanism utilizing (a) Radio-Frequency transitions to drive the cooling and the FORT spontaneous scattering to repump, and (b) "microwave" two-photon stimulated Raman transitions to drive and an additional laser at 795 nm to repump. The microwave drive shown in (b) will also yield cooling in conjunction with the FORT spontaneous scattering repump shown in (a), as is later demonstrated.

components, in units of mW/cm^2. Both $\Omega^{eff}_{m_f m_i}$ and the detuning of the laser from resonance with the intermediate state Δ are in units of rad/s.

The effective Rabi frequency changes with laser detuning and intensity, as shown in Fig. 6.2 with a solid line. A dashed line demonstrates the photon scattering rate of atoms in the FORT under the same conditions. In order to use the two-photon Rabi frequencies for cooling, one must find a regime in which the Rabi frequencies are high enough while the heating due to photon scattering is low. To find the optimum detuning and intensity, we must evaluate the drive transition rate.

The rate of atoms making a transition between $|3,+3>$ and $|2,+1>$ is strongly influenced by the presence of the AC Stark shifts. As the atom oscillates in the potential, it sweeps into and out of resonance with the drive field at a fixed microwave frequency. This is exactly analogous to a Landau-Zener transition in which the atom is stationary and the drive frequency is swept from $-\infty$ to ∞. The more adiabatically (slowly) the frequency is swept, the larger the transfer of population from one state to another in the absence of dephasing (see for example Ref. [97]). This is expressed mathematically by writing the probability P_{LZ} of transferring atoms during one sweep through resonance as [98]

$$P_{LZ} = 1 - \exp(-2\pi\Gamma_{LZ}) \tag{6.2}$$

where the Landau-Zener parameter $\Gamma_{LZ} = \Omega^2_{eff}(4d\omega_{rf}/dt)^{-1}$. Then $d\omega_{rf}/dt$ is the rate of change of the atom's resonant frequency due to the change in position of the atom with time:

$$\frac{d\omega_{rf}}{dt} = \frac{1}{\hbar}\frac{d}{d\rho}[U(3,+3,\rho) - U(2,+1,\rho)]\frac{d\rho}{dt}. \tag{6.3}$$

$U(F, m_F, \rho)$ is given in Eq. (4.1) and Eq. (4.2). The probability of an atom changing state while oscillating through resonance and back again is $2P_{LZ}(1 - P_{LZ})$.

The velocity of atoms and slope of the potential are continually changing. Therefore, the probability of an atom changing state as it oscillates depends on the frequency of the microwave modulation or analogously on the location in the trap at which the difference in AC Stark shifts between the two states exactly equals the microwave drive frequency. Figure 6.3 shows the probability of an atom changing state, assuming that the microwave frequency is different at each point so as to be resonant with the difference in AC Stark shifts at each point. The maximum probability of a transition is achieved near the turning points of the oscillation, but unfortunately in that case $2P_{LZ}(1 - P_{LZ})$ approaches zero, and no atoms return to the bottom of the well in the $|b>$ state. Within a few Ω_{eff} of the turning point, it is unclear if decoherence will permit transitions to the $|b>$ state to occur at the turning point. If not, the Raman lasers may have to be pulsed on and off so that the transition is no longer adiabatic. The majority of calculations in this Chapter are made assuming a large population transfer at the turning points. Then in Section 6.2.7, modifications brought about by a pulsed scheme will be discussed.

To select the optimum detuning and intensity, it is helpful to examine some general scaling issues. Heating rates are minimized when the spontaneous scattering rate $\Gamma_{\rm sc}$ is unsaturated, Δ must be large and $\Gamma_{sc} \propto I_t/\Delta^2$ [see Eq. (5.2)]. However, two

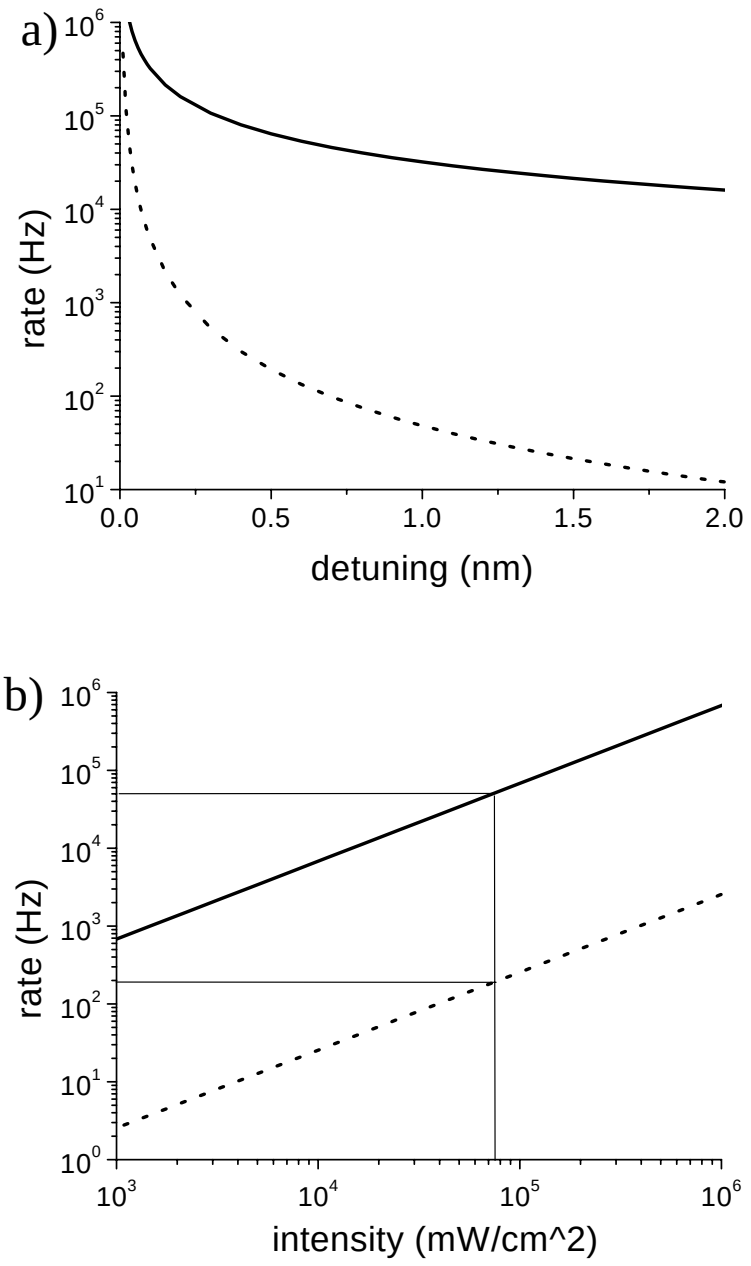

Figure 6.2: Effective Rabi frequency/(2π) (solid curve) for the two-photon stimulated Raman transition (a) versus the laser detuning for total intensity $I_t = 1.18 \times 10^5$ mW/cm^2 and (b) versus the laser intensity at a fixed detuning of 0.4 nm. Broken curves represent the spontaneous photon scattering rate of atoms in the FORT due to the Raman laser beam. The intensities describe typical experimental conditions. Therefore, $I_t = I_1 + 2I_2$, and the intensity of second frequency component $I_2 = \frac{1}{2}I_1$, where I_t is used to calculate the spontaneous rate and $\sqrt{I_1 I_2} = I_t/\sqrt{8}$ for calculation of the Rabi frequency.

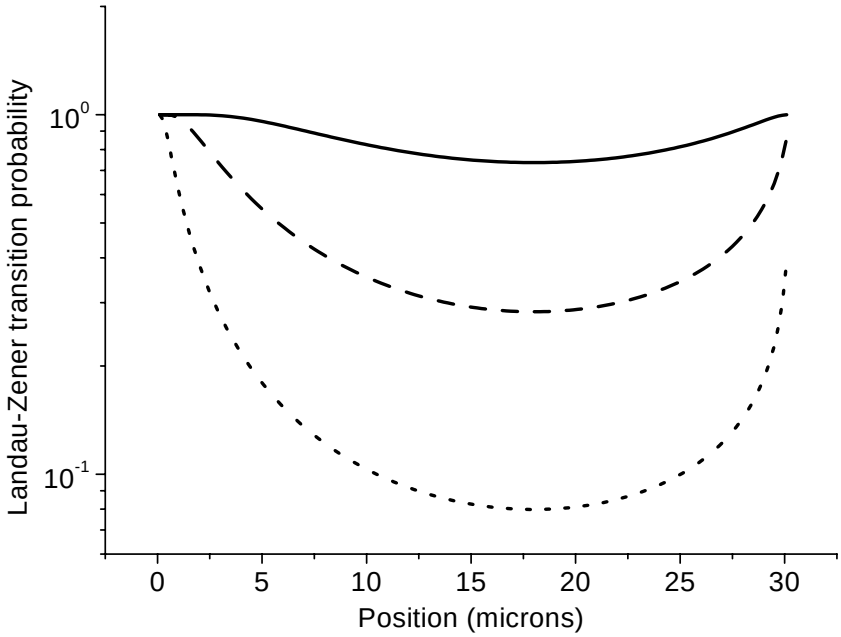

Figure 6.3: Landau-Zener transition probability as a function of position in the circular FORT for 1 atom oscillating in the FORT potential, with a maximum amplitude ρ_{max} of 30 μm. The microwave frequency is different at each position so as to be resonant with the difference in AC Stark shifts at each point. I_t = 7.5×10^4 mW/cm^2 (solid), 3.8×10^4 mW/cm^2 (dashed), and 1.9×10^4 mW/cm^2 (dotted).

different regimes must be considered for the Landau-Zener probability. Often, two photon Raman transitions can be employed with high Rabi frequencies and long interaction times. In this case, the Landau-Zener model no longer applies and atoms can undergo as much as a π-pulse. The time t_π required for a π-pulse scales as $1/\Omega_{eff} \sim \Delta/I_t$, and therefore the ratio of two-photon transition rate to spontaneous scattering rate is proportional to Δ. This scaling also applies to the Landau-Zener transitions when Γ_{LZ} approaches 1. However, when atoms are resonant with the drive frequency for a small fraction of the Rabi oscillation period, Γ_{LZ} is small. Then $P_{LZ} \propto \Omega_{eff}^2 \sim I_t^2/\Delta^2$. Therefore the ratio of Landau-Zener transition rate to spontaneous scattering rate goes with I_t. To demonstrate the Raman transitions, we operate in the small Γ_{LZ} regime. Thus high intensities are critical for observing Raman transitions due to the Raman laser over the background due to spontaneous scattering of the laser.

However, to drive both forced evaporative cooling and Sisyphus cooling, it is important that the microwave frequency stay resonant with atoms near the turning points, where Γ_{LZ} is not small and therefore the first scaling characteristics apply. Thus as atoms are removed from the largest ρ values, the frequency must be decreased in order to interact with atoms at slightly lower energies. The fastest the frequency can be swept and still interact with all atoms is the width of the oscillation every quarter-period of oscillation $\tau_{\rm osc}/4$. The width of the resonance is approximately $\Omega_{\rm eff}$. To cool all the

atoms, the drive frequency must vary at a rate not to exceed $(\Omega_{\text{eff}}/\tau_{\text{osc}})$, and it must interact with atoms at each AC Stark shift. Therefore the duration of the fastest sweep that cools each atom is then the potential depth in MHz divided by the sweep rate in MHz/s. The number of photons spontaneously scattered during this time then scales with ratio of the scattering rate to the Rabi frequency, $\propto 1/\Delta$. Thus the number of photons scattered during an optimized sweep is independent of the Raman laser intensity, assuming there is enough intensity to prevent the Landau-Zener approximation from breaking down.

6.2.2 Repumping with Spontaneous Scattering

Repumping is also an important part of the cooling cycle. For the cycle to be irreversible, it must involve a spontaneous transition. For the cycle to remove any energy, the repumping must occur at smaller differential Stark shifts than the drive transition does. For the circular FORT potentials, the amount of energy extracted per cycle depends on the initial energy E_i, where E_i is the total energy of the atom with respect to the energy of the bottom of the trapping potential U_0.

$$\frac{\Delta E(E_{\text{i}},\rho)}{E_{\text{i}}} = (1-\frac{U_b}{U_a})(1-(\frac{\rho}{\rho_{\max}})^2),$$

The turning point of the atom's oscillation $\rho_{\max}$ can be found by solving Eq. 4.1 for ρ:

$$\rho_{\max}(E_{\text{i}}) = w_0\sqrt{\ln(1-\frac{E_{\text{i}}}{U_0})/-2}. \tag{6.4}$$

The probability that an atom is repumped at a particular ρ depends on the time interval $dt(\rho)$ that it spends at a particular ρ, and $dt(\rho)$ is given by energy conservation

$$dt(\rho) = d\rho[\frac{2}{m}U_b(e^{-2\rho_{\max}^2/w_0^2}-e^{-2\rho^2/w_0^2})]^{-\frac{1}{2}},$$

where m is the mass of the Rb atom [99].

Because the detuning and intensity can vary with position, the photon scattering rate Γ_{sc} described in Eq. (5.2) also acquires a ρ dependence. When the FORT light is used as the repump, the detuning Δ is so large that it is essentially uniform across the trap and the rate just depends on the local intensity. In that case,

$$\Gamma_{\text{sc}}^{\text{int}} = Ge^{-2\rho^2/w_0^2},$$

where G is an arbitrary constant.

An additional circularly polarized laser tuned close to resonance with the $P_{1/2}$ or $P_{3/2}$ can be added to perform the repumping. Even when it is not focused, selectivity is still provided by the spatial dependence of the detuning provided by the AC Stark shift.

$$\Gamma_{\text{sc}}^{\text{det}}(\rho) = \frac{\Gamma^2}{\Gamma^2+4[\delta+\frac{U_0}{h}(1-e^{-2\rho^2/w_0^2})]^2}$$

Table 6.1: Repumping from the $|2,+1>$ state. Tabulated are the percent probabilities that an atom decays from the excited state listed across the top to the ground state listed on the left side. These excited states are accessible with a Δm = +1 transition from the $|2,+1>$ state. Based on calculations by Christopher J. Myatt.

	$5\ ^2P_{3/2}$		$5\ ^2P_{1/2}$	
	$\|3',+2>$	$\|2',+2>$	$\|3',+2>$	$\|2',+2>$
$\|3,+3>$	14	16	11	56
$\|3,+2>$	19	5	15	19
$\|3,+1>$	23	1	19	4
$\|2,+2>$	15	52	19	15
$\|2,+1>$	30	26	37	7

where w_0 is the FORT laser beam waist, the P state linewidth Γ = 6 MHz, and δ = detuning of the laser from the AC Stark-shifted atoms at the bottom of the trap. The optimum $\delta = \Gamma/2$ for maximum selectivity.

The average fractional energy change per cooling cycle α can then be computed as a function of the atom's initial energy $E_{\rm i}$:

$$\alpha = < \frac{\Delta E(E_{\rm i})}{E_{\rm i}} > = \frac{\int_{\rho=0}^{\rho_{\max}} dt(\rho)\,\Gamma_{\rm sc}(\rho)\,\frac{\Delta E(E_{\rm i},\rho)}{E_{\rm i}}}{\int_{\rho=0}^{\rho_{\max}} dt(\rho)\,\Gamma_{\rm sc}(\rho)}, \tag{6.5}$$

where $\rho_{\max}$ is a function of $E_{\rm i}$ as in Eq. (6.4). The result of this integral as a function of initial energy for both rf and microwave drives, as well as both types of repump transitions, is plotted in Fig. 6.4. From this plot, it is clear that the microwave drive connecting $|3,+3>$ and $|2,+1>$ can remove much more energy per cycle than the rf scheme connecting to $|3,+2>$. In addition, the spatial selectivity of the repumping is not essential for removing energy, as shown by curves 2 and 6. Finally, an optical repumping technique can provide spatial selectivity using detuning. This technique works best when U_b is large compared with the linewidth of the repumping transition, as in curve 3 of Fig. 6.4.

Another large influence on the effectiveness of the repump is the probability that an atom spontaneously decays to the $|3,+3>$ state after being repumped. This depends on quantum numbers of the initial state $|b>$, the polarization of the repumping photon (always σ_+), and the excited state. Examination of the appropriate Clebsch-Gordon coefficients tabulated in Table 6.1 and Table 6.2 reveals some important distinctions between repumping schemes.

The RF cooling scheme excites atoms to the $|3,+2>$ from which they need to be repumped. The circularly polarized FORT laser can do this quite effectively. When it is tuned close to the D_2 transition, 84% of the absorbed photons excite atoms to the $|4',3>$ state. Of these, Table 6.1 shows that 1/4 decay to the $|3,+3>$ state, while 3/4 decay back to the $|3,+2>$ state in which they started. They then have another chance to make it back to the $|3,+3>$ state while being penalized only 1 photon recoil. Averaging over all transitions, this cycle is 92% closed.

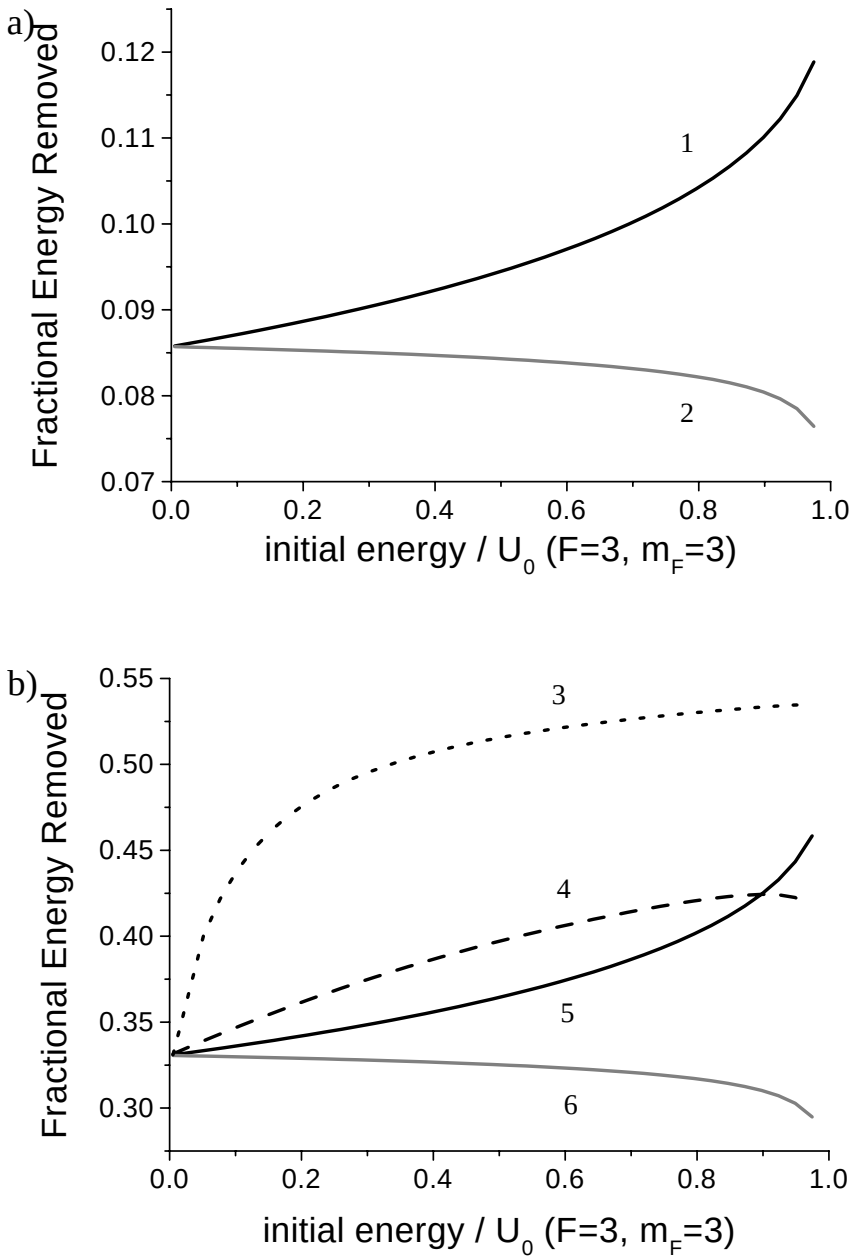

Figure 6.4: Evaluation of Eq. (6.5) as a function of initial energy, for various repumping schemes. **(a)** For $|a>= |3,+3>$ and $|b>= |3,+2>$ as in the rf cooling scheme depicted in Fig. 6.1 (a). **(b)** shows the cooling efficiency for $|a>= |3,+3>$ and $|b>= |2,+1>$ the scheme depicted in Fig. 6.1 (b). Curves 1 and 5 represent repumping by the FORT as described by $\Gamma_{\rm sc}^{\rm int}(\rho)$. Curves 2 and 6 show that energy can still be extracted when no spatial dependence of the repump scattering rate is employed, i.e. when $\Gamma_{\rm sc} = 1$. When repumping is done with an additional repump laser, $\Gamma_{\rm sc}^{\rm det}(\rho)$ is used in the integral. Curve 4 is shown for $U_0(a)$ = -1 mK, and curve 3 for $U_0(a)$ = -10 mK.

Table 6.2: Repumping from the $|3,+2>$ state. Tabulated are the percent probabilities that an atom decays from the excited state listed across the top to the ground state listed on the left side. These excited states are accessible with a Δm = +1 transition from the $|3,+2>$ state. Based on calculations by Christopher J. Myatt.

	$5\ ^2P_{3/2}$		$5\ ^2P_{1/2}$
	$\|4',+3>$	$\|3',+3>$	$\|3',+3>$
$\|3,+3>$	25	42	33
$\|3,+2>$	75	14	11
$\|2,+2>$	0	44	55

The circular FORT is not as effective when repumping atoms from the $|2,+1>$ state, where they are driven in the microwave cooling scheme. If the FORT is closest to the D_2 transition, an average over the appropriate Clebsch-Gordon probabilities indicates that only 15% of the repumping transitions return the atoms to the $|3,+3>$ state to complete a closed cycle. 28% return the atoms to the $|2,1>$ state, and again no net cooling results. Unfortunately, 34% return to the shallowest $|2,+2>$ state from which they are most likely lost before they can be pumped to the $|3,+3>$ state.

In contrast, an additional circularly polarized repump laser tuned from the $5\ ^2S_{1/2}$ $|2,+1>$ to the $5\ ^2P_{1/2}$ $|2',+2>$ state should be much more efficient. As shown in Table 6.2, 56% of the repump transitions result in a closed cycle. For this additional laser to dominate the repumping process, the scattering rate of atoms in the $|2,+1>$ state must be several times higher than the FORT. However, this will not cause significant additional heating because the vast majority of atoms are in the $|3,+3>$ state where they are detuned several GHz from resonance with the additional repump laser.

6.2.3 Cooling Rates

Once the efficiency of the cooling process is understood, the maximum cooling rate is readily calculated. Because the Landau-Zener probability is very high at the turning points of the oscillation, after half an oscillation period no more atoms will be resonant with the drive frequency, because they will either be cooled or lost. Therefore, to continue cooling, the microwave or rf drive frequency must increase so as to interact with atoms of lower kinetic energy. As described in the previous subsection, the optimum rate at which to sweep the frequency ν is

$$\frac{d\nu}{dt} = \frac{4}{\tau_{\rm osc}} \frac{\Omega_{eff}}{2\pi} \tag{6.6}$$

where $\tau_a^{\rm osc}$ is the period of oscillation of atoms in the deeper of the two circular FORT potentials involved in the cooling cycle.

The maximum cooling rate is the ratio of the amount of energy carried away in one cooling event to the time between cooling events. As plotted in Fig. 6.4, the fraction (α) of energy removed in one cooling cycle depends on the initial energy E_i;

$\Delta E = -\alpha E_i$. The time between events Δt, for a constant frequency sweep, also depends on the initial energy. The more energy an atom gives up in one cooling event, the longer it must wait before the drive frequency is resonant with its turning point again and it can experience another cooling cycle.

$$\Delta t = \frac{\Delta E}{h}(\frac{d\nu}{dt})^{-1}.$$

The resulting cooling rate is surprisingly constant in time, independent of the atom's energy:

$$\frac{dE}{dt} = \frac{4\Omega_{eff}\hbar}{\tau_a^{\rm osc}} \tag{6.7}$$

This calculation must break down when the time for an atom to be repumped (t_R) exceeds Δt above. In essence, that means that the atoms can no longer keep up with the sweep rate of the drive frequency. If t_R is limited by the time required for the atom to oscillate back to the center of the trap, then $t_R = 1/4\tau_b^{\rm osc}$, where $\tau_b^{\rm osc}$ is the period of oscillation in the shallow potential. Cooling then crosses into a different regime, in which the sweep rate is limited so that the atom is repumped before the drive comes into resonance with the frequency of the new turning point of the atom. This gives an exponentially decreasing cooling rate:

$$\frac{dE}{dt} = -\alpha E \frac{4}{\tau_b^{\rm osc}} \tag{6.8}$$

and a resulting time-dependent energy of

$$E(t) = E_{\rm i} e^{-4\alpha t/\tau_b^{\rm osc}}. \tag{6.9}$$

For typical experimental parameters of Ω_{eff} = 2π 50 kHz and $\tau_a^{\rm osc}$ = 1 ms, dE/dt = 10 mK/s. The energy (E_t) at which the expression for dE/dt changes from a constant to an energy-dependent expression is then $E_i = \Omega_{eff}\hbar\tau_b^{\rm osc}/\alpha\tau_a^{\rm osc}$. For the values above, $\tau_b^{\rm osc} = 2$ ms, and α = 0.3, E_B/k_B = 17 μK.

6.2.4 Evaporative Cooling

Forced evaporative cooling is also a powerful technique that can be highly efficient in the limit of rapid collisions and long lifetimes. The speed with which the potential depth can be reduced and hence the cooling can be driven depends on the collision rate of the atoms. Because the circular FORT has much tighter confinement and higher collision rates, evaporation can proceed at much faster rates in this trap than in magnetic traps. For the best evaporative cooling configuration, one should operate the trap at a wavelength in which the $|b>$ state is unbound. This is the case for $|2,1>$ state between 786 nm and 795 nm.

6.2.5 Heating Mechanisms

A variety of heating mechanisms can limit the performance of both Sisyphus and evaporative cooling. The heating due to collisions with background gasses is predicted by Beijerinck to be a modest 12 μK/s [17] in a 1 mK trap with a collisionally limited lifetime of 10 s.

Larger contributions come from simple photon scattering in the circular FORT. Even with perfect polarization, each photon absorbed on the cycling transition ($|3,+3> \rightarrow |4',+4>$) gives a recoil kick. The heating rate due to this process is a simple random walk in momentum space. The resulting heating rate is

$$\frac{dT}{dt} = \frac{\Gamma_{sc}}{3}\frac{v_R^2 m}{k_B}$$

where v_R is the recoil velocity (0.5 cm/s in Rb), m is the atomic mass, and k_B is Boltzman's constant. Conveniently in Rb, for T in μK and v in cm/s, $m/k_B \approx 1$. Typical experimental parameters give 500 photons/s absorbed and spontaneously scattered from the FORT laser beam, and therefore a heating rate of 40 μK/s.

The FORT atoms will also absorb photons from the Raman laser beams, and because these are not circularly polarized, they tend to randomize the m_F states. The resulting dipole force fluctuations can give rise to large heating rates, as shown in Chapt. 4, Fig. 4.7. In that chapter, an expression was derived for the exponential lifetime as a function of initial and final temperatures and the depths of the potentials involved. Using the same arguments, a heating rate can be directly derived. The resulting expression for energy as a function of time becomes:

$$E(t) = E_i e^{\frac{U_a}{U_b}\Gamma_h t} \tag{6.10}$$

where Γ_h is defined previously as the hopping rate between potentials. The resulting 1/e time constant is then $[\frac{U_a}{U_b}\Gamma_h]^{-1}$

For the Raman lasers detuned 0.4 nm, typical experimental parameters give 200 photon/s scattering rates and therefore $\Gamma_h \approx 10$/s. The derivative of Eq. 6.10 evaluated for an initial energy of 0.4 mK gives a large initial heating rate of 4 mK/s, nearly equal to the cooling rate.

Imperfect FORT polarization can still contribute to heating in the same way described in Chapt. 4. Therefore, the FORT laser polarization must be carefully controlled to keep the dipole force fluctuation heating from limiting the cooling.

Often, radiation trapping is cited as a limit to effective optical cooling schemes. This should not limit the performance of the schemes proposed here, because the FORT photons are very far from resonance, and therefore unlikely to be reabsorbed as they exit the atom cloud. Even the addition of a repump at 795 nm will not cause additional heating, because it is several GHz detuned from the majority of atoms in the trap.

6.2.6 Ultimate Temperatures

The limits of the optimized Sisyphus cooling process are found by examining the balance between the heating and cooling rates. The largest heating rate calculated

in the preceding section is caused by dipole force fluctuations induced by spontaneous scattering of photons from the Raman laser. However, this heating rate decreases with temperature, whereas the Sisyphus cooling rate is independent of temperature above about 20 μK. Therefore, if the temperature is low enough to start the cooling process, this heating rate can only affect the Sisyphus cooling below the crossover temperature, where Sisyphus cooling starts to turn off. In that case, the differential equation that describes the competition between heating and cooling is simply

$$\frac{dE}{dt} = (-\alpha \frac{4}{\tau_b^{\rm osc}} + \Gamma_h \frac{U_a}{U_b})E.$$

For the parameters given in the previous section, the cooling term outweighs the heating by a factor of 15, and therefore this heating mechanism does not greatly impact the Sisyphus cooling rate.

Recoil heating due to FORT scattering of 40 μK/s does not limit the final temperature. Because this heating rate is independent of the atom's energy, and less than the constant cooling rate of 10 mK/s, this cannot limit the final temperature until the cooling turns off in the exponential regime. By setting the magnitudes of the cooling and heating rates equal to one another as above, the limiting temperature is 70 nK. Therefore, this heating rate will not limit the final temperature of the atoms, as this is far below the recoil limit of the cooling process. The constant heating rate due to background collisions of 12 μK/s should also not limit the final temperature, as that heating rate balances the cooling rate at an even lower temperature: 20 nK.

Finally, the cooling process itself causes some recoil heating, due to the spontaneous emission of photons in all directions. If a few repumping events are on average required to close the cooling cycle, the final temperature is about 250 nK. Thus the recoil limit seems to be the ultimate cooling limit of the Sisyphus process.

The above limits were established under the assumption of ideal repumping. If the cooling cycle is only 92% closed, then about 10% of the atoms are lost during each cooling event, and the number of atoms left after j cooling cycles will be $0.9^{\rm j}$. Thus to cool atoms a factor of 10 with α = 0.3, cooling a factor of 10 results in a loss of 50% of the atoms. Even this loss should turn off as the atoms get colder, because atoms will no longer be lost from the very shallow $|2, +2>$ state. Of course, as temperatures decrease, densities increase and therefore collisional losses will increase. Increased losses are not calculated in this document, but will undoubtedly be important.

6.2.7 Cooling with a Pulsed Drive

As mentioned on page 74, it may not be possible to drive transitions between $|a>$ and $|b>$ continuously due to the adiabatic interaction of the atoms with the drive frequency. In this case, a pulsed implementation similar to that used in gravitational Sisyphus cooling may be necessary. To do this in the circular FORT, the MOPA drive is turned on for about 1/4 $\tau_a^{\rm osc}$ in order to induce Rabi flopping between $|a>$ and $|b>$ that results in 50% of the population in each state. Then 1/4 $\tau_a^{\rm osc}$ later, if the repumping is induced by an additional laser, the repump laser should be turned on for an additional

1/4 $\tau_a^{\rm osc}$. This cycle should then be repeated every 3/4 $\tau_a^{\rm osc}$ so that the drive can interact with atoms in every phase of oscillation. Therefore the optimum sweep rate is a factor of 3 slower than that given by Eq. (6.6) and therefore so is the optimum cooling rate [Eq. (6.7)] from 10 mK/s to 3 mK/s.

One of the heating rates scale with the time that the Raman laser beams illuminate the trapped sample, specifically the dipole force fluctuation heating induced by the spontaneous scattering of Raman laser light as described on pg. 82. The reduced duty cycle of the Raman lasers changes the heating from 4 mK/s to 1.3 mK/s. The other heating rates are not reduced with the Raman laser duty cycle. Therefore the temperatures at which the cooling and heating balance will increase by up to a factor of 3. Fortunately the final temperature appears to be limited by the recoil heating due to spontaneous emission during the cooling cycle, which remains the same as previously estimated.

6.3 Experimental Implementation

6.3.1 RF considerations

To implement the Sisyphus cooling scheme, we first explored the rf drive. We attempted to couple rf into the vacuum chamber by placing a drive coil about 2 in. dia. on a 6 in. flange (4 in. clear aperture window), and drove it at frequencies between 1 and 10 MHz. Unfortunately, the stainless steel vacuum chamber is an excellent shield of rf. To quantify that statement, we measured the voltage across a pick-up coil as a function of the distance between the pick-up coil and the source coil, in free space and in the presence of a 4 in. dia. pipe, mimicking our vacuum chamber. The results, shown in Fig. 6.5, indicate that the rf that reaches the atoms at about 16 cm from the coil is suppressed by 3 orders of magnitude in amplitude, and therefore 6 orders of magnitude in power. Consequently, we concluded that the only way to couple rf into our vacuum chamber is to break vacuum and insert a coil very close to the atoms.

6.3.2 MOPA

Rather than open the vacuum chamber, we chose to pursue the two-photon stimulated Raman transition option. This was made easier by the existence of a microwave-modulated master oscillator power amplifier MOPA system already constructed by Neil Claussen. A typical MOPA system [100] consists of a grating-tuned diode laser injected into a tapered amplifier. Multiple diode laser beams at different frequencies can also be injected into the amplifiers [101]. Our MOPA relies on microwave modulation [96] to create 2 frequencies in the master oscillator (MO) diode laser. The length of the cavity is chosen to be resonant with the modulation frequency, so that large modulation depths are achieved with small injected powers. Typically two frequency sidebands are created with powers up to about 50% of the power remaining in the carrier, and 25% of the initial power in each sideband.

The output from the MO is then tightly focused and mode-matched into the power amplifier (PA) that is driven at between 1.5 and 1.8 Amps. The output from the PA

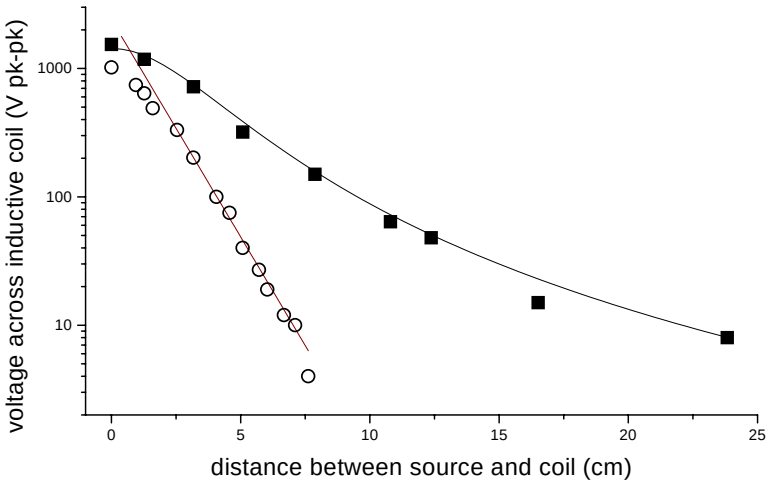

Figure 6.5: Demonstration of the difficulty of coupling rf (frequency = 3.7 MHz) radiation into a vacuum chamber from outside. In free space (■), the field detected by an inductive coil decreases as $1/r^3$. However, when the rf radiation must propagate along the axis of a metal cylinder (dia. = 4 in) (◯), the field decays with a e^{-1} length of 1.3 cm.

contains all the frequency components from the MO. Unfortunately, as discussed in detail in Ref. [100], the output from the PA also contains a lot of broadband radiation spread over 20 - 30 nm. The power density of this radiation decreases by more than an order of magnitude when the MO is injected into the PA, making it about 1.5% of the power at the amplified frequency per 0.1 nm [100]. If the MOPA is focused to a total intensity of 1.5×10^5 mW/cm^2, the amount of intensity within a linewidth of the Rb resonance is about 3.4×10^{-4} mW/cm^2, resulting in a scattering rate of 2.5 $\times 10^3$ photons per s, which is larger than the scattering due to the amplified power at the desired wavelength by a factor of 10 when the MO is tuned 0.5 nm from resonance. The effect of the scattering induced by the broad-band power emitted from the PA was clearly observable. The lifetime of FORT atoms in the presence of the MOPA light decreased from 7 s to 200 ms at MOPA total intensities as small as 10^4 mW/cm^2.

This broad-band radiation is difficult to filter out using conventional filters, because we want to block broadband radiation on resonance with the atoms, but completely pass the amplified power about 0.5 nm away. Typical interference filters do not have narrow enough bandpass widths or sharp enough cut-offs for this application. Fabry-Perot cavities might be made to work, but would require a lot of effort. Therefore, the most logical filter is an absorption cell of the appropriate species, in this case Rb. Therefore, a Rb cell was placed in the MOPA beam path and heated such that the coldest point in the cell is about 55^0C, giving a vapor pressure of 6 $\times 10^{-6}$ Torr, 30 times that of room temperature. The effect of broadband MOPA light on the FORT

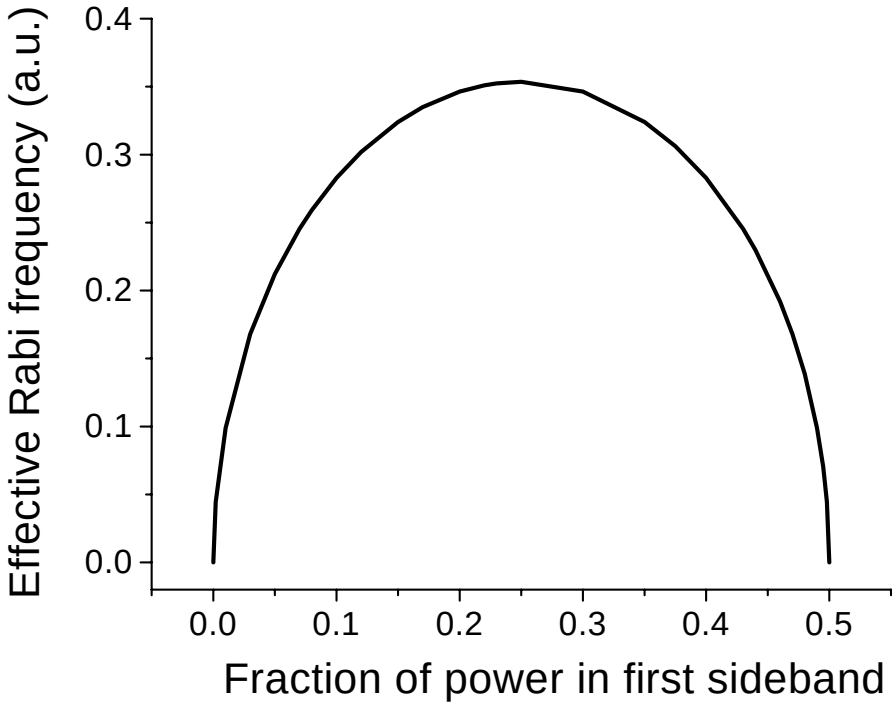

Figure 6.6: Calculated relative Rabi Frequency vs. the efficiency of MOPA modulation. The MOPA modulation is defined as the ratio of the power in one sideband over the power at the carrier frequency, assuming the power is equal between the +1 and -1 order modulation peaks.

lifetime became much less significant. Without any injected light, the lifetime of the atoms changes only about 10% when illuminated by the PA broadband radiation under conditions in which the maximum MOPA intensity is a total of 10^5 mW/cm^2.

The optimum modulation amplitude of the MOPA light in order to drive two-photon Raman transitions is readily calculated. Because both sidebands are equally populated, but the transition is driven by an interference between one sideband and the carrier, over-modulation can deplete the carrier and reduce the transition rate. Thus the optimum requires that half the power remain in the carrier and 25% in each sideband. However, it is not a steep function, so the requirements on modulation are not stringent, as shown in Fig.6.6.

6.3.3 Procedure

A schematic of the experiment is shown in Fig. 6.7. The procedure is very similar to that described in Chapter 4. Primary differences include the absence of a repump beam to help with loading. Also, we have the capability to image the atoms

as in Chapter 5. Thus we are able to measure the temperature of the atoms in ballistic expansion as the atoms are cooled with the MOPA laser beam. Finally, we include the MOPA laser, focused to 1.5 $\times 10^5$ mW/cm^2, counterpropagating the FORT laser. This choice of geometry allows the highest intensities for driving the two-photon transitions, but only allows Δm = -2 transitions. Therefore state $|b>$ in the cooling scheme must be $|2,+1>$ because $|2,+2>$ is inaccessible, although it would provide slightly higher values of α. Thus with an infinite intensity, directing the MOPA beams perpendicular to the FORT may be preferable. The MO is modulated at frequencies near 3035 MHz, as described above. We have the capability to trigger a ramp of that frequency, linear to within about 10%, with control over the ramp rate, duration, beginning and ending frequencies.

6.4 Preliminary results

6.4.1 Two-Photon Stimulated Raman Transitions

To verify that the MOPA laser could actually excite two-photon stimulated Raman transitions, we monitored the number of atoms stored in the FORT for a fixed FORT storage time while the MOPA illuminated the atoms for the majority of that time. The frequency of the modulation was changed from shot to shot, and the number remaining in the trap was monitored. The resulting loss is shown in Fig. 6.8. This plot presents many interesting features that give information about the internal states and kinetic energies of atoms in the FORT and the depth of the FORT. No transitions occur blue of the 3035 MHz Rb resonance, implying that no atoms are being driven to deeper potentials, only shallower ones. This is a weak indication of the spin-polarization we measured previously in Chapter 6. The depth of the potential can be measured by the shift of the steep edge. This occurs 35 MHz red of the Rb unshifted resonance, implying a 50 MHz AC stark shift at the bottom of the $|3,3>$ potential, or 2.5 mK. Calculated values for this trap are 1 mK, assuming $w_0 = 60$ μm This value decreased the next day by 10 MHz, and these are the conditions under which the remaining data were taken.

6.4.2 Cooling with Stationary Frequency

Figure 6.9 shows observed temperature as a function of time, for the frequency fixed at a detuning of 22.5 MHz below the Rb resonance. During the cooling, the number of atoms in the FORT decreased between a factor of 20 and 50. The uncertainty arises because the peak optical depth after expansion is monitored, but not the total number. The conversion of the peak optical depth relies on knowledge of the scaling of the length of the FORT. In (b), ■ are calculated assuming the longitudinal dimension does not contract and is therefore not in thermal equilibrium with the other dimensions, while ◯ show N assuming thermal equilibrium in all 3 dimensions. Finally, phase space density is computed assuming the sample is in thermal equilibrium, and is seen to increase by a factor of about 15.

The mechanism here is most likely primarily evaporative. Because the frequency is not changing with time, most atoms are not excited at the turning point of their

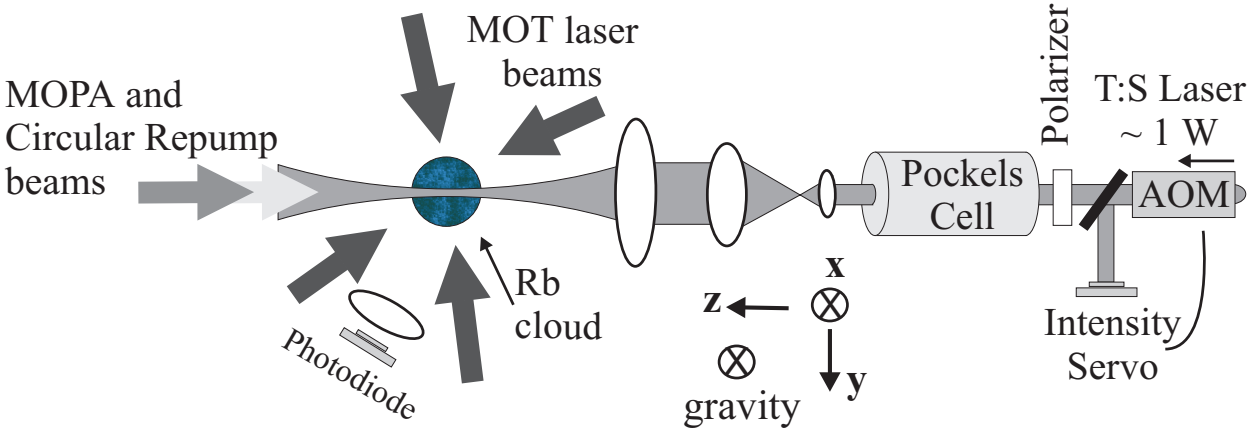

Figure 6.7: Layout of the all-optical two-photon stimulated Raman cooling scheme. Primary differences between this and Fig. 4.4 include the addition of a MOPA laser beam counter-propagating the FORT. The additional repump shown to counter-propagate the FORT laser beam is only proposed, and has not yet been implemented.

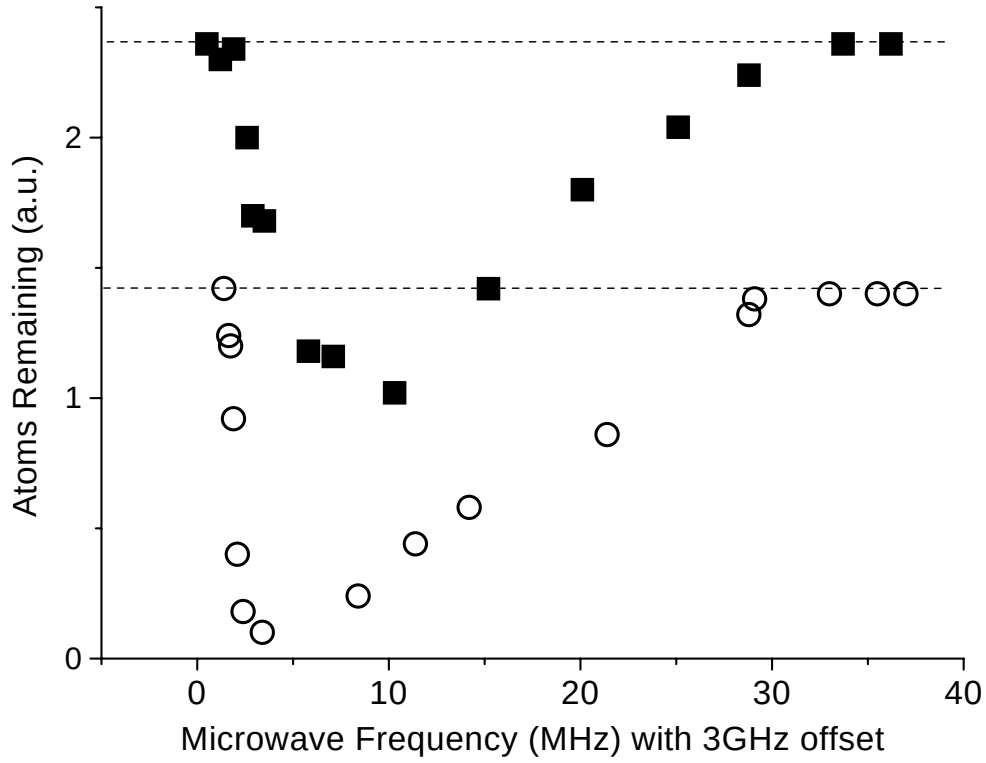

Figure 6.8: Loss from the circular FORT due do ground-state changing transitions as a function of the microwave frequency driving the transition. The resonance frequency for atoms in free space is 3035 MHz. (■) represent a FORT storage time of 250 ms and a cooling duration of 150 ms, while (◯) show the same data for a longer FORT storage time (500 ms) and a longer cooling duration of 480 ms. Because at longer times the signal drops all the way to zero, the shape of the curve is distorted and the slope of the curve near the bottom of the trap goes to zero.

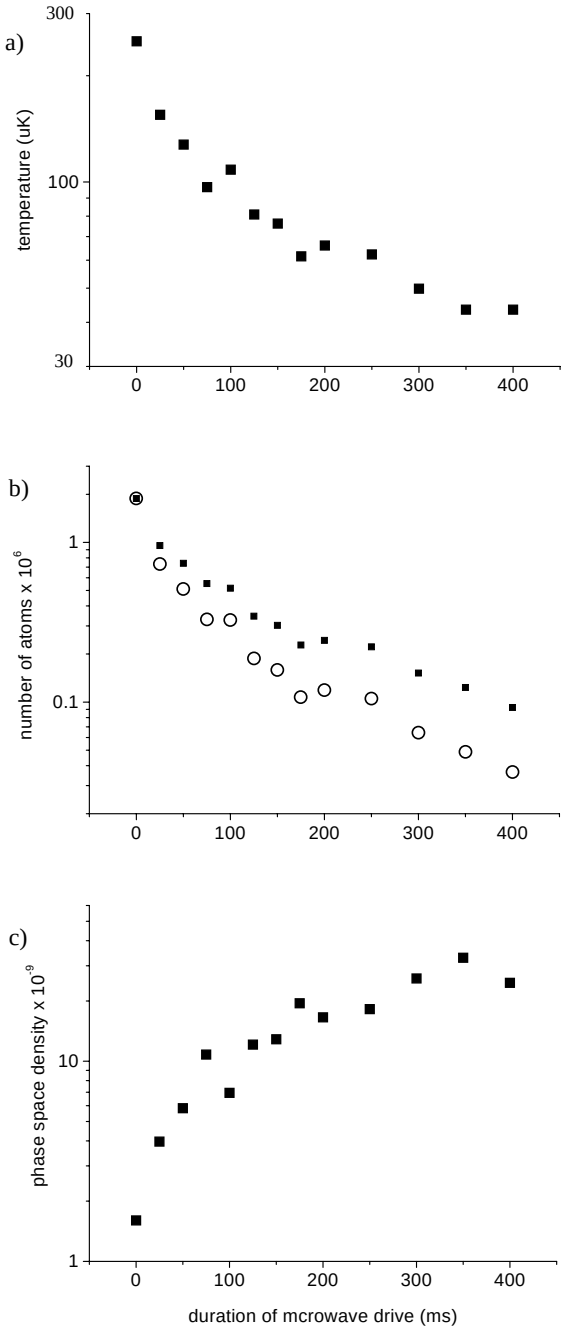

Figure 6.9: While the microwave drive frequency was held fixed at 3012.5 MHz, the time during which it was applied was varied simultaneously with the FORT storage time. (a) Shows the change in temperature, (b) number, and (c) the deduced phase space density, assuming the cloud remains in thermal equilibrium. In b), (■)'s represent the number left assuming the longitudinal dimension of the trapped sample does not change and (◯)'s represent the number assuming all dimensions are in thermal equilibrium.

oscillation. Instead they are excited to state $|b>$ with large kinetic energies, from which they are lost. However, at very low temperatures, this mechanism must turn off because all states in the circular FORT are trapped (ie. $U_0 < 0$) . Perhaps this is the cause of the turnoff in cooling, along with substantial number loss.

6.4.3 Cooling with Swept Microwave Frequency

Once two-photon Raman transitions were demonstrated and cooling was demonstrated at a fixed frequency, cooling with a swept drive frequency was demonstrated. The frequency ramp began at the unshifted resonance of the ground-state splitting, and was swept at a constant rate for a variable time. Therefore the duration of the sweep also represents a "deeper cut" into the cloud, or allows interactions with increasingly colder atoms. The results are shown in Fig. 6.10. Phase space density increases by a factor of 5. In addition, the number loss is about a factor of 7.5, which could be ascribed to inefficient evaporation. At the lowest temperatures, however, evaporation seems unlikely because all states in the circular FORT are trapped at this wavelength. Thus additional losses are again likely to be due to collisional losses caused by increased density.

A comparison of the cooling results is at first glance perplexing. The fixed frequency data gives lower temperatures (30 μK vs. 80 μK), and higher phase space density increase (factor of 10 vs. factor of 5). Even in reaching 80 μK, the fixed frequency cooling gave comparable number loss and slightly higher (factor of 1.5) phase space density increase. Perhaps the fixed frequency cooling is initiating an evaporative cooling mechanism, while the swept frequency is poorly optimized for Sisyphus cooling. In both cases, the Sisyphus cooling may be turning off as the atoms get colder and the Landau-Zener transitions become increasingly adiabatic. Further study is warranted.

6.4.4 Heating Rates

Once cooling is shown to work, heating rates are easily measured by applying a cooling pulse and then watching the trapped sample heat up with time. As shown in Fig. 6.11, rates of 150 μK/s are measured in the circular FORT in the absence of any additional laser light. This rate is consistent with a 5-10 s lifetime in a 1 mK trap. The expected heating rate in this trap, calculated earlier, is only 46 μK/s. However, the FORT polarization is not likely to be perfectly circular, and additional dipole force fluctuation heating, in conjunction with the heating already described, can easily cause the higher measured rate.

6.5 Conclusion

Sisyphus cooling and forced evaporative cooling schemes are theoretically very powerful cooling mechanisms in the circular FORT. Sisyphus cooling rates of up to 10 mK/s are possible, and limiting temperatures approaching the recoil limit may be possible. Initial results show that the temperature can be reduced by a factor of 4 to 80 μK while the number decreases by only a factor of between 2 and 6. Significant

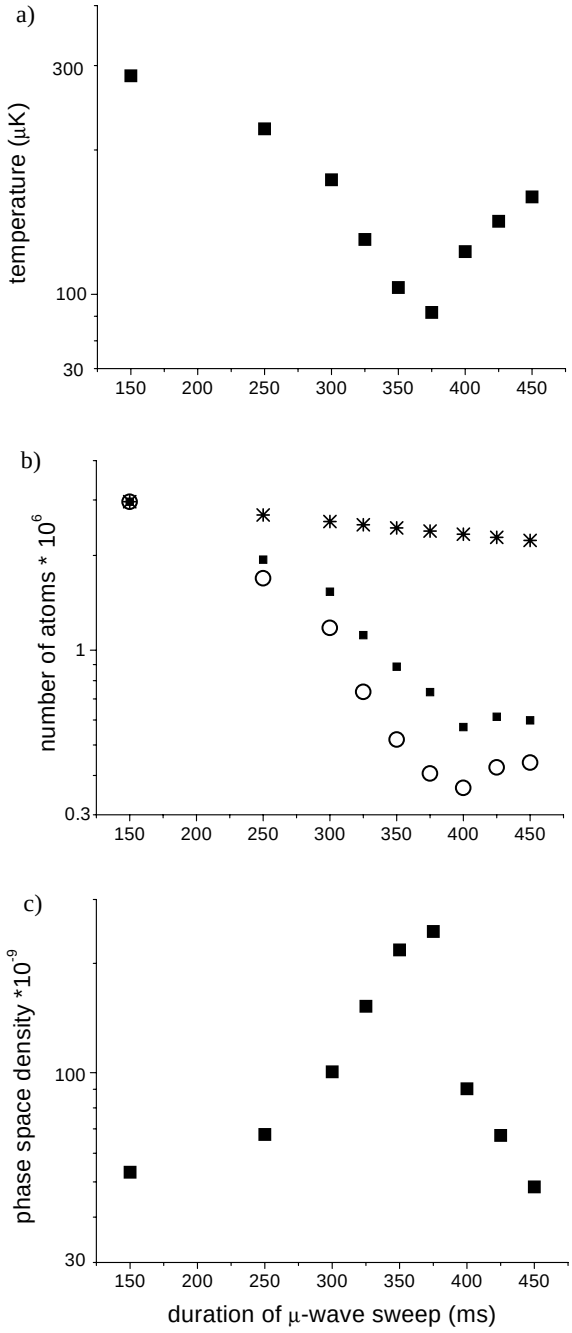

Figure 6.10: Atoms in the FORT are continually illuminated by the Raman beams while the microwave frequency was swept at a constant rate, starting from the unshifted resonance of 3035 MHz. As time increases, the end point of the sweep changes, effectively cutting deeper into the cloud. 150ms corresponds to a sweep of 9.8 MHz. Plotted are (a) the temperature of the atoms after cooling, (b) the number of atoms remaining after cooling, and (c) the resulting phase space density, assuming the sample is in thermal equilibrium. In b), (■)'s represent the number left assuming the longitudinal dimension of the trapped sample does not change, (◯)'s represent the number assuming all dimensions are in thermal equilibrium, and finally the (∗)'s show the time-dependence of atoms in the FORT during that time without any cooling.

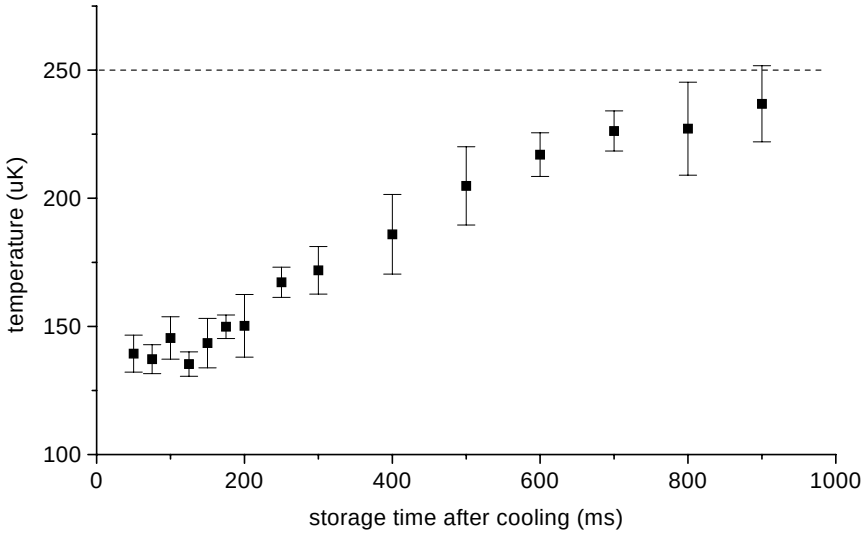

Figure 6.11: Heating rate of atoms stored in the circular FORT. Temperature is plotted as a function of time the atoms are stored in the FORT after a 50 ms cooling pulse is applied.

improvements in the Sisyphus contribution to this cooling scheme may be realized by utilizing an additional circularly polarized repump on the D_1 line, tailoring the frequency sweep to coincide with the optimum cooling rate, and pulsing the the MOPA on and off rapidly. Evaporation has not been optimized, and most likely the evaporative cooling effects could be improved significantly by tailoring the evaporation sweep rate as is done in magnetic traps. [67]

Bibliography

[1] M. H. Anderson, J. R. Ensher, M. R. Matthews, C. E. Wieman, and E. A. Cornell, "Observation of Bose-Einstein condensation in a dilute atomic vapor," Science **269,** 198–201 (1995).

[2] C. S. Wood, S. C. Bennett, D. Cho, B. P. Masterson, J. L. Roberts, C. E. Tanner, and C. E. Wieman, "Measurement of Parity Nonconservation and an Anapole Moment in Cesium," Science **275,** 1759–63 (1997).

[3] G. Gwinner, J. A. Behr, S. B. Cahn, A. Ghosh, L. A. Orozco, G. D. Sprouse, and F. Xu, "Magneto-optic trapping of radioactive ^{79}Rb," Phys. Rev. Lett. **72,** 3795–8 (1994).

[4] O. Stern and W. Gerlach, "Der experimentelle Nachweis des magnetischen Moments des Silberatoms," Z. Phys. **8,** 110–1 (1921).

[5] W. Gerlach and O. Stern, "Der experimentelle Nachweis der Richtungsquantelung im Magnetfeld," Z. Phys. **9,** 349–52 (1922).

[6] N. F. Ramsey, Molecular Beams (Clarendon Press, Oxford, 1956).

[7] W. D. Phillips and H. Metcalf, "Laser deceleration of an atomic beam," Phys. Rev. Lett. **48,** 596–9 (1982).

[8] W. Ertmer, R. Blatt, J. L. Hall, and M. Zhu, "Laser manipulation of atomic beam velocities: demonstration of stopped atoms and velocity reversal," Phys. Rev. Lett. **54,** 996 – 9 (1985).

[9] S. Chu, L. Hollberg, J. E. Bjorkholm, A. Cable, and A. Ashkin, "Three-dimensional viscous confinement and cooling of atoms by resonant radiation pressure," Phys. Rev. Lett. **55,** 48–51 (1985).

[10] J. P. Gordon and A. Ashkin, "Motion of atoms in a radiation trap," Phys. Rev. A **21,** 1606–17 (1980).

[11] P. D. Lett, R. N. Watts, C. I. Westbrook, W. D. Phillips, P. L. Gould, and H. J. Metcalf, "Observation of Atoms Laser Cooled below the Doppler Limit," Phys. Rev. Lett. **61,** 169–72 (1988).

[12] J. Dalibard and C. Cohen-Tannoudji, “Laser cooling below the Doppler limit by polarization gradients: simple theoretical models,” J. Opt. Soc. Am. B **6,** 2023–45 (1989).

[13] P. J. Ungar, D. S. Weiss, E. Riis, and S. Chu, “Optical molasses and multilevel atoms: theory,” J. Opt. Soc. Am. B **6,** 2058–71 (1989).

[14] E. L. Raab, M. Prentiss, A. Cable, S. Chu, and D. E. Pritchard, “Trapping of neutral sodium atoms with radiation pressure,” Phys. Rev. Lett. **59,** 2631–4 (1987).

[15] C. Monroe, W. Swann, H. Robinson, and C. Wieman, “Very cold trapped atoms in a vapor cell,” Phys. Rev. Lett. **65,** 1571 – 4 (1990).

[16] S. Bali, K. M. O’Hara, M. E. Gehm, S. R. Granade, and J. E. Thomas, “Quantum-diffractive background gas collisions in atom-trap heating and loss,” Phys. Rev. A **60,** R29 – 32 (1999).

[17] H. C. W. Beijerinck, “Rigorous calculation of heating in alkali traps by background gas collisions,” submitted to Phys. Rev. A .

[18] C. J. Myatt, N. R. Newbury, R. W. Ghrist, L. Loutzenhiser, and C. E. Wieman, “Multiply loaded magneto-optical trap,” Opt. Lett. **21,** 290 – 2 (1996).

[19] C. J. Myatt, E. A. Burt, R. W. Ghrist, E. A. Cornell, and C. E. Wieman, “Production of two overlapping Bose-Einstein condensates by sympathetic cooling,” Phys. Rev. Lett. **78,** 586–9 (1997).

[20] E. Riis, D. S. Weiss, K. A. Moler, and S. Chu, “Atom funnel for the production of a slow, high-density atomic beam,” Phys. Rev. Lett. **64,** 1658–61 (1990).

[21] J. Nellessen, J. Werner, and W. Ertmer, “Magneto-optical compression of a monoenergetic sodium atomic beam,” Opt. Comm. **78,** 300–308 (1990).

[22] A. Scholz, M. Christ, D. Doll, J. Ludwig, and W. Ertmer, “Magneto-optical preparation of a slow, cold and bright Ne^* atomic beam,” Opt. Comm. **111,** 155–62 (1994).

[23] J. Yu, J. Djemaa, P. Nosbaum, and P. Pillet, “Funnel with orientated Cs atoms,” Opt. Comm. **112,** 136–40 (1994).

[24] Z.-T. Lu, K. L. Corwin, M. J. Renn, M. H. Anderson, E. A. Cornell, and C. E. Wieman, “Low-Velocity Intense Source of Atoms from a Magneto-optical Trap,” Phys. Rev. Lett. **77,** 3331–4 (1996).

[25] C. Y. Park, M. S. Jun, and D. Cho, “Magneto-optical trap loaded from a low-velocity intense source,” J. Opt. Soc. Am. B **16,** 994–7 (1999).

[26] R. S. Williamson III, P. A. Voytas, R. T. Newell, and T. Walker, “A magneto-optical trap loaded from a pyramidal funnel,” Opt. Express **3,** 111–117 (1998).

[27] K. I. Lee, J. A. Kim, H. R. Noh, and W. Jhe, "Single-beam atom trap in a pyramidal and conical hollow mirror," Opt. Lett. **21,** 1177–9 (1996).

[28] D. Müller, E. A. Cornell, D. Z. Anderson, and E. R. I. Abraham, "Guiding laser-cooled atoms in hollow core fibers," submitted .

[29] D. Müller, D. Z. Anderson, R. J. Grow, P. D. D. Schwindt, and E. A. Cornell, "Guiding atoms around curves with lithographically patterned current-carrying wires," Phys. Rev. A (accepted) (1999).

[30] M. Stephens and C. Wieman, "High collection efficiency in a laser trap," Phys. Rev. Lett. **72,** 3787 – 90 (1994).

[31] M. Stephens, R. Rhodes, and C. Wieman, "Study of wall coatings for vapor-cell laser traps," J. Appl. Phys. **76,** 3479 – 88 (1994).

[32] K. Lindquist, M. Stephens, and C. Wieman, "Experimental and theoretical study of the vapor-cell Zeeman optical trap," Phys. Rev. A **46,** 4082 – 90 (1992).

[33] T. Dinneen, A. Ghiorso, and H. Gould, "An orthotropic source of thermal atoms," Rev. Sci. Inst. **67,** 752 – 5 (1996).

[34] Z.-T. Lu, K. L. Corwin, K. R. Vogel, C. E. Wieman, T. P. Dinneen, J. Maddi, and H. Gould, "Efficient Collection of ^{221}Fr into a Vapor Cell Magneto-optical Trap," Phys. Rev. Lett. **79,** 994 – 997 (1997).

[35] J. S. Grossman, L. A. Orozco, M. R. Pearson, J. E. Simsarian, G. D. Sprouse, and W. Z. Zhao, "Hyperfine Anomaly Measurements in Francium Isotopes and the Radial Distribution of Neutrons," Phys. Rev. Lett. **83,** 935–8 (1999).

[36] M. A. Rowe, S. J. Freedman, B. K. Fujikawa, G. Gwinner, and S.-Q. Shang, "Ground-state hyperfine measurement in laser-trapped radioactive ^{21}Na," Phys. Rev. A **59,** 1869–73 (1999).

[37] J. E. Bjorkholm, R. R. Freeman, A. Ashkin, and D. B. Pearson, "Observation of Focusing of Neutral Atoms by the Dipole Forces of Resonance-Radiation Pressure," Phys. Rev. Lett. **41,** 1361–64 (1978).

[38] S. Chu, J. E. Bjorkholm, A. Ashkin, and A. Cable, "Experimental observation of optically trapped atoms," Phys. Rev. Lett. **57,** 314–7 (1986).

[39] J. D. Miller, R. A. Cline, and D. J. Heinzen, "Far-off-resonance optical trapping of atoms," Phys. Rev. A **47,** R4567–70 (1993).

[40] R. A. Cline, J. D. Miller, M. R. Matthews, and D. J. Heinzen, "Spin relaxation of optically trapped atoms by light scattering," Opt. Lett. **19,** 207–209 (1994).

[41] K. L. Corwin, S. J. M. Kuppens, D. Cho, and C. E. Wieman, "Spin-Polarized Atoms in a Circularly Polarized Optical Dipole Trap," Phys. Rev. Lett. **83,** 1311–14 (1999).

[42] C. Cohen-Tannoudji and J. Dupont-Roc, "Experimental study of Zeeman light shifts in weak magnetic fields," Phys. Rev. A **5,** 968–84 (1972).

[43] D. Cho, "Analogous Zeeman effect from the tensor polarizability in alkali atoms," J. of Korean Phys. Soc. **30,** 373–6 (1997).

[44] S. J. M. Kuppens, K. L. Corwin, K. Miller, T. Chupp, and C. E. Wieman, "The physics of loading an optical dipole trap," submitted (1999).

[45] N. R. Newbury, C. J. Myatt, E. A. Cornell, and C. E. Wieman, "Gravitational sisyphus cooling of ^{87}Rb in a magnetic trap," Phys. Rev. Lett. **74,** 2196–9 (1995).

[46] K. Gibble and S. Chu, "Laser-cooled Cs frequency standard and a new measurement of the frequency shift due to ultracold collisions," Phys. Rev. Lett. **70,** 1771–4 (1993).

[47] D. W. Keith, C. R. Ekstrom, Q. A. Turchette, and D. E. Pritchard, "An interferometer for atoms," Phys. Rev. Lett. **66,** 2693–6 (1991).

[48] M. J. Renn, E. A. Donley, E. A. Cornell, C. E. Wieman, and D. Z. Anderson, "Evanescent-wave guiding of atoms in hollow optical fibers," Phys. Rev. A **53,** R648–51 (1996).

[49] Z.-T. Lu, C. J. Bowers, S. J. Freedman, B. K. Fujikawa, J. L. Mortara, S.-Q. Shang, K. Coulter, and L. Young, "Laser trapping of short-lived radioactive isotopes," Phys. Rev. Lett. **72,** 3791–4 (1994).

[50] T. E. Barrett, S. W. Dapore-Schwartz, M. D. Ray, and G. P. Lafyatis, "Slowing atoms with sigma$^-$ polarized light," Phys. Rev. Lett. **67,** 3483–6 (1991).

[51] M. Zhu, C. W. Oates, and J. L. Hall, "Continuous high-flux monovelocity atomic beam based on a broadband laser-cooling technique," Phys. Rev. Lett. **67,** 46–9 (1991).

[52] W. Ketterle, A. Martin, M. A. Joffe, and D. E. Pritchard, "Slowing and cooling atoms in isotropic laser light," Phys. Rev. Lett. **69,** 2483–6 (1992).

[53] C. Monroe, Ph.D. thesis, Univ. of Colorado, Boulder, CO 80309, 1993.

[54] J. A. Behr *et al.*, "Magneto-optic trapping of beta-decaying ^{38}K and ^{37}K from an on-line isotope separator," Phys. Rev. Lett. **79,** 375–8 (1997).

[55] J. E. Simsarian, A. Ghosh, G. Gwinner, L. A. Orozco, G. D. Sprouse, and P. A. Voytas, "Magneto-optic trapping of ^{210}Fr," Phys. Rev. Lett. **76,** 3522–5 (1996), l. A. Orozco, SUNY Stony Brook, private communication.

[56] V. A. Dzuba, V. V. Flambaum, and O. P. Sushkov, "Calculation of energy levels, E1 transition amplitudes and parity violation in francium," Phys. Rev. A **51,** 3454–61 (1995).

[57] P. G. H. Sandars, "Enhancement Factor for the Electric Dipole Moment of the Valence Electron in an alkali atom," Phys. Lett. **22,** 290–1 (1966).

[58] R. Guckert, E. P. Chamberlin, D. W. Preston, V. D. Sandberg, D. Tupa, D. J. Vieira, H. Wollnik, and X. X. Zhao, "Coupling an optical trap to a mass separator," Nucl. Instrum. Methods Phys. Res. B **126,** 383 – 5 (1997).

[59] L. A. Bray, (Pacific Northwest National Labs, 1996), private communication.

[60] S. Gerstenkorn, J. Berges, and J. Chevillard, "Atlas Du Spectre D'Absorption de la Molecule d'Iode," Technical report, Laboratoire Aime Cotton (1982) .

[61] J. Hall and S. A. Lee, "Interferometric Real-time Display of CW Dye Laser Wavelength with Sub-Doppler Accuracy," Appl. Phys. Lett. **29,** 367 (1976).

[62] I. collaboration: A. Coc *et al.*, "Isotope shifts, spins and hyperfine structures of ^{118,146}Cs and of some francium isotopes," Nuc. Phys. A **468,** 1 – 10 (1987).

[63] S. V. Andreev, V. I. Mishin, and V. S. Letokhov, "Rydberg levels and ionization potential of francium measured by laser-resonance ionisation in a hot cavity," J. Opt. Soc. Am. B **5,** 2190 – 8 (1988).

[64] M. A. Kasevich, E. Riis, L. Chu, and R. G. DeVoe, "RF spectroscopy in an atomic fountain," Phys. Rev. Lett. **63,** 612 – 5 (1989).

[65] T. Walker, P. Feng, D. Hoffman, and R. S. Williamson III, "Spin-polarized spontaneous-force atom trap," Phys. Rev. Lett. **69,** 2168–71 (1992).

[66] J. R. Gardner, R. A. Cline, J. D. Miller, D. J. Heinzen, H. M. J. M. Boesten, and B. J. Verhaar, "Collisions of doubly spin-polarized, ultracold ^{85}Rb atoms," Phys. Rev. Lett. **74,** 3764–7 (1995).

[67] W. Ketterle and N. J. VanDruten, "Evaporative cooling of trapped atoms," Adv. At. Mol. Opt. Phys. **37,** 181–236 (1996).

[68] G. R. Harrison, Massachusetts Institute of Technology Wavelength Tables (MIT Press, Cambridge, Mass., 1939).

[69] D. Boiron, A. Michaud, J. M. Fournier, L. Simard, M. Sprenger, G. Grynberg, and C. Salomon, "Cold and dense cesium clouds in far-detuned dipole traps," Phys. Rev. A **57,** R4106–9 (1998).

[70] K. L. Corwin, Z.-T. Lu, C. F. Hand, R. J. Epstein, and C. E. Wieman, "Frequency-stabilized diode laser with the Zeeman shift in an atomic vapor," Appl. Opt. **37,** 3295–8 (1998).

[71] M. E. Gehm, K. M. O'Hara, T. A. Savard, and J. E. Thomas, "Dynamics of noise-induced heating in atom traps," Phys. Rev. A **58,** 3914–21 (1998).

[72] Siegman, Lasers (University Science Books, Mill Valley, CA, 1986).

[73] E. Hecht, Optics (Addison-Wesley Publishing Company, Reading, Massachusetts, 1990).

[74] C. G. Townsend, N. T. Edwards, C. J. Cooper, K. P. Zetie, C. J. Foot, A. M. Steane, P. Szriftgiser, H. Perrin, and J. Dalibard, "Phase-space density in the magneto-optical trap," Phys. Rev. A **52,** 1423–40 (1995).

[75] T. P. Dinneen, K. R. Vogel, E. Arimondo, J. L. Hall, and A. Gallagher, "Cold collisions of Sr^*-Sr in a magneto-optical trap," Phys. Rev. A **59,** 1216–22 (1998).

[76] C. S. Adams, H. J. Lee, N. Davidson, M. Kasevich, and S. Chu, "Evaporative cooling in a crossed dipole trap," Phys. Rev. Lett. **74,** 3577–80 (1995).

[77] T. Takekoshi and R. J. Knize, "CO_2 laser trap for cesium atoms," Opt. Lett. **21,** 77–9 (1996).

[78] T. Walker and P. Feng, "Measurements of Collisions Between Laser-cooled Atoms," Advances in Atomic Molecular and Optical Physics **34,** 125–70 (1994).

[79] K. M. O'Hara, S. R. Granade, M. E. Gehm, T. A. Savard, S. Bali, C. Freed, and J. E. Thomas, "Ultrastable CO_2 Laser Trapping of Lithium Fermions," Phys. Rev. Lett. **82,** 4204–7 (1999).

[80] J. D. Miller, Ph.D. thesis, University of Texas, 1994.

[81] A. Gallagher and D. E. Pritchard, "Exoergic Collisions of Cold Na^*–Na," Phys. Rev. Lett. **63,** 957–60 (1989).

[82] P. D. Lett, K. Mølmer, S. D. Gensemer, K. Y. N. Tan, A. Kumarakrishnan, C. D. Wallace, and P. L. Gould, "Hyperfine structure modifications of collisional losses from light-force atom traps," J Phys. B **28,** 65 – 81 (1995).

[83] P. S. Julienne and J. Vigue, "Cold collisions of ground- and excited-state alkali-metal atoms," Phys. Rev. A **44,** 4464–85 (1991).

[84] S. D. Gensemer, V. Sanchez-Villicana, K. Y. N. Tan, T. T. Grove, and P. L. Gould, "Trap-loss collisions of ^{85}Rb and ^{87}Rb: Dependence on trap parameters," Phys. Rev. A **56,** 4055–63 (1997).

[85] D. Sesko, T. Walker, C. Monroe, A. Gallagher, and C. Wieman, "Collisional Losses from a Light-Force Atom Trap," Phys. Rev. Lett. **63,** 961–4 (1989).

[86] C. D. Wallace, T. P. Dinneen, K.-Y. N. Tan, T. T. Grove, and P. L. Gould, "Isotopic difference in trap loss collisions of laser cooled rubidium atoms," Phys. Rev. Lett. **69,** 897 – 900 (1992).

[87] L. Marcassa, V. Bagnato, Y. Wang, C. Tsao, J. Weiner, O. Dulieu, Y. B. Band, and P. S. Julienne, "Collisional loss rate in a magneto-optical trap for sodium atoms: Light-intensity dependence," Phys. Rev. A **47,** R4563–6 (1993).

[88] M. B. Peters, D. Hoffmann, J. D. Tobiason, and T. Walker, "Laser-induced ultracold Rb($5S_{1/2}$) + Rb($5P_{1/2}$) collisions," Phys. Rev. A **50,** R906–9 (1994).

[89] D. Hoffmann, P. Feng, and T. Walker, "Measurements of Rb trap-loss collision spectra," J. Opt. Soc. Am. B **11,** 712 – 20 (1994).

[90] M. Drewsen, P. Laurent, A. Nadir, G. Santarelli, A. Clairon, Y. Castin, D. Grison, and C. Salomon, "Investigation of sub-Doppler cooling effects in a cesium magneto-optical trap," App. Phys. B **59,** 283–98 (1994).

[91] A. Kuhn, H. Perrin, W. Hänsel, and C. Salomon, "Three Dimensional Raman Cooling using Velocity Selective Rapid Adiabatic Passage," In OSA Tops on Ultracold Atoms and BEC, K. Burnett, ed.,**7,** 58–65 (1996).

[92] H. Perrin, A. Kuhn, I. Bouchoule, and C. Salomon, "Sideband cooling of neutral atoms in a far-detuned optical lattice," Europhys. Lett. **42,** 395–400 (1998).

[93] V. Vuletić, C. Chin, A. J. Kerman, and S. Chu, "Degenerate Raman Sideband Cooling of Trapped Cesium Atoms at Very High Atomic Densities," Phys. Rev. Lett. **81,** 5768 – 71 (1998).

[94] Y. B. Ovchinnikov, D. V. Laryushin, V. I. Balykin, and V. S. Letokhov, "Cooling of atoms on reflection from a surface light wave," JETP Lett. **62,** 113 – 8 (1995).

[95] P. Desbiolles, M. Arndt, P. Szriftgiser, and J. Dalibard, "Elementary Sisyphus process close to a dielectric surface," Phys. Rev. A **54,** 4292 – 8 (1996).

[96] C. S. Wood, Ph.D. thesis, Univ. of Colorado, Boulder, CO 80309, 1996.

[97] J. C. Camparo and R. P. Frueholz, "Parameters of adiabatic rapid passage in the 0-0 hyperfine transition of ^{87}Rb," Phys. Rev. A **30,** 803–11 (1984).

[98] M.-O. Mewes, M. R. Andrews, D. M. Kurn, D. S. Durfee, C. G. Townsend, and W. Ketterle, "Output Coupler for Bose-Einstein Condensed Atoms," Phys. Rev. Lett. **78,** 582–5 (1997).

[99] L. D. Landau and E. M. Lifshitz, Mechanics (Pergamon Press, 1976).

[100] A. C. Wilson, J. C. Sharpe, C. R. McKenzie, P. J. Manson, and D. M. Warrington, "Narrow-linewidth master-oscillator power amplifier based on a semiconductor tapered amplifier," Applied Optics **37,** 4871–5 (19).

[101] G. Ferrari, M.-O. Mewes, F. Schreck, and C. Salomon, "High-power multiple-frequency narrow-linewidth laser source based on a semiconductor tapered amplifier," Optics Letters **24,** 151–3 (1999).

[102] L. S. Cutler, “Frequency stabilized laser system,” U.S. patent 3,534,292 (1970).

[103] C. E. Wieman and L. Hollberg, “Using diode lasers for atomic physics,” Rev. Sci. Instrum. **62,** 1 – 20 (1991).

[104] K. B. MacAdam, A. Steinbach, and C. Wieman, “A narrow-band uunable diode laser system with grating feedback and a saturated absorption spectrometer for Cs and Rb,” Am. J. Phys. **60,** 1098 – 111 (1992).

[105] B. Cheron, H. Gilles, J. Havel, O. Moreau, and H. Sorel, “Laser frequency stabilization using Zeeman effect,” J. Phys. III **4,** 401 – 6 (1994).

[106] W. Demtröder, Laser Spectroscopy (Springer-Verlag, New York, 1996).

Appendix A

Dichroic Atomic Vapor Laser Lock

A.1 Introduction

Lasers with stable frequencies are essential in many fields of research. In addition, they are used commercially in precision machining tools, gravimeters, and laser vibrometers. He-Ne lasers have been the industry standard for many years,[102] but they are bulky, energy inefficient, and have limited tube lifetime. Diode lasers offer an improvement in all these areas and moreover can be stabilized to atomic transitions. Typical methods of stabilization [103, 104] although practical in some laboratory settings, are not reliable enough for use in commercial equipment. Using a technique originally demonstrated with a LNA ($La_{(1-x)}Nd_xMgAl_{11}0_{19}$) laser in helium [105] we developed a robust diode laser stabilization scheme that will be useful in both commercial instruments and research laboratories.

A.2 Diode Laser Frequency Stabilization

The frequency of a diode laser with grating feedback depends on the current, temperature, and external diffraction grating position. With the laser cavity in a Littrow configuration (see Fig. A.1), the output beam reflects off the grating, while the first-order beam diffracts back into the laser diode. The optical feedback from the grating is spectrally narrowed and peaked at a frequency that can differ from the bare diode central frequency. Thus this feedback narrows the laser linewidth to <1 MHz and forces the central frequency to nearly that of the feedback signal. To tune the laser central frequency, the grating is tilted by applying a voltage to a piezoelectric transducer (PZT). Over time, the central frequency will drift because of temperature, current, and mechanical fluctuations. This drift can be reduced by stabilizing the laser to an external reference. In addition, small, rapid fluctuations in laser frequency, which contribute to the laser linewidth, can be reduced by rapidly controlling the diode laser current.

In one popular method of stabilizing the diode laser frequency, some of the output light is sent into a saturated absorption spectrometer. The diode laser frequency is then locked to either the side or the peak of the narrow saturated absorption features, [103, 104, 106] shown in Fig. A.2. These narrow lines offer the advantage of a steep slope, where the slope is the change in the fractional absorption signal with laser frequency. Side-locking to this slope is accomplished by electrically controlling the PZT

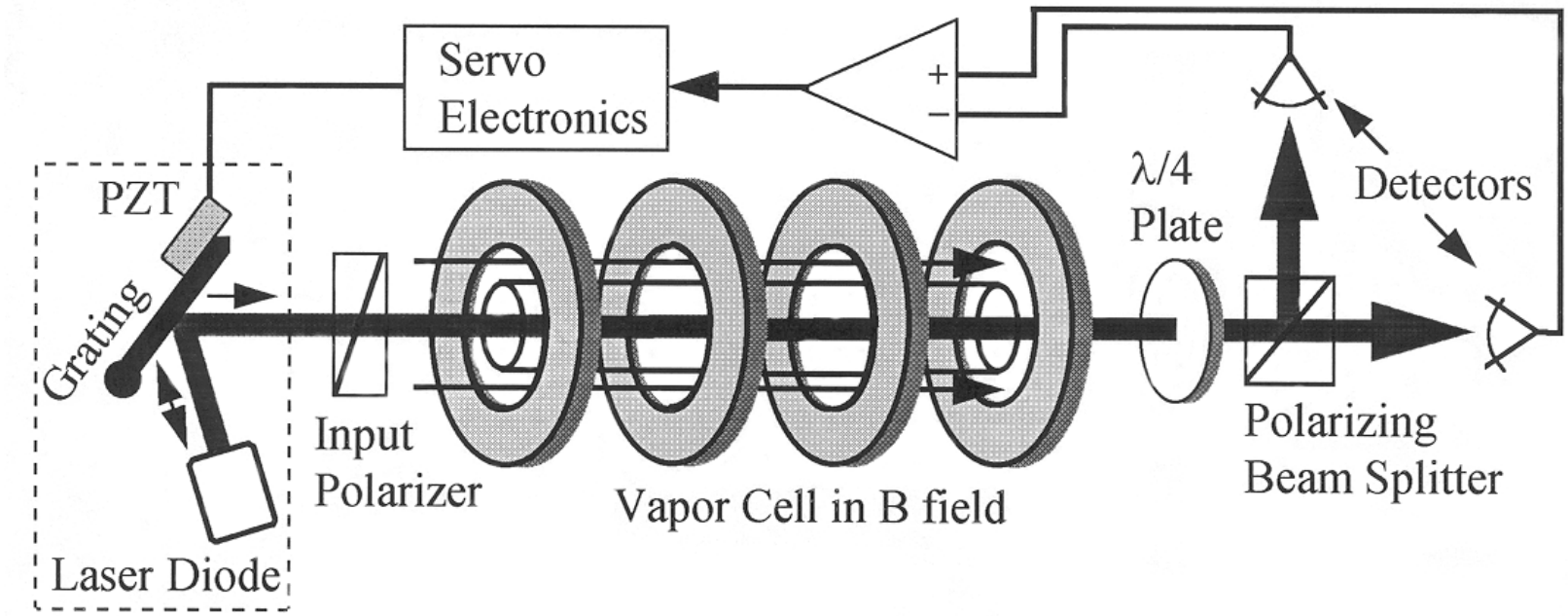

Figure A.1: Schematic of a DAVLL system. Here we show the entire beam passing through the lock, but in actuality, only a small amount of power is picked off from the main beam and enters the locking apparatus.

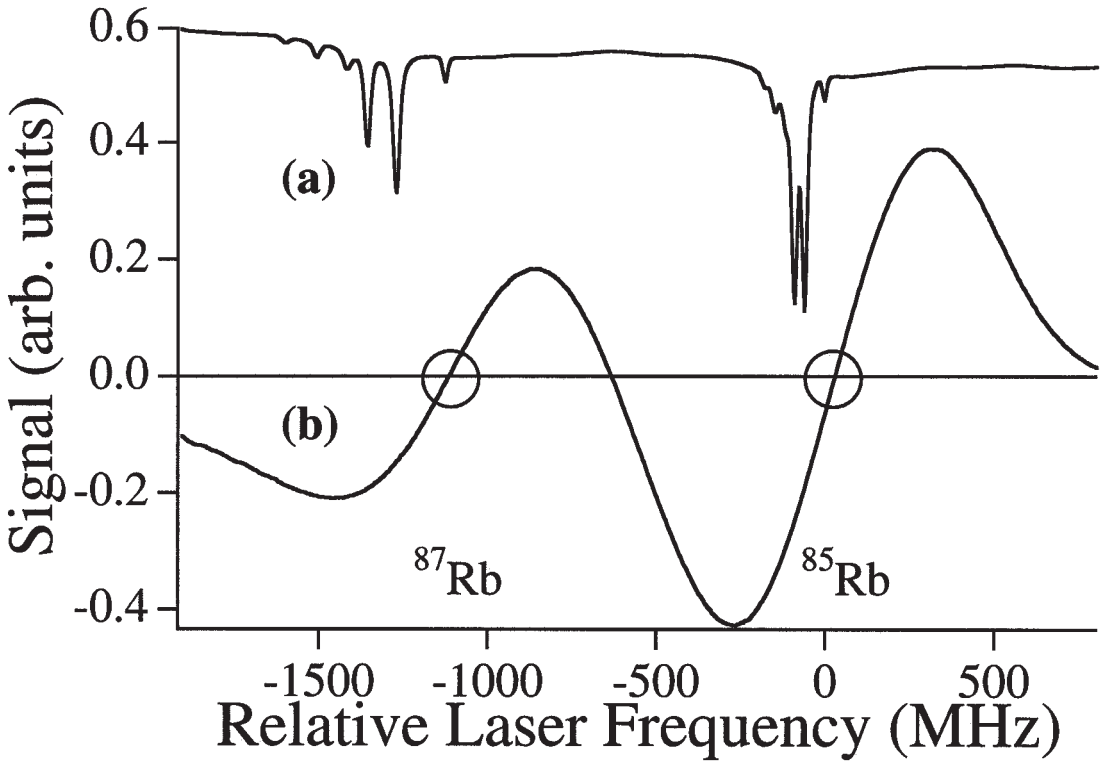

Figure A.2: Oscilloscope trace of (a) the signal from a saturated absorption spectrometer and (b) the DAVLL signal, as the diode laser is scanned across Rb resonances with the PZT. A laser can be locked to either of the two circled zero crossings of the DAVLL signal. These features are due to the ^{87}Rb $F = 2 \rightarrow F' = 1, 2, 3$ and the $^{8}5$Rb $F = 3 \rightarrow F' = 2, 3, 4$ transitions. The frequency of the lock point can be tuned optically by rotating the quarter-wave plate, or electronically by adding an offset voltage to the signal.

voltage so that the saturated absorption signal is maintained at a particular level. However, a disadvantage of side-locking is that fluctuations in beam alignment and intensity will alter the lock point and cause drift in the laser frequency. Peak-locking is less sensitive to these fluctuations, but has its own disadvantages related to phase-sensitive detection: Either the output of the laser is modulated directly or expensive electro-optic components are used to modulate only the light entering the spectrometer. A further disadvantage of both peak and side locks is their small capture range, which prevents them from recovering from perturbations that shift the laser frequency by more than -30 MHz.

A.3 The Dichroic-Atomic-Vapor Laser Lock Signal

To overcome the aforementioned disadvantages with the conventional locks, we developed a dichroic-atomic-vapor laser lock (DAVLL). This technique employs a weak

magnetic field to split the Zeeman components of an atomic Doppler-broadened absorption signal and then generates an error signal that depends on the difference in absorption rates of the two components. The subtraction technique minimizes the frequency drifts that are due to changes in line shape and absorption that typically limit the utility of Doppler-broadened absorption features for frequency stabilization. The DAVLL lock offers the advantages over saturated absorption: large recapture range, simplicity, low cost, and no need for frequency modulation.

As shown in Fig. A.3(a), a Doppler-broadened absorption feature is detected when a laser beam (with wave vector $\mathbf{k} = k\hat{z}$) passes through a Rb vapor and the laser's frequency is scanned across a transition. In the absence of a magnetic field, we obtain the same signal regardless of the laser polarization (c). However, if a uniform magnetic field ($\mathbf{B} = B\hat{z}$) is present and the laser is circularly polarized ($\epsilon = \hat{\sigma}_+$), the central frequency of the absorption feature increases [Fig. A.3(b)]. If the laser has the opposite polarization ($\epsilon = \hat{\sigma}_-$) [Fig. A.3(c)], the central frequency decreases. By subtracting the two absorption profiles [Fig. A.3(d)], we obtain an antisymmetric signal that passes through zero and is suitable for locking.

A DAVLL signal with a steep slope causes the lock to be less sensitive to noise sources that mimic laser frequency changes, such as laser intensity noise. A rough comparison with a typical saturated absorp- tion setup in our laboratory shows that the DAVLL slope is comparable with that of the saturated absorption lines. This may seem surprising at first, because the linewidths of the saturated absorption lines (FWHM -20 MHz) are much smaller than those of the DAVLL lines (-500 MHz peak-peak) [Fig. A.2(b)]. However, the heights of the saturated absorption features range from $\sim$1/3 to 1/30 of the on-resonant Doppler-broadened absorption fraction, whereas the DAVLL signal height is twice that absorption fraction. By approximating the slope as the linewidth divided by the signal height, we estimate that the slope of the largest saturated absorption peak is only four times bigger than the DAVLL slope.

The slope of the DAVLL signal is also affected by the magnetic field. The separation of the two Zeeman-shifted absorption peaks must be large enough to give a sizable capture range, but small enough to give a large slope through the unshifted resonance. In addition, the Zeeman-shifted absorp- tion peaks broaden with increasing field, because the various transitions contained within one Doppler- broadened feature shift different amounts. We found that 100 G maximizes the slope, and therefore represents the best compromise between increased separation and increased broadening. However, the dependence of slope on the magnetic field is not strong, so if B is varied by a factor of 2 it should not significantly alter the lock performance.

A.4 Apparatus

A schematic of the diode laser and optics used to generate the DAVLL signal is shown in Fig. A.1. The SDL 780 nm diode laser is tuned by use of a diffraction grating, as described above. The output beam from this laser passes through a beam splitter, and a small amount of power is split off to be used for locking. After passing through a small aperture, the resulting beam passes through a linear polarizer. Pure linear polarization

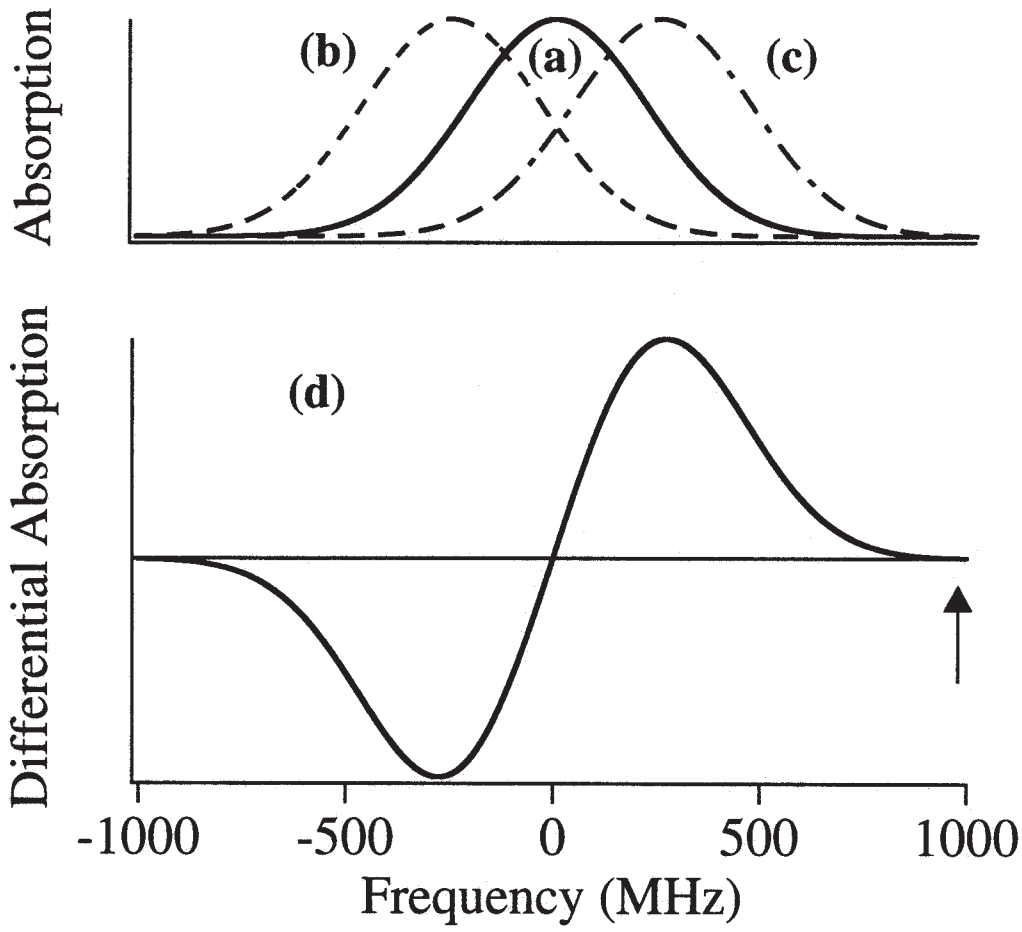

Figure A.3: Origin of the DAVLL signal shape. (a) A Doppler-broadened transition in Rb in the presence of no magnetic field. (b) The same transition, Zeeman shifted in a 100 G magnetic field, when circularly polarized light is incident on the vapor. (c) The same as (b), but with the opposite circular polarization. (d) The difference between (c) and (b) giving the DAVLL signal. In this idealized case, the arrow indicates that the off-resonant signal is zero.

is equivalent to a linear combination of equal amounts of two circular polarizations. This beam (2.5-mm diameter, 0.5 mW) next passes through a cell-magnet combination, consisting of a glass cell filled with Rb vapor and a 100 G magnetic field. The magnet is made of rings of rubber-embedded permanently magnetic material, spaced appropriately and glued together concentrically around the glass cell.[1] To generate the DAVLL signal, the absorption profiles of the $\hat{\sigma}_+$ light must be subtracted from that of the $\hat{\sigma}_-$. To accomplish this, after exiting the cell, the two circular polarizations are converted into two orthogonal linear polarizations by passing through a quarter-wave plate. Then the two linear polarizations are separated by a polarizing beam splitter, and the resulting two beams are incident on two photodetectors whose photocurrents are subtracted. As the frequency of the laser is scanned across an atomic transition, an antisymmetric curve is generated, as shown in Figs. A.2 and A.3. The diode laser is then locked by feeding back a voltage to the PZT so that the DAVLL signal is maintained at the central zero crossing.

We align the optics by orienting the fast axis of the quarter-wave plate at 45^o to the axis of the output polarizing beam splitter, so that equal intensities are incident on the two photodetectors when the laser is far detuned ($>$1 GHz) from the Rb resonances [see Fig. A.3(d)]. The DAVLL system is least susceptible to drifts when the off-resonant signal gives no net photocurrent, and the lock is therefore very near the center of the unshifted resonance, as shown in Figs. A.2 and A.3. We tuned the locked laser frequency either by adding an electronic offset or by rotating the quarter-wave plate. The latter optical method changes the frequency by weighting one circular polarization more heavily than the other. This type of offset is more stable than the electronic offset because the lock point is always at a zero in net photocurrent, which occurs when the powers incident on the two photodetectors are equal. Thus with optical offsets, the lock point maintains its insensitivity to laser intensity fluctuations.

A.5 Characterization of Frequency Stability

To monitor the frequency stability of the laser lock, we stabilized two separate lasers each to their own DAVLL system. We locked them to the same Doppler-broadened feature (^{85}Rb $F = 3 \rightarrow F'$) with different optical offsets, typically approximately 25 MHz apart. A portion of the light from each laser was combined at a beam splitter and copropagated onto a fast photodetector (125 MHz). The resulting beat note, corresponding to the difference between the two laser frequencies, was fed into a high-speed counter. By reading the counter every 5 s, a computer monitored the laser stability over periods ranging from 12 to 38 h.

In this way, the difference between the two laser frequencies was monitored over many days, under different conditions. The beat frequency was stable to 2.0 MHz peak-peak while the temperature of the laboratory, and therefore of the optical components,

[1] We used the material with part number PSM1-250-3X36C from the Magnet Source, 607-T S. Gilbert St., Castle Rock, Colo. 80104, 1-800-525-3536. Although uniformity is not critical to stability, we minimized variations to 5% along the field axis of symmetry by spacing the inside rings closer together than the outer ones.

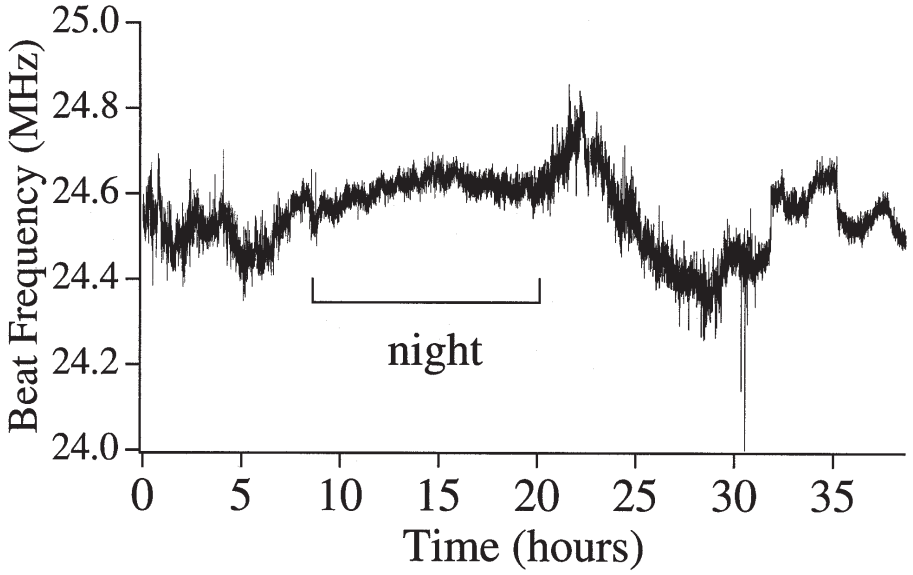

Figure A.4: Measured beat frequency between two DAVLL systems over a 38 h period. Variations in the beat frequency indicate the limits of the laser stability to be approximately 500 kHz peak-peak. These data show a stability of 27 kHz rms during an 11 h period at night when environmental factors such as room temperature and air currents are more stable. The discontinuities at the end of the run are due to incomplete shielding of the detection photodiodes from room lights. The run was stopped when a laser mode hopped, but after we adjusted the current to return the laser to the proper mode, it returned to the same frequency.

varied a couple of degrees throughout the day. When the cells (with attached magnets) were enclosed in a copper pipe and crudely temperature stabilized, the stability improved to 500 kHz peak-peak over 38 h, as shown in Fig. A.4. The cell-magnet combinations have measured dependences of 1.0 MHz/^{o}C and 1.7 MHz/^{o}C. We attribute this drift to a temperature-dependent birefringence of the cell windows, because the lock point is more sensitive to birefringence than to any other parameters. This is expected and observed, as discussed below. To confirm that optical offsets are more stable than electronic, we used an optical offset to tune one laser 120 MHz away and found that the drift rate was still comparable. When similar frequency offsets were applied electronically, the drift increased to 3 MHz peak-peak.

If the two lasers drift in a correlated manner, then the difference frequency remains constant so the above measurement is insensitive to it. To confirm that this was not occurring, we measured the stability of one DAVLL system by beating it against a second diode laser that was locked to a peak of a saturated absorption feature. Because the physics of the two locks is quite different, we expect drifts in the two systems to have different dependencies. In this case, we observe a stability of 200 kHz peak-peak over 12 h, which is consistent with the result previously described. From this we conclude that the two DAVLL systems were not drifting in a correlated manner, and

the stability of the beat frequency can be interpreted as the stability of the absolute frequency.

The frequency stability of the lock can also be predicted without comparing two separate systems. We can convert the stability of the off-resonant signal level (Fig. A.3) to an equivalent frequency stability by multiplying the fluctuations in photocurrent by the slope of the central resonant DAVLL signal. This calculation reliably predicts the frequency stability of the locked system and is therefore a simple, useful diagnostic. The agreement between the predicted and measured stability also indicates that the primary source of drift is changing birefringence of the optical components, because birefringence equally affects the signal levels both on and off resonance. As a final testament to the lock's stability, we used these lasers to maintain a Rb magneto-optic trap for many days without adjusting the lasers that were locked to DAVLL systems.

The above results were obtained by use of zero-order glass/polymer retarders, calcite Glan-Thompson input polarizers, and calcite Wollaston prism beam splitters. Comparable stability was also found when we used less expensive optics, including a plastic film polarizer, a plastic film retarder ($\lambda/4$ at 540 nm), and a single calcite crystal (used as a polarizing beam splitter). In contrast, we found that some dielectric polarizing beam-splitting cubes give a large temperature dependence.

The DAVLL lock was found to be robust because of the very broad locking signal. In fact, we applied mechanical perturbations to the optical table as high as the table's damage threshold (including banging on the table with a hammer) and were unable to knock the lasers out of lock. The lasers jumped once every couple days, apparently because one of the lasers jumped to a different mode of the laser chip. These jumps were usually attributable to temperature drifts in the laser chip, but could occasionally be caused by a fast electromagnetic pulse such as that produced by our turning on a large nearby argon-ion laser. These types of mode hops are not observed in diodes with good antireflection coatings because the chip resonances are greatly suppressed. Therefore a DAVLL system constructed with such diodes would likely never lose lock.

A.6 Conclusion

We have shown that the DAVLL lock provides an effective method for stabilizing a diode laser to a very broad, stable atomic reference. In comparison with saturated absorption locks, this system stays locked for much longer periods of time and requires fewer optics, less electronics, and less laser power. It can also be quite compact and inexpensive. This simple, robust stabilization scheme should work for a number of atomic and molecular species at a variety of wavelengths and is an appealing option whenever a continuous stable laser frequency is desired.

Appendix B

Stabilization of a Diode Laser at an Arbitrary Frequency

B.1 Introduction

We describe a general technique for stabilizing a diode laser to an arbitrary wavelength. This involves the use of a stable diode laser locked to an atomic transition at a different wavelength, and a low-finesse scanning Fabry-Perot cavity. The resulting lock is very robust and tunable. Therefore this lock can be employed in situations where no atomic or molecular absorption lines exist.

This development was motivated by the Fr MOT described in Chapt.3. For that trap, two lasers needed to be stabilized to two different transitions, one at the D_2 transition and the other at the D_1. This is more challenging than locking to the corresponding lines in Rb because no stable isotopes of Fr exist, and therefore a Fr absorption cell is not an option. While molecular iodine lines exist near the ^{221}Fr D_2 line, none are available near the D_1.

The cavity lock was therefore developed to meet some unusual demands. We knew the frequency of the ^{221}Fr D_1 line only to within about 100 MHz, so our lock reference had to allow for a large scanning range. Because we had access to a λ-meter with precision of a few MHz, long-term (day-to-day) stability was not particularly necessary. However, a robust lock was essential, because we needed to find both laser frequencies simultaneously by fixing the D_1 diode laser and scanning and the D_2 laser. If the laser frequently lost lock, we would never find the Fr laser frequencies.

Thus we devised a scheme that offered all of the above benefits with relatively simple components. In short, a commercial scanning Fabry-Perot cavity was used to transfer the stability of a diode laser locked to a Rb line (at 780 nm) to a diode laser near the Fr D_2 line at 817 nm.

B.2 Description

A schematic of the lock is shown in Fig. B.1. The idea is relatively straightforward. First a diode laser at wavelength λ_1 is stabilized to a readily accessible atomic transition. A beam from this laser is combined at a beam splitter (B.S.) with a beam from another laser at λ_2, the wavelength of interest. Following the beam splitter, a polarizer (Pol.) and quarter-wave retarder (λ/4) provide some optical isolation from the light that reflects off the cavity. The combined beam is then focused into a Fabry-Perot

cavity with mirrors that reflect at both wavelengths. The power transmitted through the cavity is partially collimated with another lens before it strikes a diffraction grating (D. G.) and diffracts into two separate beams, each of which is collected with a lens and focused onto a separate photodetector. This allows the transmitted power at each wavelength to be monitored separately. To lock the length of the cavity to λ_1, the power transmitted through the cavity at λ_1 is monitored, and this signal is fed back to the cavity PZT to control the length. This effectively makes the cavity a length standard, equal in length to a half-integral number of wavelengths (λ_1).

The frequency of the second diode laser is in turn locked to the cavity at λ_2. To do this, the transmitted power at λ_2 is monitored by an additional photodetector. Then the signal is fed back to the second diode laser to stabilize its frequency to the side of the transmission peak of λ_2s. In this way the stability of the first laser can be transferred to the second laser via the cavity. In addition, λ_2 can be tuned in a controllable way by making small changes to the frequency of the first laser. The cavity length will change, and therefore λ_2 will change by nearly the same amount as λ_1 of the second laser's lock point will also change by nearly the amount that the first laser was adjusted.

This scheme will only work, however, when the cavity transmits both wavelengths. This condition is of course not met at every cavity length, and in fact becomes less likely as the cavity finesse increases. As an example, consider the case for λ_1 = 780 nm and λ_2 = 817 nm. The transmitted power as monitored by the two photodetectors is shown in Fig. B.2 for these wavelengths. One can see in Fig. B.2 (a) that there are only a limited set of cavity mirror spacings for which power at both wavelengths will be transmitted. Fig. B.2 (b) and (c) show enlarged portions of (a). The distance one must translate the rear cavity mirror in order to observe coincident fringes depends on the two wavelengths and the finesse of the cavity. If the two wavelengths share a large least common denominator, then only a few fringes separate coincident fringes. For example, when λ_1 = 500 nm and λ_2 = 600 nm, then one must only scan 6 fringes at λ_1 or 5 at λ_2 in order to observe exact coincidence. In general, however, coincidence is only approximate, and depends on the width of the cavity resonance, or fringe. This fringe width is given by the cavity free spectral range (FSR) divided by the finesse F.

The number of fringes that separate coincident fringes can be easily calculated using a simple computer program, as shown in Fig. B.3. This simple algorithm, written in IDL,[1] will calculate the number of fringes that separate coincident fringes. The only input parameters consist of the two wavelengths and the finesse of the cavity. We have not been able to write down a simple analytical expression for the results of this routine, but one may certainly exist. For λ_1 = 780 nm and λ_2 = 817 nm, n_1 = 22 ($22 < F < 260$), n_1 = 265 ($260 < F < 850$) and n_1 = 780 for larger F.

[1] written by Kurt Miller

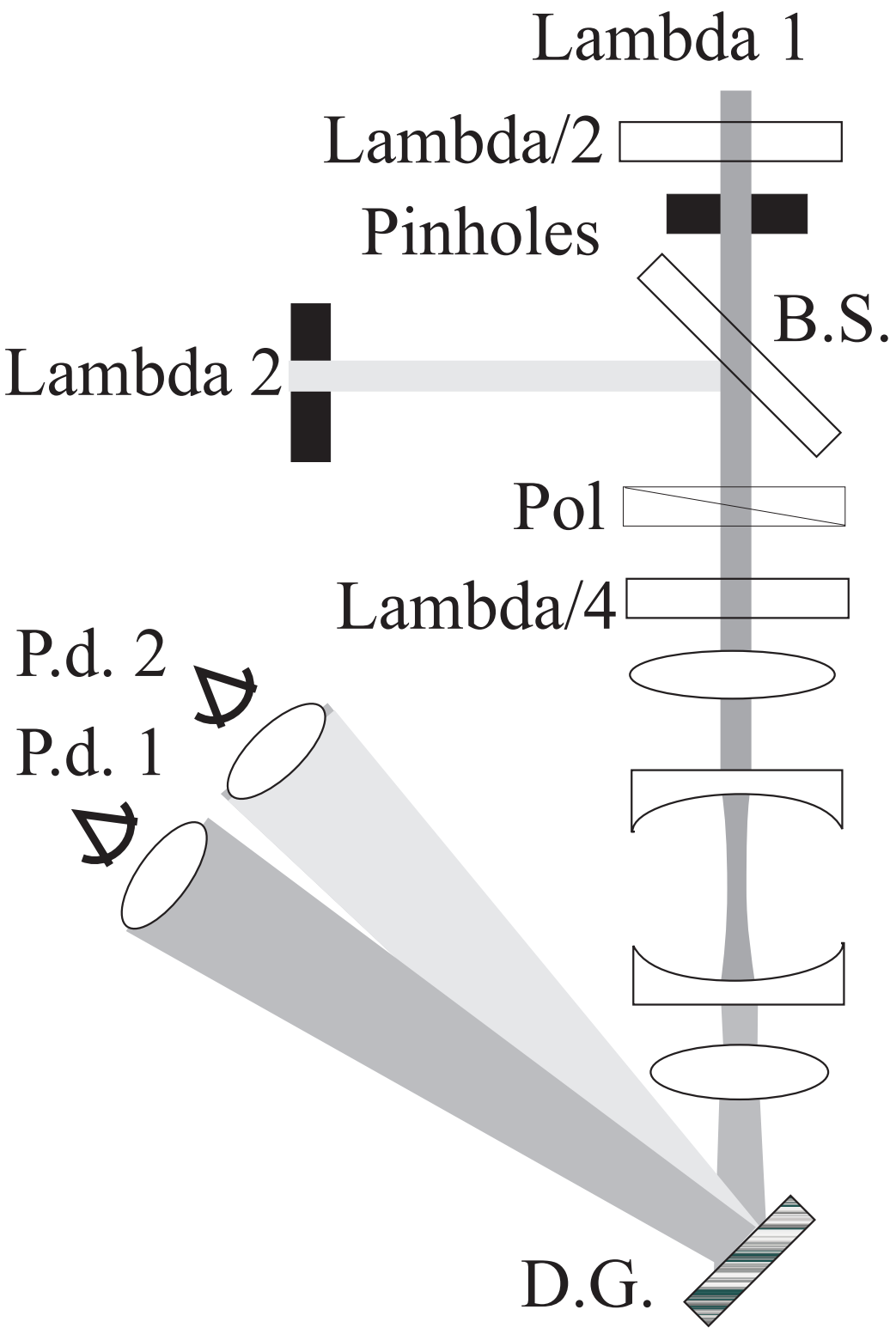

Figure B.1: Schematic of the cavity locking system used for transferring the stability of one laser to another.

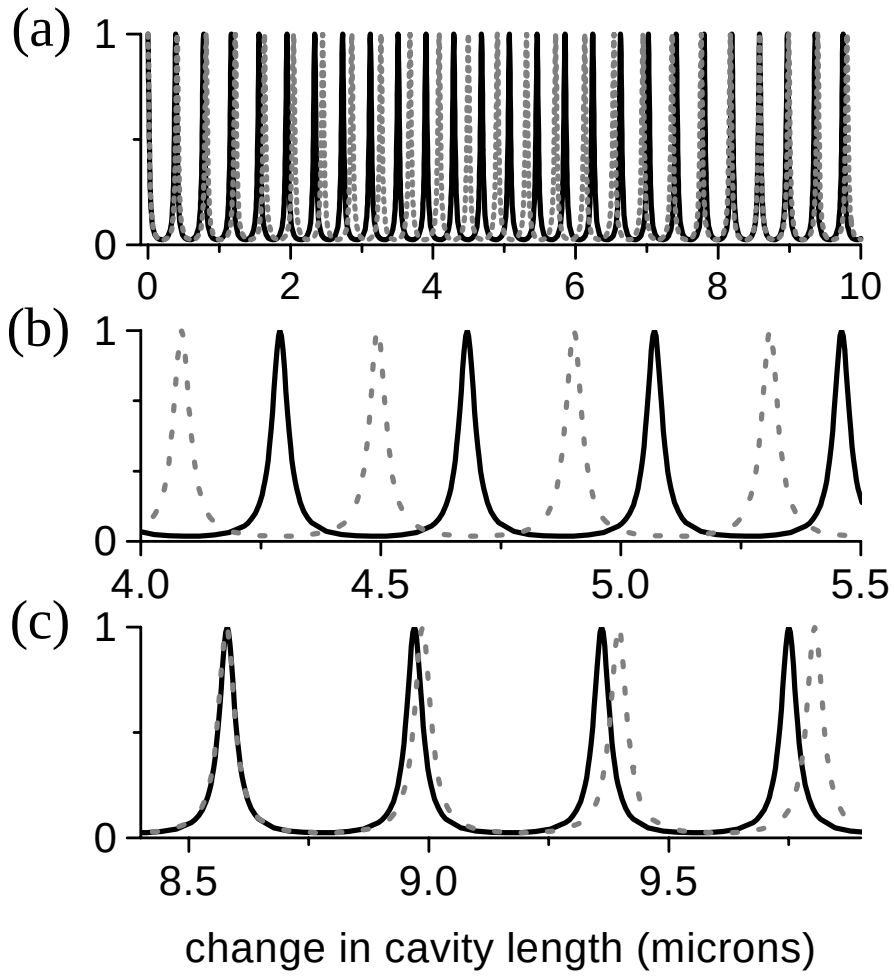

Figure B.2: Fractional transmission (calculated) of a cavity with a finesse of 40 for two different wavelengths. The dotted line represents the transmission of 780 nm, while the solid line represents 817 nm. Sections of plot (a) are enlarged below to show regions in which fringes are not coincident (b) and where fringes are coincident (c).

```
PRO cavity
;initialize
    n1          = 0L
    lambda1     = 780D
    lambda2     = 817 D
    F           = 130D
    flag        = 0

while (flag eq 0) do begin
                n1 = n1 + 1
                n2 = n1 * (lambda1/lambda2)
                if ( abs(n2-round(n2)) lt (1/F) ) then flag = 1
endwhile

print, 'n1=',n1, ' n2=',n2

END
```

Figure B.3: A simple computer algorithm (written in IDL) to calculate the distance one must change the length of the cavity (in units of cavity fringes) between coincident maxima in cavity transmission. Input parameters include the 2 wavelengths (lambda1 and lambda2) and the finesse of the cavity (F). The output parameters, n1 and n2, represent the number of fringes (for each wavelength) through which the cavity must scan before two fringes coincide at the same length, to within the width of the fringe.

B.3 Implementation

B.3.1 Components

The diode laser at 780 nm was stabilized to the Rb D_2 transition using the DAVLL scheme described in Appendix A and Ref. [70]. In fact, the requirements of insensitivity to disturbances motivated the development of the DAVLL lock. The output of this stabilized laser then entered the scanning Fabry-Perot cavity. The voltage applied to the PZT of the cavity was electronically controlled by monitoring the transmission of the 780 nm light through the cavity, and side-locking to one of the cavity fringes.

The SDL laser at 817 nm was employed without an external cavity, in order to extract the most power possible for the Fr MOT. As a result, up to 80 mW were sent to the trap from the 100 mW nominal output diode. The frequency of the diode was controlled by applying a DC voltage to the servo input of the current supply. Thus the voltage was used to tune the current of the diode laser. A small amount of power from this laser was sent into a λ-meter, as described in Chapt. 3. It had a precision of a few MHz, and therefore allowed the frequency of the 817 nm diode to be precisely determined. Without active frequency stabilization, the frequency drifted at 32 MHz/hr

or more.

The cavity we used was a commercially available Tropel scanning Fabry-Perot cavity. The mirror set we used was not particularly good at 817 or 780 nm, and as a result, the cavity finesse was small, typically about 60. We used a high frequency, high voltage amplifier built in the JILA electronics shop to drive the PZT of the cavity. The amplifier's high frequency response allowed us to use it in a servo loop to control the cavity length without inducing more phase shift than that inherent in the PZT-mirror spring-mass system alone. The position of the rear mirror could also be coarsely controlled by rotating the mirror mount so as to screw the mirror in and out.

B.3.2 Procedure

Once both lasers are optimally aligned into the cavity, the following procedure is employed to stabilize the frequency of the 817 nm diode laser. First, the 780 nm diode laser is locked to the zero-crossing of Fig. A.2, where it is least susceptible to drift. Then the 817 nm laser is tuned to the desired frequency by adjusting both its temperature and current while monitoring the λ-meter. A saw-tooth ramp applied to the high-voltage amplifier sweeps the cavity across several fringes, while the output of each photodetector is monitored on an oscilloscope as simulated in Fig. B.2. By simultaneously monitoring the fringes, the cavity can be adjusted such that the cavity is nearly confocal and the fringes are therefore as symmetric as possible. Even so, the fringes are often not completely symmetric. Then small turns of the screw are applied to find a pattern of coincident and nearly coincident fringes, as shown in Fig. B.2 (c).

Once the correct coincident fringes are found, the cavity is locked to the side of the transmission fringe observed by photodetector 1. At this point, one must recheck the frequency of the 817 nm laser, to ensure that it has not drifted too far, and if necessary, relock the cavity to a different fringe of the 780 nm diode. One must also keep in mind the desired tuning range of the 817 nm laser when selecting the cavity fringe. At last, the 817 nm diode frequency is side-locked to the transmitted power detected by photodetector 2. This frequency can then be scanned by changing the set point voltage of the DAVLL-locked diode laser.

B.3.3 Polarization

As a note, we also attempted to separate the two wavelengths using polarization instead of wavelength. In this scheme, the two wavelengths enter the cavity with opposite polarization, and are then separated at the output with a polarizing beam splitter. This method might prove useful in cases where λ_1 and λ_2 are too close together to make the diffraction grating useful. Unfortunately, this technique is very sensitive to slight mirror birefringence, especially for high finesse. This made it more difficult to eliminate cross-talk between the two polarizations, as discussed below. Therefore, the remainder of this Appendix will deal with the wavelength separation.

B.4 Results

The cavity lock performed very well throughout the Fr experiment. The robust behavior of the DAVLL lock has already been discussed. During the experiment, it essentially never lost lock. The 817 nm diode laser lost lock when it mode hopped, and this occurred every couple days, due to the unfortunate relative inaccessibility of our transition to our diode. The lock would also jump when the table was bumped too hard, because the cavity was sensitive to mechanical perturbations. Day-to-day, however, the cavity was also quite stable. Once the length was set, the coincident fringe would consistently be found at the same voltage, $\sim$200 V.

One possible limitation to the stability of the lock would be cross-talk between the two lasers. This would occur if some light detected by photodetector 2 was at λ_1 and vice versa. This leakage was less than 0.3%, implying that at least 99.7% of the light striking photodetector 2 was at λ_2.

Finally, all evidence indicates that the laser was stable to within a few MHz for hours. We were able to maintain a Fr MOT for hours at a time, and the MOT should be sensitive to changes of 3 MHz or less, especially operating with limited repump power as we were. The λ-meter readings were also stable to within its resolution.

B.5 Conclusion

In conclusion, we successfully transferred the stability of the DAVLL lock to an additional diode laser via a cavity. This technique has minimal technological requirements, including a low-quality diffraction grating and a low-finesse cavity. It allows for controlled tuning over a wide range of laser frequencies, up to several hundred MHz. Therefore this locking scheme is generally applicable to a large number of wavelengths for a variety of applications.